Olfactory pollution in the anthropocene: The impact of atmospheric NO_x and ozone pollution on plant-pollinator interactions

Ka Lok Jeremy Chan

A dissertation

submitted in partial fulfillment of the

requirements for the degree of

Doctor of Philosophy

University of Washington

2022

Reading Committee:

Jeffrey Riffell, Co-Chair

Joel Thornton, Co-Chair

Thomas Daniel

Program Authorized to Offer Degree:

Biology

University of Washington

Abstract

Olfactory pollution in the anthropocene: The impact of atmospheric NO_x and ozone pollution on plant-pollinator interactions

Ka Lok Jeremy Chan

Co-Chairs of the Supervisory Committee:
Jeffrey Riffell
Biology
Joel Thornton
Atmospheric Sciences

Olfaction is the oldest sense, and olfactory navigation is important for many animals. Air pollution from human activity has been shown to disrupt olfactory navigation, though we have only recently started investigating these impacts, and the mechanisms and scope of these disruptions remain largely unknown. We focused on the impacts of atmospheric ozone and nitrate radicals (hereafter 'oxidants') from air pollution on floral scent transmission, and how it affects pollinator behavior in the field. To study the impact of the oxidants on floral scent signals, we first developed an electrospray ionization source for a high-resolution time-of-flight mass spectrometer (HR-TOFMS). This ionization source is able to measure chemicals in the atmosphere with high sensitivity and time resolution by generating a variety of reagent ion species. We used the *Oenothera pallida – Hyles lineata / Manduca sexta* plant-pollinator system to study how oxidants affect *O. pallida* hawkmoth visitation by impacting floral scent

transmission. We performed pollinator observations and pollinator exclusion treatments to determine that hawkmoths are important pollinators of *O. pallida*. Then we collected and analyzed floral scent samples from *O. pallida* flowers and measured the antennographic responses of the hawkmoths *Hyles lineata* and *Manduca sexta* to the floral scent. We then produced an odor blend of antennographically active chemicals representing the most salient scent signals from the flowers to the hawkmoths. Then, we determined how oxidants from nocturnal air pollution degrade these floral scent signals, and what the behavioral impacts of this scent degradation on hawkmoth pollinator visitation behavior was in the field. Finally, we modeled the global impacts of such scent degradation on pollinator scent navigation using the reaction rates and global oxidant distributions from the GEOS-Chem global chemical model under simulated present day and pre-industrial conditions. We found that atmospheric oxidants impact hawkmoth visitation rates to floral odor sources by degrading the monoterpene component of the odor. The model results show that under current global concentrations of oxidants, nitrate radicals degrade most floral volatiles significantly more than ozone does, and that many major cities have had scent recognition distances reduced by more than 70% compared to pre-industrial times.

TABLE OF CONTENTS

ACKNOWLEDGEMENTS

Many people have helped me along the way and made this endeavor possible. Some helped with the research or logistics, but everyone made the journey meaningful and enjoyable.

I am grateful to Jeff Riffell for being a great scientific and personal mentor to me, offering amazing support and patience through the past seven years, and believing in me. I thank Joel Thornton for his guidance and sagely scientific advice. I would also like to thank my committee members Tom Daniel, Janneke Hille-Ris-Lambers and David Gire for their guidance and advice.

I am thankful to Sriram Parasurama for his help with countless experiments and analyses, and Eleanore Sammeth and Regina Mettey for their help with my project. I thank Binh Nguyen for his incredible dedication of time to keeping all the insect colonies alive so that the research could happen, and Jeanette Milne for keeping my study plants alive. Claire Rusch and Diego Alonso for their help with data analysis and programming. Yue Zhao for working with me on the electrospray ionization project. Members of the Riffell group and Thornton group for helping me out in the lab, and in creating a fun and supportive environment to work in. Members of the biology and atmospheric sciences departments for creating a stimulating and welcoming environment.

I would like to thank my undergraduate mentors Natia Frank, Tom Reimchen, Patrick von Aderkas, Barbara Hawkins and Paul Bentley for nurturing my interest and motivation in science.

I am grateful to Eric Grace for being a personal and scientific mentor who rekindled my passion in science and taught me to enjoy life along the way.

I am grateful to my family, especially my parents for supporting me through life and my academic journey. I wish that my dad could be here to share in this achievement.

I am deeply grateful to my partner Rachel Atlas for being my sunshine and my muse, for helping me through many difficult times, for stimulating discussions about everything, and for making everything awesome.

DEDICATION

To the wilderness

Introduction

Movement is important to animals for locating food, mates, shelter, and escaping from unfavorable situations. Key to movement is sensory navigation, which allows animals to make informed choices about their movements. Animals use multiple sensory modes to navigate. Examples include how humans simultaneously use visual, auditory, and olfactory reception to navigate through landscapes, how bats and cetaceans use echolocation via auditory reception to navigate, and how migrating birds use visual, olfactory, and magnetoreception to guide their migratory flights. Olfaction is the oldest sense. It is used by bacteria to locate food and escape threats in the absence of other senses, and we will examine olfactory navigation in greater detail in this dissertation.

Human activity has been known to impact several sensory modalities (Dominoni et al., 2020). For example, insects and migrating birds are drawn to light sources at night (Firebaugh and Haynes, 2016), and sonar has been implicated in strandings of cetaceans (Brownell Jr et al., 2009). Air pollution has been shown to interfere with olfactory navigation by affecting the emission of olfactory signals (Saunier and Blande, 2019), by masking olfactory signals (Riffell et al., 2014), by impacting the ability of animals to detect olfactory signals (Dotteryl et al., 2016; Vanderplanck et al., 2021; Demares et al., 2022), and by atmospheric degradation of the scent chemicals (Girling et al., 2013; Farre Armengol et al., 2015).

Few studies have examined the atmospheric processing of olfactory signals due to the difficulty of atmospheric chemical analysis. This is because the atmospheric concentrations are low, highly variable, and subject to surface effects which confound the analyses. Also, there have been few studies of the impacts of air pollution on olfactory navigation over larger spatial scales.

In this study we developed new tools for analyzing atmospheric chemistry to better understand the atmospheric degradation of scent signals used in olfactory navigation. Then we characterized the *Oenothera pallida* – hawkmoth plant-pollinator system as a model system for studying the impacts of air pollution on scent-mediated pollinator visitations. Next, we performed chemical analyses and electrophysiological measurements to determine *Oenothera pallida* floral scent composition, and which scent components were important for scent tracking in the hawkmoths *Hyles lineata* and *Manduca sexta* which were determined to be key pollinators of *Oenothera pallida*. We created an odor blend of the relevant scent components and analyzed the simulated atmospheric degradation of the odor components in atmospherically relevant concentrations of ozone and nitrate radicals. We studied nitrate radical chemistry since the hawkmoths are nocturnal, and nitrate radicals often dominate nighttime atmospheric degradation of volatile chemicals (Ng et al. 2017). We then determined what the impacts of this atmospheric degradation of *Oenothera pallida* floral odor blend was on hawkmoth visitations in a wind tunnel, and in the field. Finally, having analyzed the atmospheric degradation of *Oenothera pallida* scent, and the impact of that degradation on hawkmoth pollinator visitations, we used global atmospheric chemical modeling to model the potential impacts of global ozone and nitrate radical concentrations on pollinator scent tracking.

To study the impacts of air pollution on olfactory navigation, we first developed tools necessary for measuring chemicals in the atmosphere. There are many chemical methods available for analyzing chemicals in the atmosphere. Examples include photoionization detectors, mass spectrometry, fluorescence, and laser absorption. Each analytical method has its trade-offs in response time, sensitivity, and specificity, but high-resolution time-of-flight mass spectrometers (HR-TOFMS) have a unique combination of high sensitivity and fast response,

while being able to simultaneously record diverse chemical types and mass ranges (Riffell et al., 2008a). We developed a cross-flow electrospray chemical ionization source for a HR-TOFMS which was able to produce a variety reagent ions which had a range of sensitivities and specificities to different analytes, while having a high gas flow rate to enable the detection of analytes with low volatilities (Zhao et al., 2017).

Next, we determined the impacts of nocturnal air pollution on the ability of pollinators to locate floral scent sources using the *Oenothera pallida* – hawkmoth plant-pollinator system in Grant County, Washington. We characterized the *Oenothera pallida* – hawkmoth plant-pollinator system as an appropriate system for studying the impacts of air pollution on olfactory navigation. Hawkmoths in the North American Deserts ecoregions navigate over long distances to locate patches of flowers (Il, 1976; Raguso et al., 2003; Schiestl, 2015), and are particularly reliant on olfactory signals due to the lack of visual information at night. We performed pollinator observations and pollinator exclusion treatments to determine that hawkmoths are important pollinators of *O. pallida*.

Then we collected and analyzed floral scent samples from *O. pallida* flowers and measured the antennographic responses of the hawkmoths *Hyles lineata* and *Manduca sexta* to the floral scent. We then produced an odor blend of antennographically active chemicals representing the most salient scent signals from the flowers to the hawkmoths. Then, we determined how the reactive components of nocturnal air pollution including ozone (O_3) and nitrate radicals (NO_3) (hereafter 'oxidants') degrade these floral scent signals, and what the behavioral impacts of this scent degradation on hawkmoth pollinator visitation behavior was in a wind tunnel.

We also performed field experiments in Grant County, WA to determine the impact of atmospheric scent degradation on hawkmoth pollinator visitations. This work is important as the behavior of lab-reared hawkmoths might not reflect that of wild specimens due to differences in nutrition, development conditions, and life history, as well as the dynamic atmospheric conditions at the field site, the effects of background odors due to local vegetation, and the long-distance scent dispersal and pollinator attraction in the field. This work is one of the few studies that determine the impact of air pollution on pollinator visitations in the field, and the only one that specifically determines the impact of atmospheric ozone and nitrate radical oxidation.

Finally, we modeled the global impacts of such scent degradation on pollinator scent navigation using the reaction rates of floral volatiles with oxidants, and global oxidant distributions from the GEOS-Chem global chemical model under simulated present day and pre-industrial conditions. Our work is the first study that has determined the impacts of worldwide distributions of atmospheric oxidants on nocturnal scent recognition distances, and how these might have changed since pre-industrial times.

This work has limitations as only one plant-pollinator system was examined, though the findings of monoterpenes being the key scent chemicals responsible for failure of scent recognition in pollinators was consistent with two other studies on other systems in the literature (Girling et al., 2013; Farre Armengol et al., 2015). Other pollinator systems might rely on different chemical classes for scent recognition, which might change the way that those systems are impacted by atmospheric oxidants, but our analytical framework will be useful for determining the impacts in those systems if the relevant scent chemicals, and their degradation rates in the atmosphere can be determined. We failed to detect any oxidation products from the atmospheric oxidation of the odor blend with oxidants. These oxidation products can change the

odor background which might affect the perception of the odor by pollinators (Riffell et al., 2014). Lastly, our pre-industrial atmospheric simulation used present-day meteorology, and is unable to account for the effects of climate change on surface temperatures and winds which might change the way pollinator odor navigation is impacted by oxidants.

Other open questions include what effects the evolutionary pressure of odor signal degradation has had on olfactory communication and chemical ecology. Our data suggest that there was significant atmospheric scent degradation by oxidants in some regions of the world in pre-industrial times, meaning that these effects have been present over evolutionarily relevant timescales. It will also be valuable to investigate the effects of environmental degradation on olfactory communication in other systems, for example in systems which rely on other classes of volatiles for communication, or in aquatic systems.

Chapter 1

An electrospray chemical ionization source for real-time measurement of atmospheric organic and inorganic vapors

Zhao, Y., Chan, J. K., Lopez-Hilfiker, F. D., D'Ambro, E. L., Slowik, J. G., Riffell, J. A., and Thornton, J. A.

Atmospheric Measurement Techniques 2020

Abstract

We present an electrospray ion source coupled to an orthogonal continuous-flow atmospheric pressure chemical ionization region. The source can generate intense and stable currents of several specific reagent ions using a range of salt solutions prepared in methanol, thereby providing both an alternative to more common radioactive ion sources and allowing for the generation of reagent ions that are not available in current chemical ionization mass spectrometry (CIMS) techniques, such as alkali metal cations. We couple the orthogonal electrospray chemical ionization (ESCI) source to a high-resolution time-of-flight mass spectrometer (HRToF-MS), and assess instrument performance through calibrations using nitric acid (HNO_3), formic acid (HCOOH), and isoprene epoxydiol (*trans*-β-IEPOX) gas standards, and through measurements of oxidized organic compounds formed from ozonolysis of α-pinene in a continuous-flow reaction chamber. When using iodide as the reagent ion, the HRToF-ESCIMS prototype has a sensitivity of 11, 2.4, and 10 cps $pptv^{-1}$ per million cps of reagent ions and a detection limit (3σ, 5s averaging) of 4.9, 12.5, and 1.4 pptv to HNO_3, HCOOH, and

IEPOX, respectively. These values are comparable to those obtained using an Iodide-adduct HRToF-CIMS with a radioactive ion source and low pressure ion-molecule reaction region. Applications to the α-pinene ozonolysis system demonstrates that HRToF-ESCIMS can generate multiple reagent ions (e.g, I^-, NO_3^-, acetate, Li^+, Na^+, K^+, and NH_4^+) having different selectivity to provide a comprehensive molecular description of a complex organic system.

Introduction

The Earth's atmosphere contains thousands of inorganic and organic species that, through complex free radical and multiphase chemistry, play a vital role in air quality and climate change (Finlayson-Pitts and Pitts, 2000; Seinfeld and Pandis, 2006; Goldstein and Galbally, 2007). Characterizing the identity and abundance of many of these species in the atmosphere is essential for understanding their atmospheric processes and subsequent environmental and climate impacts. As a result, there is a critical interest in the development and application of the state-of-art analytical instruments for the analysis of atmospheric composition (Noziere et al., 2015). As a sensitive, selective, and soft-ionization measurement technique, chemical ionization mass spectrometry (CIMS) has received significant use in the real-time *in situ* measurement of atmospheric trace species (Huey et al., 1995; Fortner et al., 2004; Hearn and Smith, 2004; Smith et al., 2004; Crounse et al., 2006; Huey, 2007; Veres et al., 2008; Kercher et al., 2009; Zhao et al., 2010). The recent coupling of chemical ionization to high resolution time-of-flight mass spectrometers (HRToF-MS) enables the simultaneous determination of the abundance and molecular composition of a wide array of atmospheric inorganic and organic compounds with fast time response and high sensitivity (Junninen et al., 2010; Bertram et al., 2011; Yatavelli et al., 2012; Aljawhary et al., 2013; Lee et al., 2014; Lopez-Hilfiker et al., 2014; Brophy and

Farmer, 2015, 2016; Lopez-Hilfiker et al., 2016a; Yuan et al., 2016). The use of HRToF-CIMS has allowed groundbreaking progress in atmospheric organic chemistry, such as the observation of highly oxygenated molecules (HOMs) formed by monoterpene oxidation (Ehn et al., 2014; Jokinen et al., 2015; Berndt et al., 2016; Lee et al., 2016). Very recently, a newly developed proton-transfer reaction (PTR) time of flight instrument (PTR-3), has enabled sensitive detection of a wide range of organic compounds including HOMs (Breitenlechner et al., 2017).

In CIMS, the analyte molecule reacts with a specific reagent ion via one or more mechanisms, including ligand switching reaction forming an ion-molecule adduct (Huey et al., 1995; Kercher et al., 2009; Aljawhary et al., 2013; Lee et al., 2014; Brophy and Farmer, 2015, 2016), proton addition (abstraction) forming a protonated (deprotonated) ion (Nowak et al., 2002; Veres et al., 2008; Yatavelli et al., 2012; Aljawhary et al., 2013; Brophy and Farmer, 2015, 2016; Yuan et al., 2016), or by direct charge transfer forming a molecular ion (Huey et al., 1995; Kim et al., 2016). The reagent ions used mainly include I^-, NO_3^-, acetate, CF_3O^-, and SF_6^- for negative ion CIMS, and H_3O^+, NO^+, protonated ethanol, and benzene cation for positive ion CIMS. Choosing an appropriate reagent ion is essential for a comprehensive characterization of a specific class of molecules while having selectivity to avoid unnecessary congestion of the mass spectrum with unwanted components. For example, previous studies using NO_3^- CIMS have reported a very low yield of HOMs from OH oxidation of monoterpene (Jokinen et al., 2015). However, a recent study using acetate CIMS found a significantly higher HOMs yields from the same system (Berndt et al., 2016). The reason for this difference is presumably a lower sensitivity of NO_3^- to HOMs formed in OH oxidation of monoterpene than that of acetate (Berndt et al., 2016). On the other hand, many atmospheric organic systems consist of a wide range of organic compounds

with different functionality and polarity. Therefore, multiple complementary ionization schemes are needed to obtain a broad view of these systems (Aljawhary et al., 2013; Praplan et al., 2015). Some advantages of CIMS are that it is direct, online, reproducible and inherently quantitative in that the kinetic theory of gases allows a robust upper limit ionization efficiency, and thus instrument response, to be calculated knowing only the pressure and interaction time of reagent ions and analyte molecules. However, the need for gas-phase reagent ions limits the suite of usable reagent ions to those for which a safe and stable gas-phase precursor exists and which produce the desired reagent ion cleanly at a high yield when ionized. As such, certain reagent ions such as metal cations (e.g., Li^+, Na^+, and K^+) and NH_4^+, which are commonly used for detection of atmospheric organic compounds in off-line techniques like electrospray ionization (ESI)-MS (Nizkorodov et al., 2011; Laskin et al., 2012; Witkowski and Gierczak, 2013), have remained largely unavailable for CIMS (Fujii et al., 2001). Compared to I^-, NO_3^-, and acetate, which are generally more sensitive to more oxygenated organic compounds than to less oxygenated ones (Aljawhary et al., 2013; Lee et al., 2014, Hyttinen et al., 2015; Iyer et al., 2016, Berndt et al., 2016), these metal cations are expected to be able to to sensitively detect both less oxygenated (e.g, compounds containing only carbonyl groups) and highly oxygenated multi-functional organic species (Gao et al., 2010; Nguyen et al., 2010; Nizkorodov et al., 2011; Laskin et al., 2012; Witkowski and Gierczak, 2013; Zhao et al., 2015; Tu et al., 2016; Zhao et al., 2016; Zhang et al., 2017), and to form more strongly bound ion adducts. In addition, at present most CIMS techniques use a radioactive ion source such as Po-210 to produce the reagent ions, although more recently some utilize X-ray radiation, electrical discharge (Hirokawa et al., 2009; Yuan et al., 2016), or electron impact (Inomata and Hirokawa, 2017). Safety regulations for the transport and use of radioactive materials may limit the deployment of the

instrument with a radioactive ion source in the field, while other methods may be less intense or lead to higher backgrounds.

We have developed a non-radioactive reagent ion source that deploys a custom-built electrospray setup within an atmospheric pressure orthogonal ion-molecule reaction (IMR) chamber. The design of the IMR region is similar to that of the Cluster-CIMS developed by Eisele and coworkers (Zhao et al., 2010). The electrospray chemical ionization (ESCI) source is coupled to a HRToF-MS for characterization. We present the design and discuss the parameters most important for optimal performance of the ESCI source. Then, we assess its performance using the measurement of formic acid, IEPOX, nitric acid, and organic mixtures formed by ozonolysis of α-pinene in a continuous-flow reaction chamber. Our results demonstrate that the ESCI source provides a potential alternative to radioactive and X-ray ion source and opens a new avenue for the generation of reagent ions such as Li^+, Na^+, K^+, and so on, that were previously unavailable for CIMS.

Experimental

Instrument description

A schematic of the ESCI module is shown in Figure 1. The electrospray setup contains a 15 μm inner diameter (ID) fused silica spray needle (PicoTip™) mounted within a cylindrical evaporation chamber through which a flow of ultra-high purity (UHP) N_2 (referred to as the ion source flow) is passed to aid in the evaporation of the spray droplets and to transport ions into the IMR. Several spray needle diameters were tried (from 8 to 30 μm), with the 15 μm giving the best combination of longevity and ion intensity. The emitting end of the spray needle is located 4 mm from the distal wall of the evaporation chamber, which consists of a 13 mm ID stainless

steel (SS) tube centered on a circular SS aperture having a 4 mm diameter. The aperture forms the entrance to the IMR which is a portion of a 22 mm ID SS tube embedded in a Teflon block. The ion source flow enters the IMR through the aperture perpendicularly to the direction of a much larger sample flow, typically 10 to 20 standard liters per minute (slpm) drawn through the IMR by a dry scroll vacuum pump (IDP-3, Agilent Technologies). Preliminary fluid dynamic simulations suggest that the mixed sample and ion source flow in the IMR remains laminar when the ratio of the ion source flow to sample flow is ≤ 0.2 and the overall Reynolds number for the sample flow is low (sample flow < 20 slpm).

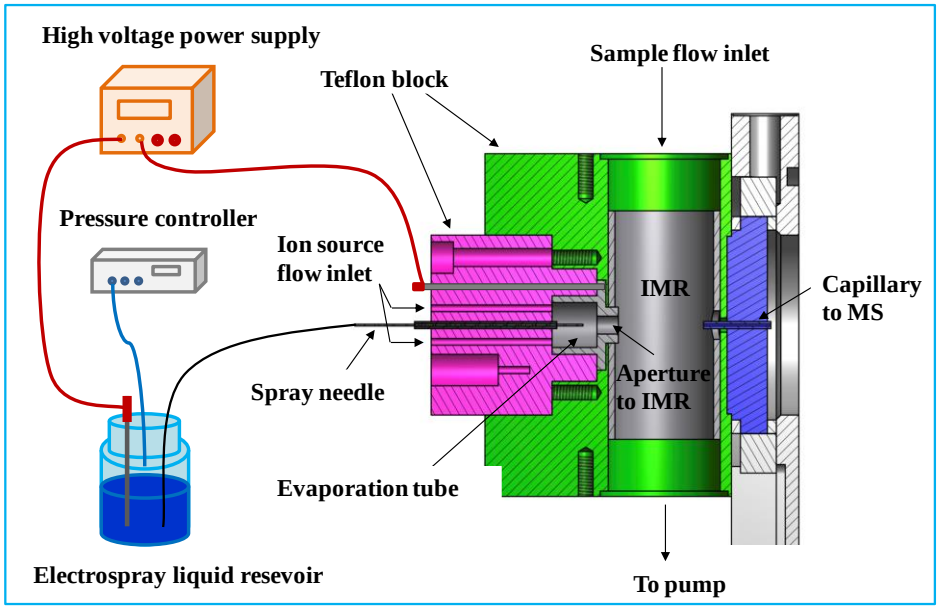

Figure 1 Schematic of the electrospray chemical ionization (ESCI) source module. Also shown are the orthogonal atmospheric pressure IMR and the entrance capillary serving as the atmospheric pressure interface between the IMR and the vacuum chamber of HRToF-MS. See text for detailed description of the source.

Ions are driven across the perpendicular sample flow to a SS capillary tube located on the opposite wall of the IMR by means of a 2 to 4 kV potential between the evaporation region lens and the capillary tube. The SS capillary projects 3.5 mm into the IMR and acts as the atmospheric pressure interface between the IMR and the vacuum chamber of a commercial

HRToF-MS (Tofwerk AG, Thun, Switzerland), effectively dropping the atmospheric pressure to 1.5 Torr in the first quadrupole of the MS, and resulting in a sample flow of ~ 270 sccm into the MS. The HRToF-MS and its data acquisition procedures have been described in detail previously (Junninen et al., 2010; Bertram et al., 2011; Lee et al., 2014). The evaporation tube, lens and IMR tube are electrically connected, while the mass spectrometer entrance capillary is electrically isolated from the IMR by a ~1 mm thick jacket of Teflon.

During operation, a dilute salt solution (~0.05 wt%) in HPLC-grade methanol (MEOH) is biased at the reservoir to +/- (2-5) kV depending on the ion mode by connecting a stainless steel rod immersed into the solution to a high voltage power supply. At a given reservoir solution voltage (V_R), the voltage applied to the evaporation tube and IMR (V_L) was carefully tuned to get the best ion signals (S_{max}), as well as the corresponding V_L, referred to as $V_L(S_{max})$. In the V_R range of 2-5 kV, a larger V_R (with a larger $V_L(S_{max})$) gives a higher reagent ion signal. To obtain good ion signals, for most of the measurements performed in this study, V_R values of 5 kV (corresponding $V_L(S_{max})$ = 2.8 kV) and -5 kV (corresponding $V_L(S_{max})$ = -3.5 kV) were used in the positive ion and negative ion modes, respectively. The reservoir is maintained at approximately 50 mbar above atmosphere using a commercial pressure controller (FLUIGENT, model MFCS-EZ) with 0.05 mbar precision. As a result, the salt solution is pushed through the fumed silica capillary tube to the spray needle at a flow rate less than 100 nL min^{-1} by the pressure in the reservoir bottle.

Under laminar flow conditions, the reaction time between reagent ions and sampled trace gases in the IMR is mainly determined by the electric field-induced drift velocity of the reagent ions. For instance, for two reagent ions used in this study, NO_3^- and Na^+, the ion-molecule reaction time (i.e., ion drift time) in the IMR is estimated to be 0.5-1 ms and 0.4-0.7 ms,

respectively, with an ion mobility of 2.37 $cm^2 s^{-1} V^{-1}$ for NO_3^- (Ellis et al., 1978) and 3.4 $cm^2 s^{-1} V^{-1}$ for Na^+ (Bohringer et al., 1987) under typical operation conditions (2-4 kV across the IMR). However, when using electrospray as a source and sampling ambient air of different humidity, the reagent ions can be solvated by methanol or water clusters (Horning et al., 1974; Garvey et al., 1994). As the ion mobility of solvated reagent ions is likely smaller than that for unsolvated reagent ions, the ion-molecule reaction time between solvated reagent ions and gas phase analytes in the IMR is expected to be longer than that estimated for the unsolvated ions. There was no evidence of protonated methanol clustering observed when electrospraying a methanolic solution of the described salts, except at extreme voltage differences between the lens and entrance capillary where it was likely that a discharge developed. Although the reagent ion is likely solvated by methanol initially, the sensitivity of the ionization to various trace gases did not appear to be significantly affected in the present study.

The ion source and sample flow rates can significantly affect the performance of the ion source. The ion source flow can aid in the generation and transport of the reagent ions into the IMR, but it may disrupt the initially laminar sample flow, especially when the sample flow is small. However, at large sample flows, the time for the ions to exit the IMR via the sample flow may be comparable to the ion drift time across the IMR at a constant potential. As a result, the sample flow may carry away the reagent ions as well as ion-molecule clusters, lowering the apparent ionization efficiency. Therefore, the ion source flow and sample flow need to be carefully optimized.

For comparison purposes, our prototype source was designed such that it could incorporate a commercial 10 mCi Po-210 inline ion source (NRD LLC) as in more typical low-pressure CIMS instruments used for atmospheric composition studies (see introduction). With

CH_3I in UHP N_2 as a reagent ion source, this set up was able to produce 0.6-1.8 × 10^6 cps of reagent ions at atmospheric pressure using an ion source flow rate of 1-2 slpm and a sample flow rate of 10 slpm, with > 2 kV potential across the IMR. Although the commercial Po-210 sources are not optimized for ion transmission at low flow rates and high pressures, this intensity is certainly suitable for use in field or laboratory studies.

Laboratory characterization

Generation of reagent ions and calibration gas standards

In this study, three negative (i.e., I^-, NO_3^-, and acetate) and four positive reagent ions (i.e., Li^+, Na^+, K^+, and NH_4^+) were generated by electrospraying their precursor salt solutions prepared in HPLC grade MEOH (Fisher Scientific). Sodium iodide (≥ 99.5%, EMD), sodium nitrate (≥ 99%, Mallinckrodt), potassium acetate (AR(ACS), Macron), ammonium acetate (99.2%, Fisher chemical), and lithium chloride (≥ 99%, Mallinckrodt) were used to produce I^- and Na^+, NO_3^-, K^+ and acetate, $NH4^+$, and Li^+ respectively. All the salts were used as received.

Three calibration gases, i.e., nitric acid (HNO_3), isotope-labeled formic acid ($H^{13}COOH$), and isoprene epoxydiols (*trans*-β-IEPOX) were used to calibrate the instrument. Gases of nitric acid and formic acid were generated using a custom-built PTFE permeation tube containing respective acid liquids, kept constantly at 40 °C. The permeation rate was determined gravimetrically. IEPOX vapor was generated by passing a flow of UHP N_2 over ~200 µl IEPOX solution in ethyl acetate kept in a glass bulb at room temperature. The concentration of IEPOX in the flow exiting the bulb was determined by an Iodide-adduct HRToF-CIMS employing a radioactive ion source, for which the sensitivity to IEPOX was calibrated using the method as

described previously (Lee et al., 2014). These three gases are common in the atmosphere and span a range in their properties important for CIMS such as acidity, polarity, and size.

Optimization of operation conditions, calibration, and background determination

The influence of sample flow and ion source flow on the ion signals was systematically evaluated using I^- as the reagent ion. The room air was directly sampled into the IMR at a flow rate ranging from 2-20 standard liters per minute (slpm). At each sample flow rate, the ratio of ion source flow/sample flow is varied from 0.02-0.2. The HNO_3 and $H^{13}COOH$ gases were added to the sample flow during the optimization.

Calibrations with HNO_3, $H^{13}COOH$, and IEPOX were performed using I^- reagent ions under optimized sample flow and ion source flow conditions. Atmospherically relevant concentrations of the calibration gases were obtained by varying the dilution of the source gas in UHP N_2 prior to delivery in the sample flow. The observed ion signals as a function of gas concentration allow the determination of the instrument sensitivity. In addition, the sample flow was humidified to a wide range of relative humidity (0-80% RH, corresponding to water vapor pressure, P_{H2O}, of 0-25 mbar) to explore the influence of water vapor on the instrument sensitivity. The determined sensitivities as well as the dependence on P_{H2O} were compared to the measurements by a radioactive Iodide-adduct HRToF-CIMS. The background signals of the instrument were determined routinely by directly sampling dry UHP N_2.

Chamber experiments of α-pinene ozonolysis

The capability of the instrument for characterizing atmospherically relevant complex organic systems was evaluated by measuring the oxidation products from α-pinene ozonolysis

using seven different reagent ions described above. Experiments of α-pinene ozonolysis were carried out in a 0.75 m^3 PTFE chamber operated in a continuous-flow mode at the University of Washington. The chamber was first flushed by 12 slpm of zero air generated by a Teledyne zero air generator (Model 701) for >72 h. Ozone, generated by flowing ultra-zero air (Praxair) at 5 sccm (standard cubic centimeter per minute) past a mercury lamp, was delivered to the chamber during the zero air flushing. α-Pinene was then added by flowing 100 sccm of UHP N_2 through a glass diffusion tube containing pure α-pinene and kept in a methanol cold trap at -70 ºC. The initial concentrations of O_3 and α-pinene added in the chamber were approximately 75 and 110 ppbv, respectively. The oxidation products formed in the chamber were sampled at 10 slpm by the HRToF-ESCIMS after 48 h of chamber equilibration.

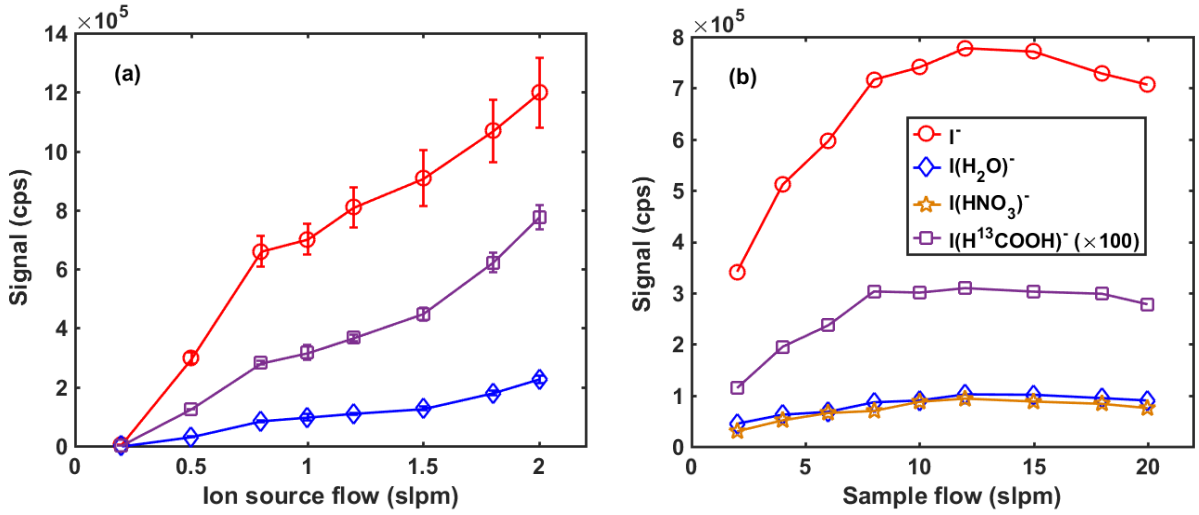

Figure 2 Dependence of ion signals on the ion source flow and sample flow. (a) Ion signals observed as a function of ion source flow during the sampling of humid room air (15 mbar water vapor pressure) containing $H^{13}COOH$ at a flow of 10 slpm. (b) Ion signals observed during the sampling of humid room air containing $H^{13}COOH$ and HNO_3 gas flow rates of 2-20 slpm (the ratio of ion source flow/sample flow is fixed to be 1:10). The signals for I $(H^{13}COOH)^-$ in (a) and (b) are magnified by 100 times.

Results and Discussion

Ion source and sample flow optimization

Figure 2a shows an example using iodide reagent ions of ion signal dependence on the ion source flow rate during sampling of humid air (P_{H2O} = 15 mbar) at 10 slpm containing an added $H^{13}COOH$ standard. As expected, the reagent ion (I^- and $I(H_2O)^-$) signals increase with increasing ion source flow. The increase of the signal for $I(H^{13}COOH)^-$ is well correlated with that of the reagent ions. The positive effect of the ion source flow is likely due to more efficient evaporation and transport of reagent ions from the spray evaporation region into the IMR region.

Figure 2b shows the ion signals for I^-, $I(H_2O)^-$, $I(H^{13}COOH)^-$, and $I(HNO_3)^-$ observed during sampling of humid air (P_{H2O} = 15 mbar) containing $H^{13}COOH$ and HNO_3 standards at a sample flow rate ranging from 2-20 slpm. The corresponding ion source flow was controlled to always be 1/10 of the sample flow. All ion signals increase initially with the increase of the sample flow, reach maximum values at 12 slpm, and then decrease slightly with further increase of the sample flow. At small sample flows, the time for the sample flow to pass through the IMR is long compared to electric field-induced ion drift time across the IMR region, and so the influence of the sample flow upon ion transit across IMR should be small. However, the corresponding increase of the ion source flow with the sample flow can promote the generation and transmission of reagent ions into the IMR, thus leading to the increase of ion signals. At large sample flows, the influence of the sample flow on the ion transit across IMR becomes significant and is no longer compensated by the enhancement in ion signals due to the increased ion source flow, hence resulting in a decrease in ion signals. Note that the same measurement was also performed at ion source flow/sample flow ratios ranging from 0.02-0.2. The trend of the

ion signal versus the sample flow at each flow ratio is very similar to that shown in Figure 2b, though the absolute ion signal values are different.

For the characterizations and applications discussed below, the sample flow and ion source flow are kept at 10 slpm and 1 slpm, respectively as these are reasonable conditions for use on environmental simulation chambers and in field measurements. We note that the sample flow can be extended to up to 20 slpm without significant loss of ion signal, and the optimal ion source flow of 2 slpm is essentially the same UHP N_2 flow requirement for current Po-210 based ion sources (Lee et al., 2014). Further improvements in the spray environment and associated transfer optics will likely further minimize the ion source flow.

Evidence of chemical ionization

Electrospray plumes not only ionize solvated analytes, but also are capable of ionizing gas phase species (Whitehouse et al., 1986; Chen et al., 1994), the latter termed secondary electrospray ionization (SESI) (Wu et al., 2000; Tam and Hill, 2004). SESI-MS has been demonstrated in the real-time analysis of a variety of gas phase analytes, including pharmaceuticals (Wu et al., 2000; Meier et al., 2012), explosives (Tam and Hill et al., 2004; Aernecke et al., 2015), human metabolites (Martínez-Lozano et al., 2011; García-Gómez et al., 2015), electronic cigarette vapors (García-Gómez et al., 2016), as well as volatile emissions from bacteria cultures (Zhu et al., 2010), food (Bean et al., 2015; Farrell et al., 2017), and plants (Barrios-Collado et al., 2016). In SESI, the electrospray plume and incoming sample flow intersect in the ionization region, and analyte ionization proceeds likely via interactions with both small charged droplets and electrospray-produced gas phase reagent ions (Wu et al., 2000). In the present study, by coupling the electrospray source to an orthogonal continuous-flow

atmospheric pressure IMR region via an evaporation region, we separate the electrospray plume from the incoming samples to avoid SESI, and instead allow for gas-phase chemical ionization.

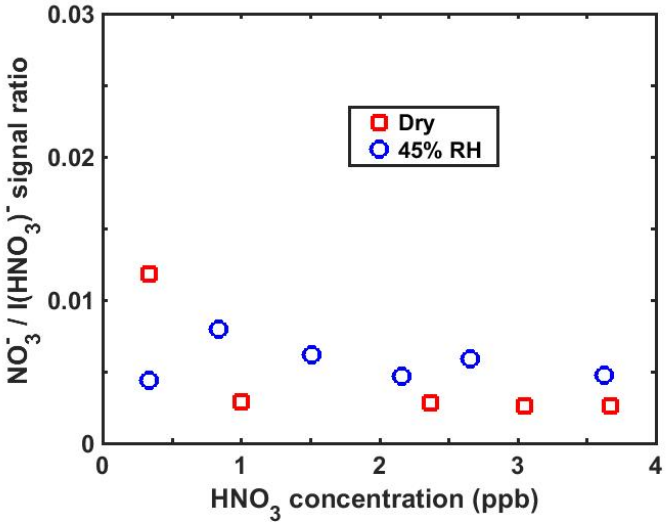

Figure 3 Signal ratio of $NO_3^-/I(HNO_3)^-$ as a function of HNO_3 concentration under dry and wet conditions observed using iodide as the reagent ion.

Under typical operating conditions, the sample flow likely transports any unevaporated droplets away from the effective ionization region in the IMR, thus largely isolating the electrospray plume from the incoming samples, making the ESCI source a chemical ionization source rather than secondary or extractive electrospray ionization (SESI or EESI) source. The evidence of the ESCI source being a chemical ionization source and not SESI or EESI is provided by monitoring the signal ratio of $NO_3^-/I(HNO_3)^-$ when sampling gas phase HNO_3 in the iodide mode. If the direct interaction between electrospray plume and incoming sample flow is important, HNO_3 dissolved in charged droplets can dissociate forming H^+ and NO_3^-, leading to the generation of NO_3^- ions in the negative ion mode. Therefore, a large signal ratio of $NO_3^-/I(HNO_3)^-$ is expected. Figure 3 shows the signal ratio of $NO_3^-/I(HNO_3)^-$ as a function of gas phase HNO_3 concentration under dry and wet conditions observed in the iodide mode. The signal

ratios of $NO_3^-/I(HNO_3)^-$ are significantly smaller than 0.01 at various HNO_3 concentrations, suggesting the direct interaction of electrospray plume with incoming samples is not important in the ESCI source.

Time response of the atmospheric pressure IMR

The time response of ESCI source/atmospheric pressure orthogonal IMR design was determined using nitric acid standard in the iodide mode. HNO_3 was delivered from a permeation tube using a small (< 100 sccm) continuous flow UHP N_2 through a 3 mm OD Teflon tube to the inlet of the orthogonal IMR. Figure 4 shows the changes in ion signal for $I(HNO_3)^-$ upon placing the HNO_3 delivery line at the opening of a 10 cm length of 2.5 cm OD Teflon tubing serving as the inlet to the IMR or removing the delivery line from the inlet. Tests were conducted at an ion source flow of 1 slpm and sample flow of 5 or 10 slpm. The increase and decay of $I(HNO_3)^-$ signal relative to that from HNO_3 in the laboratory air give an e-folding time of about 1s for nitric acid under two different flow conditions. This time response value is comparable to or better than that for the low pressure IMR (1 second to a few seconds).

Sensitivity to selected trace gases

To assess the performance of the HRToF-ESCIMS, we measured the sensitivity to HNO_3, $H^{13}COOH$, and IEPOX using I^- as the reagent ion. The iodide-based CIMS has been widely used to detect atmospheric inorganic and organic compounds in previous studies (Huey et al., 1995; Kercher et al., 2009; Lee et al., 2014; Brophy and Farmer, 2015; Lee et al., 2016; Lopez-Hilfiker et al., 2016b), though almost exclusively at low pressure (20 – 80 mbar) as opposed to the atmospheric pressure (1013 mbar) implementation used here. The sensitivity of iodide-based

CIMS to a given compound mainly depends on the polarity and hydrogen binding energy of a compound to the I^- ion (Lee et al., 2014; Iyer et al., 2016). In the atmospheric pressure ESCIMS, the ion molecule reaction time (a few ms) is set by the electric field, and is up to a factor of 30 or more shorter than those (30-120 ms) in low-pressure CIMS instruments (Bertram et al., 2011; Lee et al., 2014, Lopez-Hilfiker et al., 2016a). The shorter reaction time should linearly lower sensitivities. However, the ion-molecule collision frequency is more than a factor of 10 higher in the atmospheric pressure ESCIMS for the same ambient concentrations of analytes. Thus, we would expect the ESCIMS sensitivities to be only slightly lower than those found in the low-pressure CIMS. It is possible that adduct formation is further stabilized by third-body effects and that the ESCIMS could in fact have higher sensitivities for some compounds forming weaker clusters.

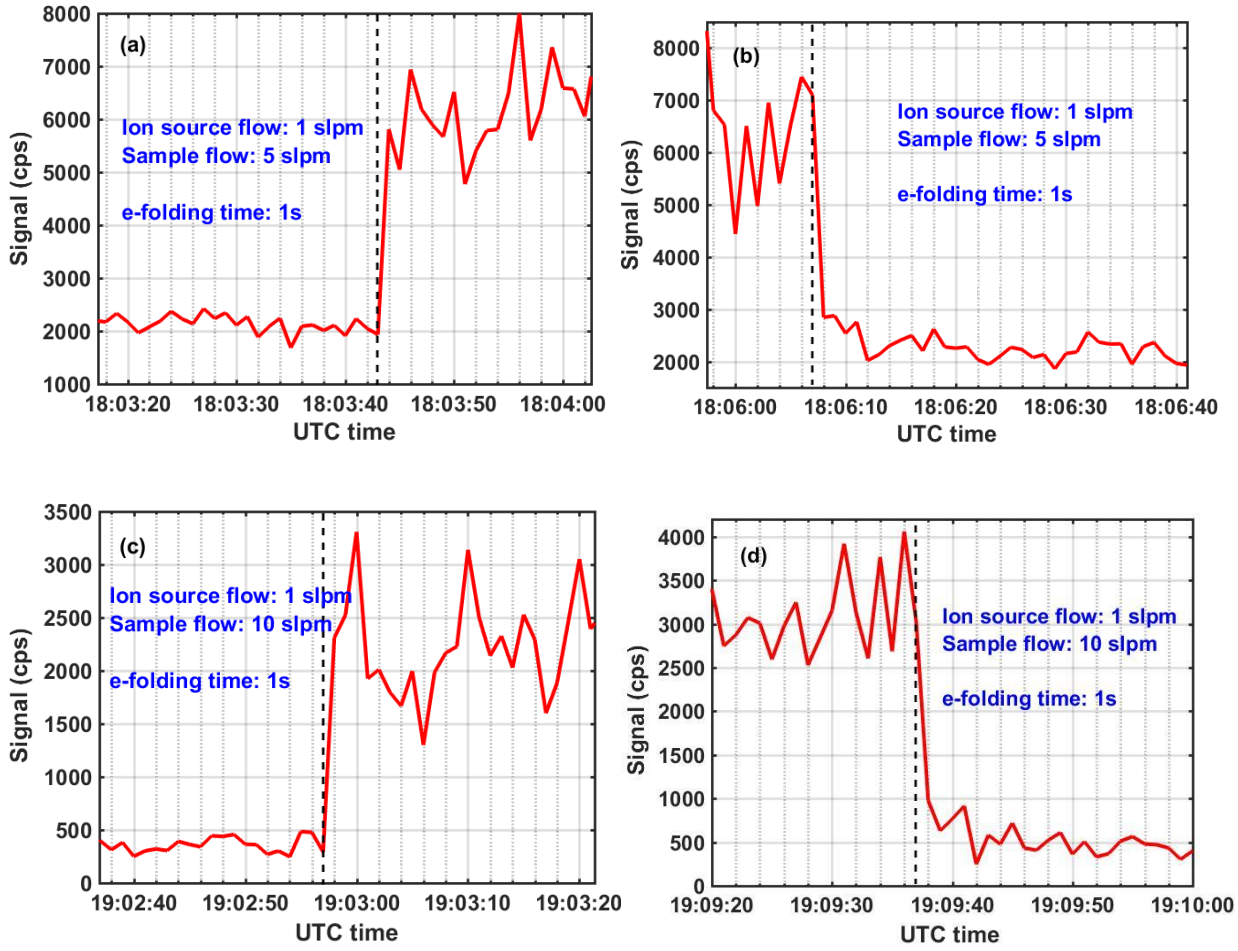

Figure 4 Time series of $I(HNO_3)^-$ observed when sampling (a, b) 5 slpm or (c, d) 10 slpm humid room air containing some ambient HNO_3 vapor. The ion source flow was 1 slpm. The dashed line indicates the time at which the HNO_3 standard gas was added or shut off.

Figure 5 shows the signals of $I(HNO_3)^-$, $I(H^{13}COOH)^-$, and $I(IEPOX)^-$ per million reagent ion count rate at different atmospherically relevant concentrations of the standards under dry and humid conditions. The signal response is linear within the investigated concentration range for all three trace gases, with the slope of the linear fit to the ion signals corresponding to the sensitivity per million reagent ion count rate. The HRToF-ESCIMS exhibits a sensitivity of 11, 2.4, and 10 cps $pptv^{-1}$ to HNO_3, HCOOH, and IEPOX, respectively, under dry conditions and 9.1, 0.5, and 1.7 cps $pptv^{-1}$, respectively, under humid conditions (P_{H2O} = 14 or 15 mbar). These

sensitivities, and those that follow are given per million cps of reagent ion. Lee et al. (2014) explored the sensitivity of a low-pressure Iodide-adduct HRToF-CIMS equipped with a radioactive ion source to a number of atmospheric inorganic and organic compounds. They reported sensitivities to HNO_3, HCOOH, and IEPOX of 4.0, 2.9, and 0.39 cps $pptv^{-1}$, respectively, at 0.2 mbar water vapor pressure in IMR. Using the same instrument as used by Lee

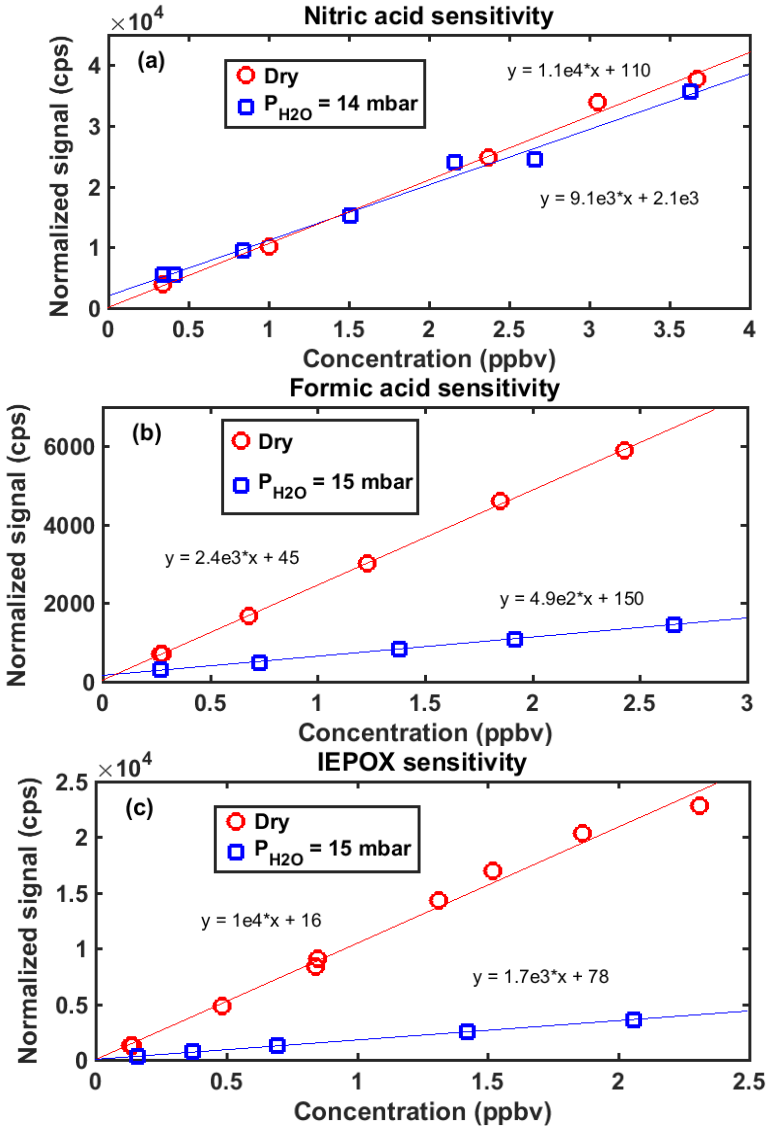

Figure 5 The sensitivity to (a) nitric acid, (b) formic acid, and (c) IEPOX under dry and humid (14 or 15 mbar water vapor pressure) conditions. Signals are normalized by the ratio of observed total reagent ion count rates to a million ion count rate. The normalized signals were observed to be a linear function of the delivered concentration. The slope derived from a linear fit corresponds to the sensitivity per million reagent ion count rates.

et al. (2014), we have more recently obtained higher values of sensitivities to HCOOH (7 cps $pptv^{-1}$) and IEPOX (10 cps $pptv^{-1}$) in the laboratory. Thus, the atmospheric-pressure ESCIMS and low-pressure CIMS approaches are fairly similar in response to the same compounds. The sensitivity difference in these calibrations is likely attributed to the differences in instrument parameters, including the configurations and pressures of the ion source and IMR, and the ion optic settings within the vacuum chamber that strongly affect ion transmission to the mass spectrometer.

The presence of water vapor can affect sensitivities, either by competing for I^- ions, thus lowering the sensitivity, or by accommodating excess energy from the collision to stabilize the Iodide-molecule clusters, thereby increasing the sensitivity (Lee et al., 2014; Iyer et al., 2016). Water vapor may also affect sensitivities by changing the size distribution of reagent ion clusters and thus their residence time (ion-molecule reaction time) in the IMR. Moreover, water vapor can affect the transmission of soluble gases through sample tubing. It is difficult to evaluate the effect of changing cluster size distribution as the information regarding the distribution and ion mobility of the reagent ion clusters is currently unavailable. In the current configuration of the ESCIMS, it is also difficult to isolate the sample transfer effect experimentally, as done previously in low-pressure IMR regions by using separate delivery lines for calibrants and water vapor (Lee et al 2014). Thus, our results shown here reflect a combination of ionization efficiency, cluster distribution, and sample transfer aspects and the latter could be significant given the 1 m length of tubing used in these tests.

Figure 6 shows the dependence of the instrument sensitivities to HNO_3, $H^{13}COOH$, and IEPOX on the P_{H2O} of the sample flow. The sensitivities to HNO_3, $H^{13}COOH$, and IEPOX increase initially with the addition of water vapor at lower P_{H2O}, reach the maximum values at

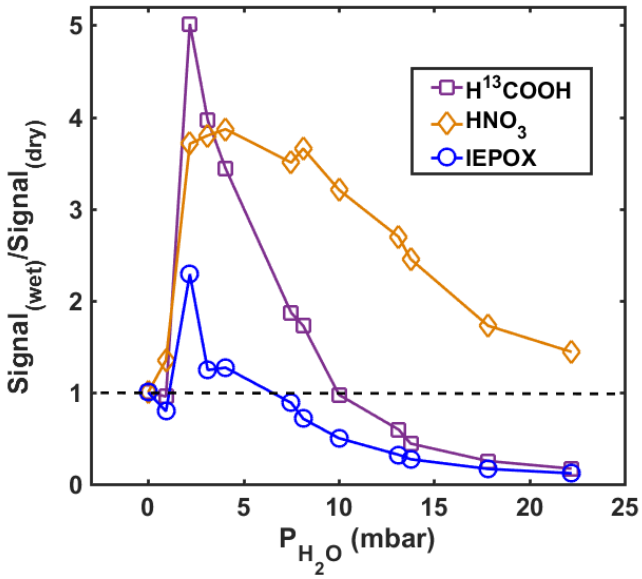

Figure 6 Normalized signal of $I(HNO_3)^-$, $I(H^{13}COOH)^-$, and $I(IEPOX)^-$ as a function of water vapor pressure (P_{H2O}) in the IMR. The signal of iodide-analyte clusters is first normalized by the total reagent ion (I^- and $I(H_2O)^-$) signals. The resulting normalized signal at each P_{H2O} was then normalized again to the respective value under dry conditions (P_{H2O} = 0, dry UHP N_2).

4.1, 2.2, and 2.2 mbar, respectively, and then decrease with the further increase of P_{H2O}. Compared to HNO_3 and $H^{13}COOH$, the positive water vapor effect on the sensitivity at low P_{H2O} for IEPOX is significantly smaller. Lee et al. (2014) investigated the effects of water vapor on the sensitivity of a low-pressure Iodide-adduct HRTOF-CIMS in the P_{H2O} (water vapor pressure in IMR) range of 0-0.8 mbar, and found a positive water vapor dependence for the sensitivity to HNO_3 and an approximately inverse U-shaped dependence for the sensitivity to HCOOH. In general, the trends for the sensitivities to HNO_3 and HCOOH versus P_{H2O} observed by Lee et al. are consistent with those at $P_{H2O} \leq 4.1$ mbar observed in the present study. In addition, recent measurements using the same low-pressure Iodide-adduct HRTOF-CIMS in our lab show that the addition of water vapor with P_{H2O} of 0.26 Torr has no significant impacts on the sensitivity to IEPOX, consistent with the relatively weak humidity dependence of the sensitivity to IEPOX at low P_{H2O} observed in the present study. The sharp decrease in the sensitivities at higher P_{H2O} as

seen in Figure 6 is therefore likely a result of the competitive consumption of I^- ions by water vapor, which dominates over the kinetic stabilization effect of water for the ion-molecule clusters, as well as a larger wall partitioning in the ~50 cm sampling tube under these conditions.

Instrument backgrounds and detection limits

The background signals for the instrument arise mainly from the impurities in the electrospray solvent and the salts used for the generation of reagent ions, as well as the

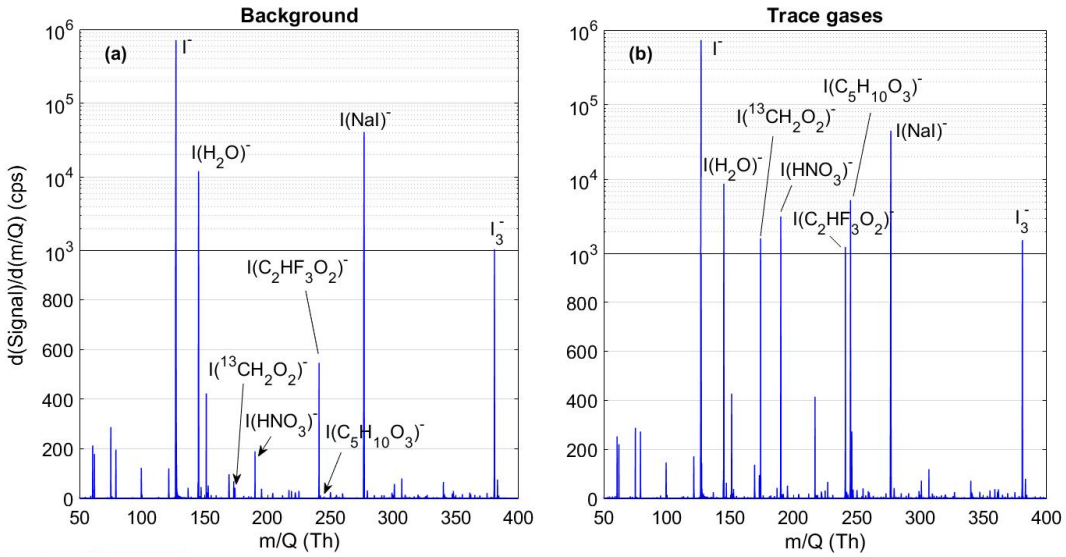

Figure 7 High resolution mass spectra collected when sampling (a) UHP N_2 and (b) UHP N_2 containing HNO_3, $H^{13}COOH$, and IEPOX gases.

desorption of gas species adsorbed onto the wall of the sampling tube and IMR. The instrument backgrounds were routinely measured by sampling UHP N_2. Figure 7 shows a typical high-resolution mass spectrum in the I^- mode recorded when sampling UHP N_2. The spectrum recorded during the addition of HNO_3, $H^{13}COOH$, and IEPOX to the UHP N_2 flow is also displayed for comparison. The typical backgrounds for HNO_3, $H^{13}COOH$, and IEPOX were measured to be 800, 240, and 50 cps, respectively. It is noted that the instrument backgrounds can be reduced by using higher purity electrospray solvents and reagent ion precursor salts, or by

using a larger sample flow that can dilute the background concentration of the species desorbed from the wall. Moreover, many experiments adding large concentrations of these standards to the sampling tube had been performed over months, and thus it is likely that these backgrounds are anomalously high.

Assuming the uncertainty in the signal and background follows Poisson counting statistics, the signal to noise (*S/N*) ratio can be determined from eq. (1) (Bertram et al., 2011):

$$\frac{S}{N} = \frac{C_f[X]t}{\sqrt{C_f[X]t + 2Bt}} \quad (1)$$

Where C_f is the instrument sensitivity; *[X]* is the concentration for a trace gas; *B* is the background count rate; *t* is the integration time. We define the detection limit of the HRToF-ESCIMS for a trace gas as the concentration that gives rise to an *S/N* ratio of 3. Using the measured instrument sensitivities and backgrounds, we calculate a detection limit of 4.9, 12.5, and 1.4 pptv for HNO_3, $H^{13}COOH$, and IEPOX, respectively, for 5s averaging, in the I^- mode. These limits of detection are comparable to those for a low-pressure Iodide-adduct HRTOF-CIMS in our lab (Lee et al., 2014).

Application to chamber studies of α-pinene ozonolysis

Raw mass spectra

Gas mixtures formed by ozonolysis of α-pinene in a steady-state chamber were used to assess the capabilities of this technique for characterizing complex organic systems of atmospheric relevance. Three negative ions (i.e., I^-, NO_3^-, acetate) and four positive ions (i.e., Li^+, Na^+, K^+, NH_4^+) were used as reagent ions for measurements. High resolution peak fitting was performed and reasonable molecular formulae were assigned for detected ions that have

intensity higher than 5 cps in all seven ion modes. Many ions are present at < 5 cps, which were excluded from the high-resolution fittings to ease the number of identifications required for comparison of several different reagent ion spectra. Although these lower signal ions might be of importance to various mechanisms of particle growth or organic radical chemistry, identifying their compositions was deemed beyond the scope of this paper. Overall, the results show that the ions observed in NO_3^- and four positive ion modes are in the form of ion-molecule clusters, whereas those observed in I^- and acetate modes are either ion-molecule clusters or molecular ions. The iodide clusters can be easily distinguished from iodide-free molecular ions due to the large negative mass defects of iodide (Lee et al., 2014), although this advantage weakens at sufficiently high masses (> ~ 500 m/Q for a resolution of 5000). In contrast, broadly distinguishing between acetate-neutral clusters and deprotonated organic ions in the acetate mode remains a challenge when using non-isotopically labeled acetate and operating the instrument in a cluster-transmitting mode with no comprehensive voltage scanning experiments (Lopez-Hilfiker et al., 2015; Brophy and Farmer, 2016), as is the case in the present study. As a result, the high-resolution ions observed in the acetate mode cannot be confidently assigned to α-pinene ozonolysis products and are excluded from further discussions.

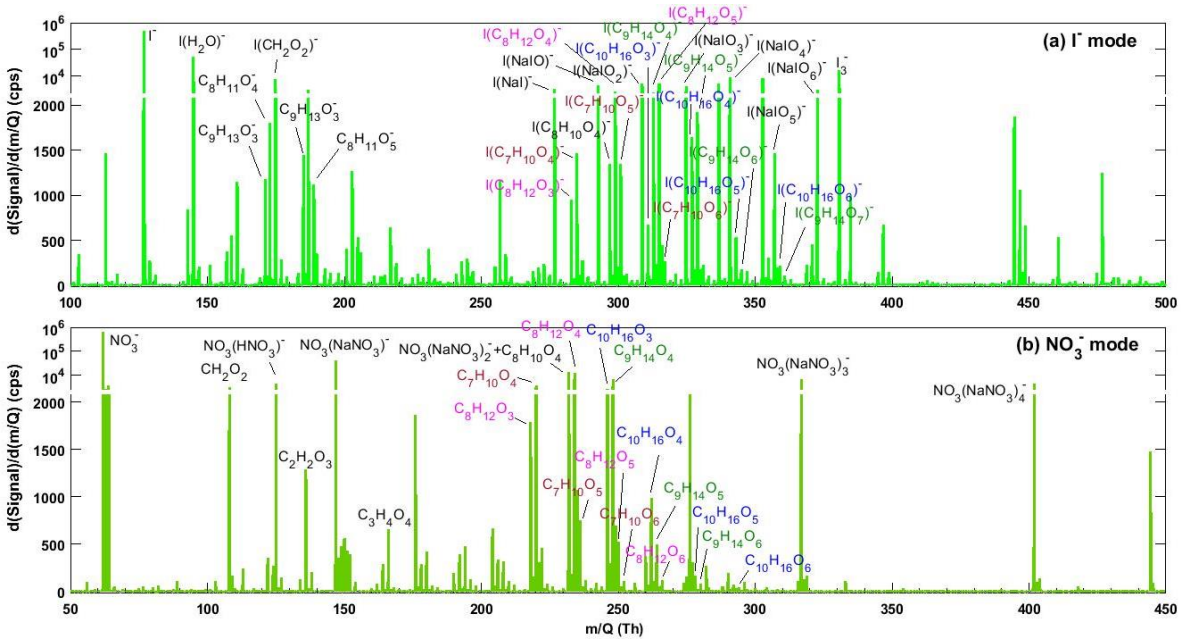

Figure 8 High resolution mass spectra obtained during ozonolysis of α-pinene in a steady-state chamber using (a) I^- and (b) NO_3^- modes. For NO_3^- mode, the chemical formulae of organic ion clusters are shown without the corresponding NO_3^- adduct for clarity as, unlike I^- mode, organic ions without a NO_3^- adduct were negligible components of the spectrum.

Examples of high-resolution mass spectra of α-pinene ozonolysis products derived in I^- and NO_3^- modes are given in Figure 8 and the spectra obtained in four positive ion modes are given in Figure 9. The iodide-mode mass spectrum of the ozonolysis products obtained here is overall similar to that obtained using the low-pressure Iodide-adduct HRToF-CIMS (see Figure S1 in the Supplement). It can be seen that peaks assigned to monomeric products ($\leq C_{10}$) are apparent in all ion modes, while peaks associated with dimeric species are evident only in the positive ion mode (discussed further below). Peak distributions in both monomer and dimer regions is very similar for Li^+, Na^+, K^+, and NH_4^+, suggesting these positive ions likely have a similar selectivity to α-pinene ozonolysis products. It is interesting to note that in negative ion modes, ion clusters of precursor salt molecules (e.g., $I(NaI)^-$ and $NO_3(NaNO_3)_n^-$) were observed with high intensities. These ions can be used as excellent mass calibration species.

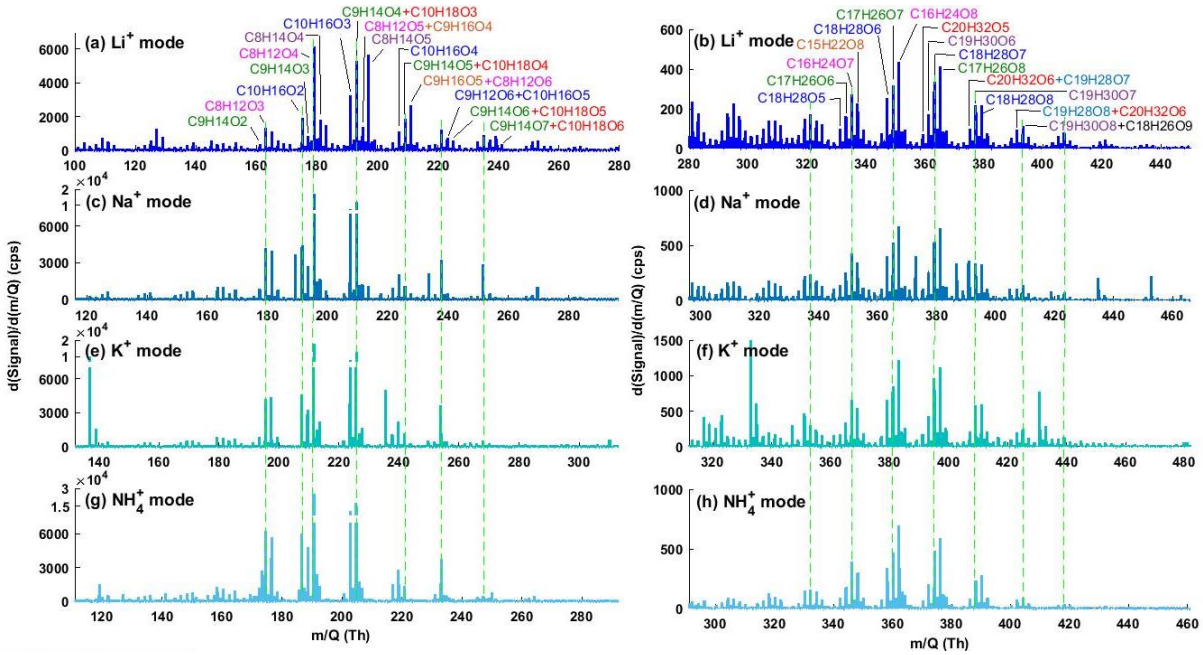

Figure 9 High resolution mass spectra of α-pinene ozonolysis products in (a, c, e, g) monomer and (b, d, f, h) dimer regions observed in (a, b) Li^+ mode, (c, d) Na^+ mode, (e, f) K^+ mode, and (g, h) NH_4^+ mode. The chemical formulae of the detected organics are given for major peaks observed in the mass spectra. To allow direct comparison, the reagent ion adduct has been removed from the detected cluster in each spectrum.

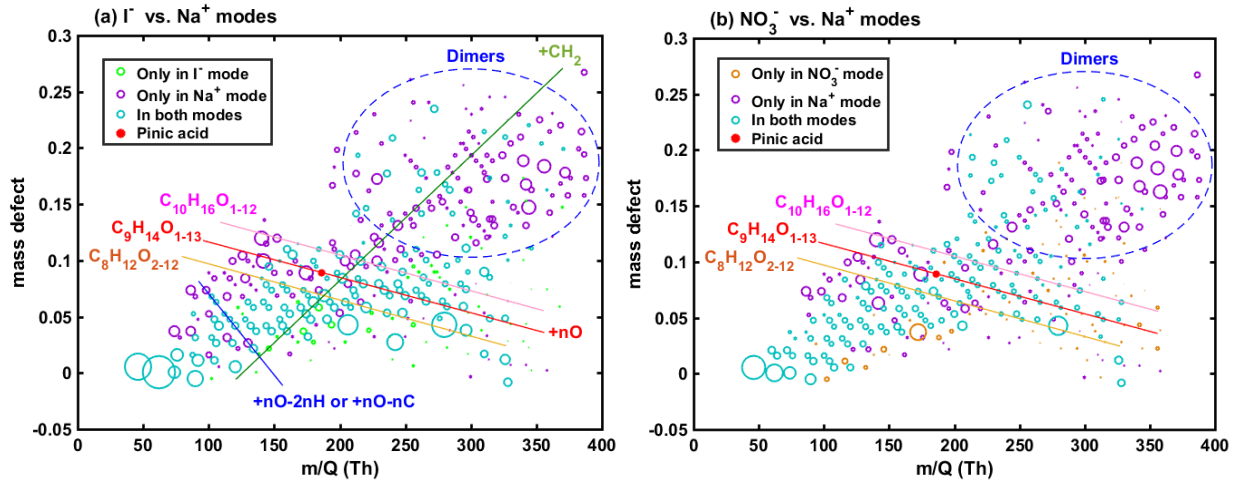

Figure 10 Comparisons of mass defect plots derived in (a) I^- and Na^+ modes, and (b) NO_3^- and Na^+ modes during ozonolysis of α-pinene in a steady-state chamber. To compare the mass defect plot obtained in two different ion modes, the reagent ions in observed clusters are excluded for the mass defect calculation, and the signals are normalized to the corresponding pinic acid intensity in each mode (see text for details). The purple circles do not necessarily mean such ions were undetected in the negative mode as they may have very small signal (< 5 cps) and be excluded from the high-resolution fitting.

Mass defect plots

To better compare the sensitivity and selectivity between this subset of negative and positive reagent ions, the mass defects of identified products are plotted against their exact mass for I^-, NO_3^-, and Na^+ modes. Figure 10 shows the comparisons of mass defect plots between I^- (or NO_3^-) mode and Na^+ mode. In the mass defect plots, the green, yellow, and purple open circles represent the products observed only in one ion mode and their size is proportional to the signal intensity of observed clusters. The blue open markers in the plots represent the products identified in both ion modes of comparison and their size is proportional to the square root of the pinic acid-normalized signal intensity ratio (*R*) between the two ion modes:

$$R = \frac{S_{A^-,i}/S_{A^-,PA}}{S_{Na^+,i}/S_{Na^+,PA}} \qquad (2)$$

Where, $S_{A^-,i}$ and $S_{A^-,PA}$ are the signal intensity of clusters for product *i* and pinic acid in I^- (or NO_3^-) mode, respectively; $S_{Na^+,i}$ and $S_{Na^+,PA}$ are the signal intensity of product *i* and pinic acid in Na^+ mode, respectively. As pinic acid ($C_9H_{14}O_4$) is among the most abundant products observed in I^-, NO_3^-, and Na^+ modes (see Figures 8 and 9), the value of *R* (i.e., the size of the markers relative to that for pinic acid (red solid circles)) can be an indicator of the relative sensitivity of I^- (or NO_3^-) and Na^+ to the oxidation products.

In the monomer region of the mass defect plots, the less oxidized products observed in both modes of comparison generally have a value of $R \leq 1$ (the blue markers have sizes smaller than or close to that of pinic acid). Thus, Na^+ is generally more sensitive to less oxidized species than I^- and NO_3^-, and most of products observed only in the Na^+ mode show very low oxygen contents ($n_O \leq 3$). As many of these species have signal intensities larger than 1000 cps, their

absence in I^- and NO_3^- modes suggests that I^- and NO_3^- are extremely insensitive to these least oxidized species, in agreement with the observations in previous studies (Lee et al., 2014; Hyttinen et al., 2015; Iyer et al., 2016). In contrast, the more oxidized products observed in both modes of comparison show a wide range of R values (e.g, $R \leq 1$ or $R \geq 1$, corresponding to the blue markers having sizes smaller or larger than that of pinic acid). This indicates that I^-, NO_3^-, and Na^+ are all sensitive to more oxidized species but have different sensitivities to a specific species. In fact, some highly oxidized products having high oxygen contents ($n_O \geq 5$) are observed only in one of these three ion modes. Note that most of these products have signal intensities lower than 50 cps, suggesting that they likely have very low concentrations, which are below the detection limit in the other two modes.

The selectivity of I^- and NO_3^- toward more oxidized species as suggested here is consistent with the observations in previous studies (Lee et al., 2014; Berndt et al., 2016), which showed that these two reagent ions can have distinct sensitivities to the oxidized species having similar oxygen contents, depending on the identities and locations of the functional groups. It is clear in Figure 10 that some very small species (e.g., CH_2O_2, CH_2O_3, $C_2H_2O_3$, and $C_2H_4O_3$) have a value of R significantly larger than 1, indicating that I^- and NO_3^- are markedly more sensitive to these small species than is Na^+.

Comparisons of the mass defect plots in the dimers region show a large difference in the detection of the gas-phase dimers between I^- (or NO_3^-) and Na^+ modes. These dimers have compositions ranging, for example, from $C_{15}H_{26}O_3$ to $C_{20}H_{32}O_7$. We note that many of these dimers have been recently detected in the gas-phase using a low-pressure Iodide-adduct HRToF-CIMS in a boreal forest environment (Mohr et al., 2017). Thus, while the lower detection efficiency of dimers in this work using I^- or NO_3^- may be from differences in reagent ion

sensitivities, we suspect that differences in ion optic settings between negative and positive ion modes that affect ion transmission efficiencies at large mass-to-charge ratios is a more likely explanation. These settings were not optimized in this work, and improvements to high mass transmission in negative ion mode are ongoing. Therefore, we refrain from making conclusions about the relative detection efficiency of dimers in negative ion mode using the atmospheric pressure ESCI.

Figure 11 shows boxplots for the O:C ratio of monomeric products from α-pinene ozonolysis detected in I^-, NO_3^-, and Na^+ modes. The O:C values for all the percentiles observed in I^- and NO_3^- modes are overall similar, whereas the corresponding values observed in Na^+ mode are obviously smaller. In addition, more than half of products observed in the three modes have a O:C ratio larger than 0.8. These results are consistent with the observations from Figure 10, where I^-, NO_3^-, and Na^+ are all sensitive to highly oxygenated organics, but the former two reagent ions are insensitive to less oxygenated organics as compared to Na^+.

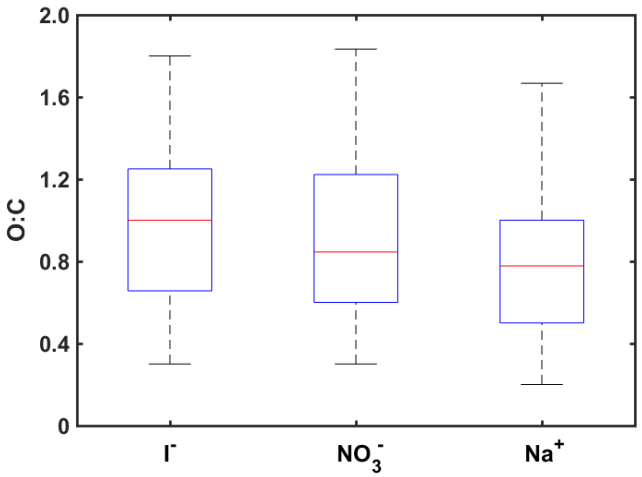

Figure 11 Boxplots showing the 5th, 25th, 50th, 75th, and 95th percentiles for the O:C ratio of monomeric products from α-pinene ozonolysis detected in different ion modes.

In summary, these comparisons suggest that there is not a reagent ion that captures all components of α-pinene ozonolysis with equally high sensitivity. Therefore, to gain a comprehensive view on a complex organic system, a combination of reagent ions with different selectivity is needed.

Declustering scans

Ion-molecule clusters, depending on their binding energies, may break apart due to collision-induced dissociation (i.e., declustering) during transmission through the ion optics within the vacuum chamber. In general, clusters with stronger binding energies can more easily survive declustering in the vacuum chamber, thus the instrument likely has higher sensitivities to the corresponding analytes, and the observed sensitivities should be closer to those calculated by ion-molecule collision rates. Declustering scanning, which is performed by systematically increasing the voltage difference (ΔV) between first and the second quadrupole sections of the MS, allows for insights into the binding energies of clusters (Lopez-Hilfiker et al., 2016a). Figure 12 shows the declustering scans of clusters containing $C_{10}H_{16}O_{2\text{-}8}$ and $C_9H_{14}O_{3\text{-}8}$ products in I^- and NO_3^- modes. It is clear that, with the increase of electrical field strength, the cluster signals for products having higher oxygen contents generally decay more slowly than those having lower oxygen contents. This is consistent with the fact that I^- and NO_3^- ions generally bind more strongly to compounds containing more hydroxy or hydroperoxy moieties (Lee et al., 2014; Hyttinen et al., 2015; Iyer et al., 2016). We note that the trends of decay for $C_{10}H_{16}O_{2\text{-}8}$ iodide clusters are in excellent agreement with previous measurements using a low-pressure iodide-adduct HRToF-CIMS (Lopez-Hilfiker et al., 2016a).

Declustering scans in Li^+, Na^+, K^+, and NH_4^+ modes show that the cluster signals for the most abundant monomeric products such as $C_{10}H_{16}O_{2\text{-}5}$ and $C_9H_{14}O_{2\text{-}5}$ increase initially with increasing ΔV and then decrease with further increase of ΔV. The reason for the initial increase in cluster signals is unclear, but might involve secondary ion chemistry and/or slight changes in ion transmission efficiency of the instrument. Here, we use the declustering scans of dimers instead of C_9 and C_{10} monomers to compare the binding energies of four positive reagent ions.

As can be seen in Figure 13, the decay rate of the cluster signals in four positive ion modes follows the order: $NH_4^+ > K^+ > Na^+ > Li^+$. This indicates an order of $Li^+ > Na^+ > K^+ > NH_4^+$ for the binding energies of the clusters, consistent with expectations from charge density considerations. In each ion mode, the cluster signals for smaller dimers generally decay more

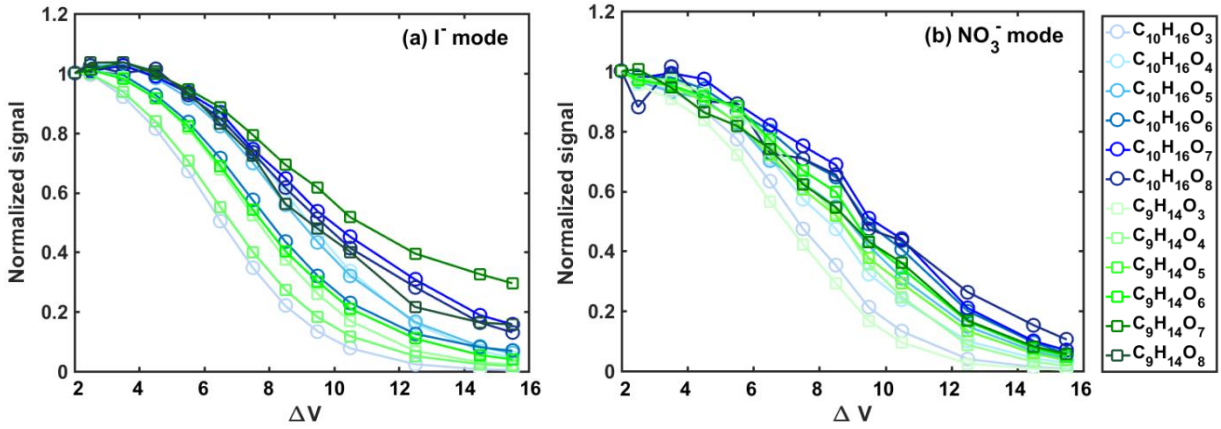

Figure 12 Declustering scans of products $C_{10}H_{16}O_{2\text{-}8}$ and $C_9H_{14}O_{3\text{-}8}$ formed by the ozonolysis of α-pinene in (a) I^- and (b) NO_3^- modes. ΔV denotes the voltage differences between the end of first and the entrance to the second quadrupole sections of the mass spectrometer. Signals at each ΔV are normalized to that obtained at the weakest declustering strength (i.e., ΔV= 2 V).

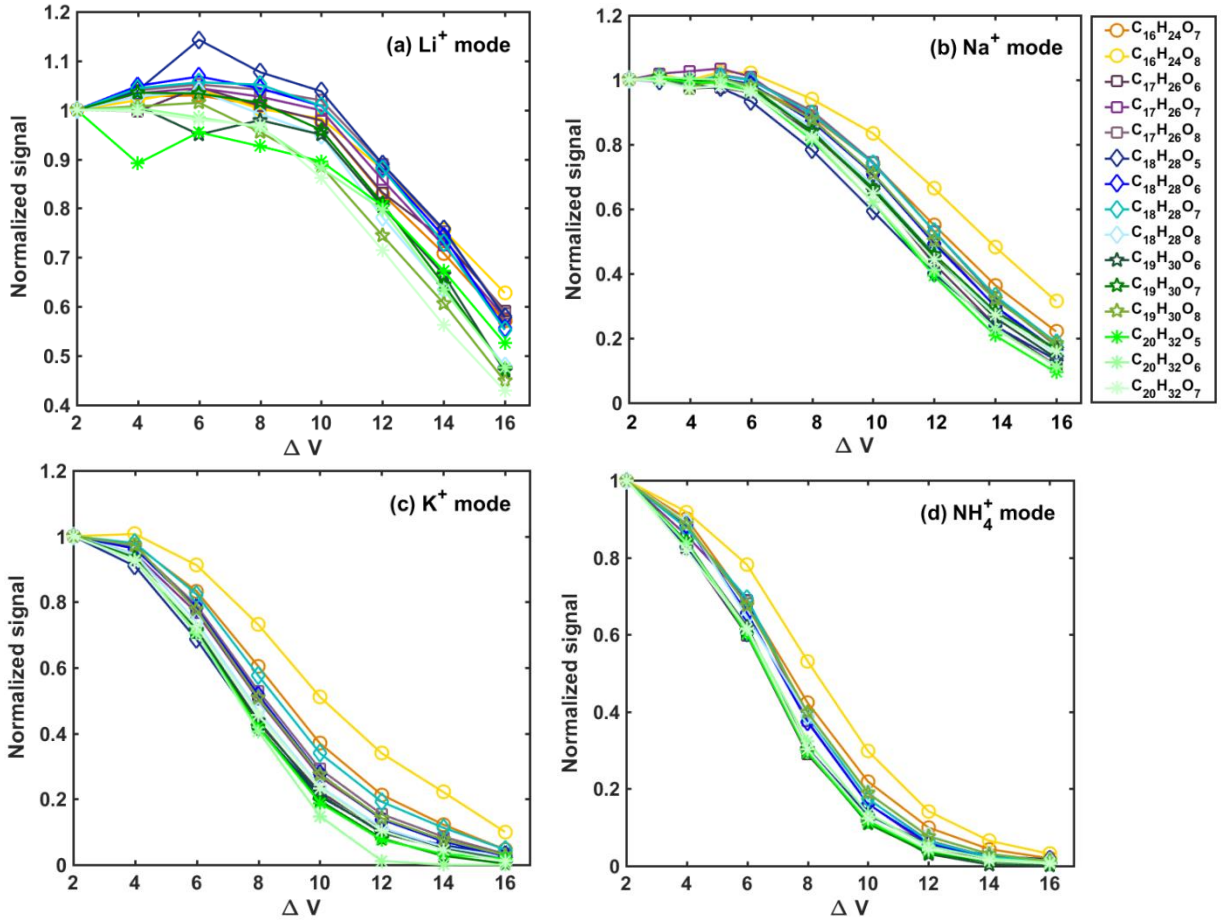

Figure 13 Declustering scans of 15 most abundant dimers formed by the ozonolysis of α-pinene in (a) Li^+ mode, (b) Na^+ mode, (c) K^+ mode, and (d) NH_4^+ mode. ΔV denotes the voltage differences between the first and second quadrupole sections of the mass spectrometer. Signals at each ΔV are normalized to that obtained at the weakest declustering strength (i.e., ΔV= 2 V).

slowly than those for larger dimers, suggesting these positive ions can more strongly bind to the smaller dimers, likely due to the higher polarity or the smaller steric effect for smaller dimers. It is worth noting that in the Li^+ mode, these dimer ions have ΔV_{50} values of ~ 15V, suggesting they are very strongly bound, with a binding enthalpy of ~ 70 kcal/mol according to the relationship between ΔV_{50} and cluster binding energies determined by Lopez-Hilfiker et al. (2016a).

Conclusion

We report an electrospray chemical ionization (ESCI) source coupled to a HRToF-MS for the real-time online measurement of atmospheric organic and inorganic species in the gas-phase. The ESCI source is unique in that it does not rely on radioactive materials or X-ray radiation that are subject to safety regulations, and allows the production of reagent ions (e.g., alkaline cations) that are not available in current CIMS techniques. Calibration experiments using nitric acid, formic acid, and IEPOX gas standards show that the HRToF-ESCIMS using iodide reagent ions has sensitivities and limits of detection comparable to those obtained for a low-pressure Iodide-adduct HRToF-CIMS using a radioactive ion source. The detection of oxidized organic compounds formed from α-pinene ozonolysis in a chamber using seven different reagent ions (e.g., I^-, NO_3^-, acetate, Li^+, Na^+, K^+, and NH_4^+) shows different selectivities for these reagent ions and expected ion-adduct binding energy trends. The data demonstrate the capability of this technique for comprehensively characterizing complex organic systems using a combination of reagent ions.

The ESCI source presented here is in its early stages of development. Continued characterization of the sensitivity and selectivity of different reagent ions, especially their dependence on humidity are needed. Further optimizations of the ion source are also required to improve its performance especially the long-time stability, which is particularly important for field applications. Versions of our prototype source allowed 10 to 24 hours of continuous operation before ion signal degraded, which is certainly suitable for many laboratory experiment durations. A short immersion of the spray tip into HPLC grade MEOH was enough to return to the same ion signal for another 10 to 24 hours, suggesting the reason was simply salt build-up on the spray needle tip altering the spray characteristics. Thus, it is likely that more dilute spray

solutions, shorter spray needle tips, a conventional coaxial sheath gas flow around the needle tip, and off-axis spray geometry would greatly improve source stability. Moreover, shifting the spray source further upstream of the entrance capillary would increase ion-molecule reaction times and thus sensitivity, as in Zhao et al. (2013). Finally, applying a dry UHP N_2 counter flow at the mass spectrometer entrance capillary would prevent ambient particles and possible charged spray droplets that are not completely evaporated from entering and blocking the capillary tube. This counter flow could also prevent free water molecules entering the vacuum chamber and promote the dissociation of reagent ion-water clusters, which may lead to an increase of the instrument sensitivity, especially in positive ion mode.

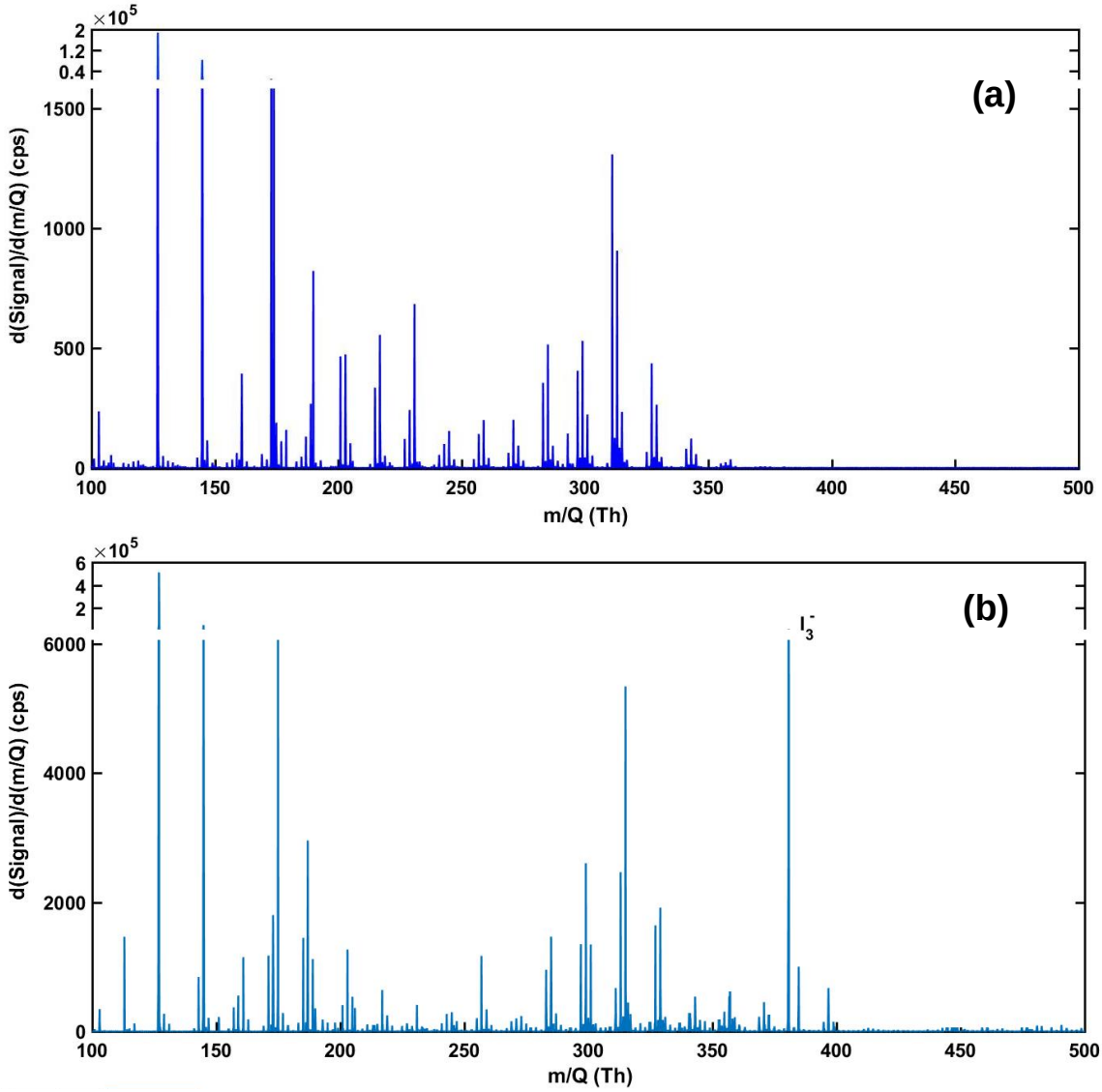

Figure S1 High resolution mass spectra obtained during ozonolysis of α-pinene in a steady-state chamber using (a) low-pressure HRToF-CIMS and (b) HRTOF-ESCIMS with iodide as the reagent ion. The peaks associated with sodium iodide salt in the ESCI mass spectrum were removed for clarity.

Chapter 2

Olfactory pollution in the anthropocene:

The impact of atmospheric NO_x and ozone pollution on plant-pollinator interactions

Chan, J. K., Parasurama, S., Xu, R., Jongebloed, U., Alexander, B., Thornton, J. A., Riffell, J. A.

Abstract

There is a growing concern about the role of sensory pollutants in impacting ecosystem function. In plant-pollinator systems, anthropogenically enhanced atmospheric oxidants such as ozone (O3) and the nitrate radical (NO3) may rapidly oxidize floral scents, but the relative sensitivity of different floral constituents to these oxidants and the physiological and behavioral impacts on pollinators and plant fitness are unknown. Using a unique nocturnal flower-moth system, we find that flower visitation by moths is severely reduced by typical atmospheric concentrations of NO3, and less so by O3. This selective importance of NO3 is caused by its relatively higher rate of reaction with monoterpenes in the floral scent. Global atmospheric models of floral scent oxidation reveal that certain urban areas, particularly those in Northern latitudes, may have extreme deficits in plant-pollinator interactions. These results illustrate the impact of anthropogenic pollutants on an animal's chemical sensing ability, and indicate that such pollutants may be critical regulators of global pollination.

Introduction

Human activities have made drastic changes to the environment, including the introduction of stimuli that are detected and processed by an animal's sensory system. Activities such as the introduction of noise, artificial lights, or anthropogenic chemicals can all potentially be detected by an animal's sensory system and lead to changes in behavior (Hafwerk and Slapperfkorn, 2015; Dominoni et al., 2020). The behavioral and physiological impacts of these anthropogenic inputs to the sensory systems, termed sensory pollutants, have received growing interest. Sensory pollutants in the form of artificial lights and sound have been found to negatively affect organismal behaviors, including predator avoidance and intraspecific interactions (e.g. mate-searching behavior). Examples include the noise from cars or heavy machinery that influences the behaviors of birds, mammals, and insects, by altering their abilities to perceive predators or detect prey (Siemers et al., 2011; Dominoni et al., 2020). Light pollution in urban areas has been implicated in the mortality of migrating birds (Firebaugh and Haynes, 2016). Despite the potential ecological effects of sensory pollution, studies have rarely linked the neural bases by which sensory pollutants influence animal behavior, with how those behavioral changes impact the abundances, distributions and interactions of organisms in the field.

In contrast to how auditory and visual pollution impacts organismal behavior, much less is known about the effects of airborne pollutants on organismal chemical communication systems and the corresponding ecological impact. Plants and their pollinators have become an excellent model to examine how olfactory pollutants impact ecological interactions. Of particular concern in this regard are nocturnal pollinators which navigate over long distances to locate patches of flowers (Il, 1976; Raguso et al., 2003; Schiestl, 2015), and use their sensitive olfactory

systems to locate and discriminate between floral resources (Riffell et al., 2008b; Riffell et al., 2013). Floral scents consist of a diverse mix of chemicals (Knudsen et al., 2006), the identities and ratios of which are important for learning and visitation to flowers (Riffell et al., 2008b). Thus floral volatile organic compounds (VOCs) play a crucial role in plant reproductive success by affecting pollinator behavior. However, floral scents are subject to anthropogenic disruptions that influence pollinator behaviors and potentially weakening plant-pollinator interactions. For example, anthropogenic pollutants can mask floral scents (Riffell et al., 2014) and degrade the chemicals of the scent (Girling et al., 2013, Farre-Armengol et al., 2015, Saunier & Blande, 2019, Vanderplanck et al., 2021, Fuentes et al., 2016), thereby suppressing the ability of pollinators to perceive scent signals (Dotteryl et al., 2016, Demares et al., 2022). A handful of laboratory studies have demonstrated the impact of anthropogenically enhanced oxidants, including ozone (Farre-Armengol et al., 2015) and NO_x pollution from diesel exhaust (Girling et al., 2013, Ryalls et al., 2022), on odor recognition by pollinators. Unfortunately, these studies often do not reflect the natural spatial and temporal dynamics of atmospheric processing of the odor in the field. A recent study by Ryalls et al. (2022) demonstrated the impacts of diesel exhaust on pollinator visitation and plant reproductive success in the field, but the chemical processes involved were not elucidated.

Members of the evening primrose family (Onagraceae) and it's pollinators provide an excellent system to understand the impacts of anthropogenic pollutants on plant-pollinator interactions. *Oenothera* spp. and their pollinators are exemplars for pollination systems in semi-arid environments, due to the rich diversity of pollinators that the flowers attract, which covers all major pollinator groups (Table S1A, Fig. S1A). *Oenothera pallida* (hereafter, *O. pallida*) grows in the North American Deserts ecoregions (Fig. S1A) where it is an important resource for

many pollinators, including crepuscular hawkmoths (*Hyles lineata*, *Manduca* spp.) that are regional specialists on *Oenothera* (Gregory, 1963; Krakos and Fabricant, 2014). Hawkmoths and other pollinators navigate over kilometers between patches of *Oenothera* and use their sensitive olfactory system to locate the patches of flowers (Il, 1976). In these areas, hawkmoths and *Oenothera* will experience varying levels of anthropogenic- and naturally-produced levels of ozone (O_3) and NO_3, with NO_3 having elevated levels near or downwind from urban centers (Huang et al., 2017). Therefore, the *Oenothera*-pollinator system provides an excellent model to examine the impacts of free radicals on pollinator behavior and flower visitation.

Volatile organic compounds (VOCs), including the scent compounds emitted from flowers, are degraded in the atmosphere by reaction with hydroxyl radicals (OH), nitrate radicals (NO_3) and ozone (O_3). During the daytime, O_3 reacts with water vapor in the presence of sunlight to form OH, which is the primary atmospheric oxidizing agent in the atmosphere during the daytime. However, at night NO_3 dominates due to reaction of O_3 with NO_2 to form NO_3 and the lack of sunlight that would otherwise rapidly decompose NO_3 to NO_2 and O (Fig. 2C) (Graham & Johnston, 1978; Ng et al., 2017).

In this manuscript, we examine the behavioral and chemical processes mediating plant-pollinator interactions in the anthropocene. We present findings from (i) pollination and behavioral studies of pollinator visitation to *O. pallida*; (ii) electrophysiological characterization of hawkmoth responses to *O. pallida* scent (iii) analyses of the degradation of floral scents from field-relevant levels of O_3 and NO_3; (iv) lab and field behavioral experiments showing the elimination of pollinator visitation due to NO_3 degradation of floral scents; and (v) modeling the global impacts of O_3 and NO_3 on pollinator detection of floral scents. Using this integrative

approach, we show that olfactory pollutants may dramatically suppress plant-pollinator interactions in the anthropocene.

Results

Characterizing *O. pallida* pollination.

To understand the importance of various pollinators to *O. pallida*, we conducted pollinator observation and exclusion experiments at field sites located at Grants Pass WA where 1 to 5 plants with 5-70 flowers were observed for 110 hours at night and 90 hours in the day for a total of 200 hours. During our observations, flowers were visited by diverse pollinators (Fig. 1B, Fig. S1A, Table S1A), particularly nocturnal hawkmoths and diurnal bees. Diurnal pollinators include multiple species of bees (mainly *Megachile, Apis mellifera, Andrenidae* and *Lasioglossum*), wasps, flies, moths and butterflies. Nocturnal and crepuscular pollinators include moths (mainly hawkmoths including *Hyles lineata* (hereafter, *Hyles*) and *Manduca sp.* (hereafter, *Manduca*)) and *Lasioglossum* bees. To assess the contribution of the various pollinators to *O. pallida* pollination, we conducted a series of pollinator exclusion treatments, including bagging (to prevent pollinator visits) and cross-pollinating individual flowers, which were tagged and later assessed for fruit set. Plants in bagged, self-pollinated treatments had significantly lower fruit set than unbagged plants (pairwise comparison of proportions with Holm correction: $P<0.001$) (Fig. 1, C-D; Table S2A, B). Exclusion of nocturnal pollinators also resulted in a lower fruit set than no-treatment controls (pairwise comparison of proportions with Holm correction: $P=0.0082$), consistent with findings from Gregory (1964) that white-flowered night-blooming *Oenothera* species in the southern

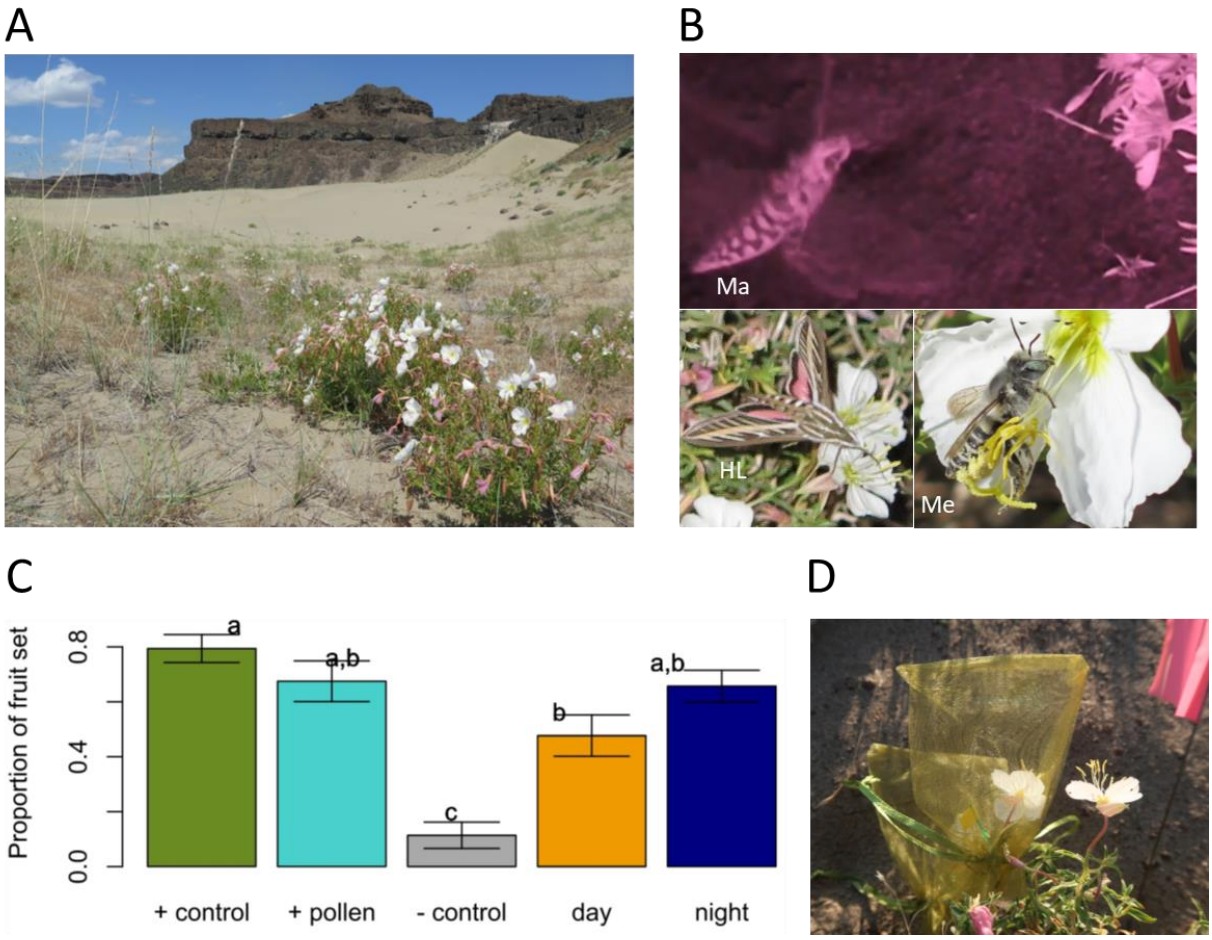

Figure 1 A: Example of *Oenothera pallida habitat* in sandy areas in sagebrush steppe of the Columbia Plateau (Echo basin, WA USA). **B**: Major pollinators of ***O. pallida*** including Ma (*Manduca species)*, HL (*Hyles lineata*), Me (*Megachile species*). **C**: Pollinator exclusion treatments + control (no-treatment control), + pollen (total exclusion with manual cross-pollination), - control (total exclusion treatment), day (nocturnal and crepuscular pollinators excluded), night (diurnal pollinators excluded). Significant differences denoted by letters above the bars, with displayed standard deviation bars. **D**: Picture of pollinator exclusion setup where individual flowers are bagged with green organza bags.

USA are pollinated primarily by hawkmoths, including *Hyles lineata* and *Manduca spp.* These hawkmoths use their olfactory sense to navigate over kilometer distances and locate patches of *Oenothera* flowers (Il, 1976). At our field site, *Hyles* and *Manduca* (primarily *M. quinquemaculata,* and to lesser extent *M. sexta*) were observed to visit *O. pallida* flowers throughout the night, with *Hyles* being a more frequent visitor than *Manduca* (Table S1A).

Atmospheric oxidation of critical *O. pallida* scent compounds.

O. pallida has white flowers which are ~4 cm in diameter and emit a high intensity scent. To first characterize the *O. pallida* floral scent and identify bioactive compounds that are important for hawkmoths, we collected scent samples in the field using dynamic sorption and analyzed the samples using gas chromatography with mass spectrometry (GCMS) (Fig. S3A, Table S3A). To identify volatile compounds that hawkmoths might use to detect the flowers, we performed gas chromatography coupled with electroantennographic detection (GC-EAD) using male *Hyles lineata* and *Manduca sexta* moths (Fig. 2A, Fig. S3B). Both hawkmoths responded to similar compounds in the *Oenothera* scent, including monoterpenes like cis-β-ocimene and β-pinene; nitrogenous compounds like 2-methylbutanal oxime; and aromatics like methyl salicylate (Fig. 2B). An odor mixture of the 12 chemicals that elicited strong antennal (olfactory) responses (Table S5) was created in mineral oil for use in subsequent laboratory experiments (Table S4).

To examine the relative atmospheric degradation of floral VOCs by NO_3 and O_3, we used an atmospheric pressure flow reactor coupled to a time-of-flight mass spectrometer (LToF, TOFWERK AG, Thun, Switzerland) with chemical ionization by benzene cations (Lavi et al., 2018) and proton-transfer reactions (VOCUS PTR, TOFWERK AG, Thun, Switzerland) (Krechmer et al., 2018) to measure the concentrations of floral volatiles in real time (Fig. 2D). This system allowed us to measure degradation of the floral volatiles under realistic atmospheric conditions. Exposure of the floral scent to both O_3 and NO_3 showed that NO_3 dramatically decreased the concentrations of certain constituents in the scent, particularly the monoterpenes, whereas other scent compounds, like 2-methylbutanal oxime, showed little change in

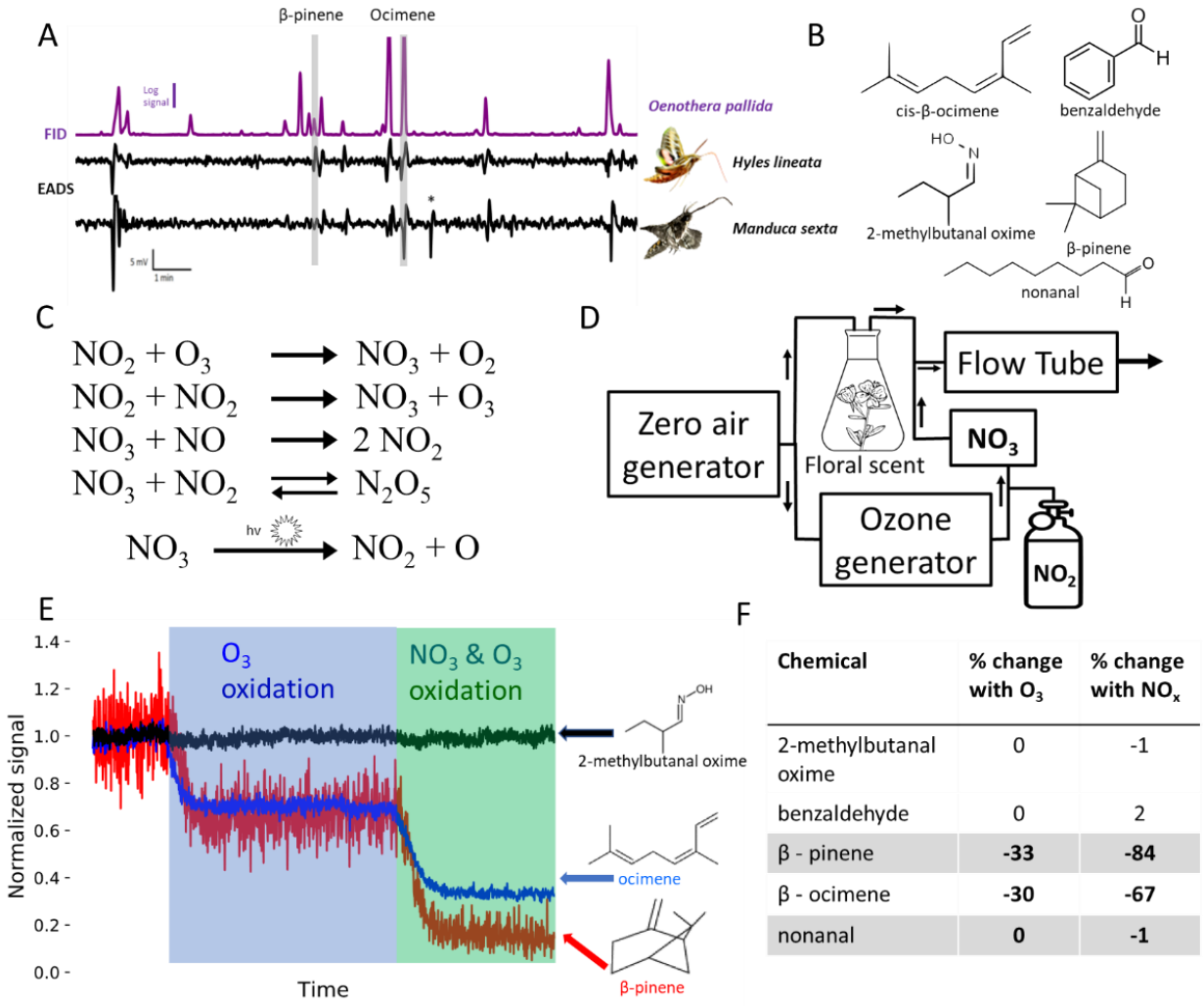

Chemical	% change with O_3	% change with NO_x
2-methylbutanal oxime	0	-1
benzaldehyde	0	2
β - pinene	**-33**	**-84**
β - ocimene	**-30**	**-67**
nonanal	**0**	**-1**

Figure 2 A: GC EAD traces of male *Hyles lineata* (top) and *Manduca sexta* (bottom) antennal response to *Oenothera pallida* night scent sample from the field. Responses to the monoterpenes β-pinene and ocimene are highlighted in gray. *Hyles* responds to β-pinene whereas *Manduca* does not. *, response not repeatable. **B**: Structures of key components of *O. pallida* scent that the moths are responsive to. **C**: Chemical equations for the formation of the nitrate radical (NO_3) from nitrogen dioxide (NO_2) and ozone (O_3). Dinitrogen pentoxide (N_2O_5) forms reversibly from NO_3 and NO_2, and acts as a reservoir of NO_3. During the day, ultraviolet light causes the dissociation of NO_3 to NO_2 and O, preventing the buildup of NO_3. **D**: Schematic of the setup for generating NO_3 from NO_2 and O_3, and oxidizing the floral scent blend in a flowtube. **E**: Example normalized traces of NO_3 and O_3 oxidation of 2-methylbutanal oxime, β-pinene, and ocimene, measured with a Vocus-PTR-TOF mass spectrometer. **F**: Table of measured volatiles and their degradation rates under NO_3 and O_3 oxidation (all differences $p < 0.001$, Welch t-test/Mann-Whitney U-test, Table S6). The O_3 and NO_2 concentrations in the flowtube were 120 ppb and 60 ppb respectively, which correspond to the upper range of highly polluted urban environments (Huang et al., 2017, Khan et al., 2015). The reaction time in the flowtube was 73 seconds which simulates the impacts on odor transmission within 100m from the odor source.

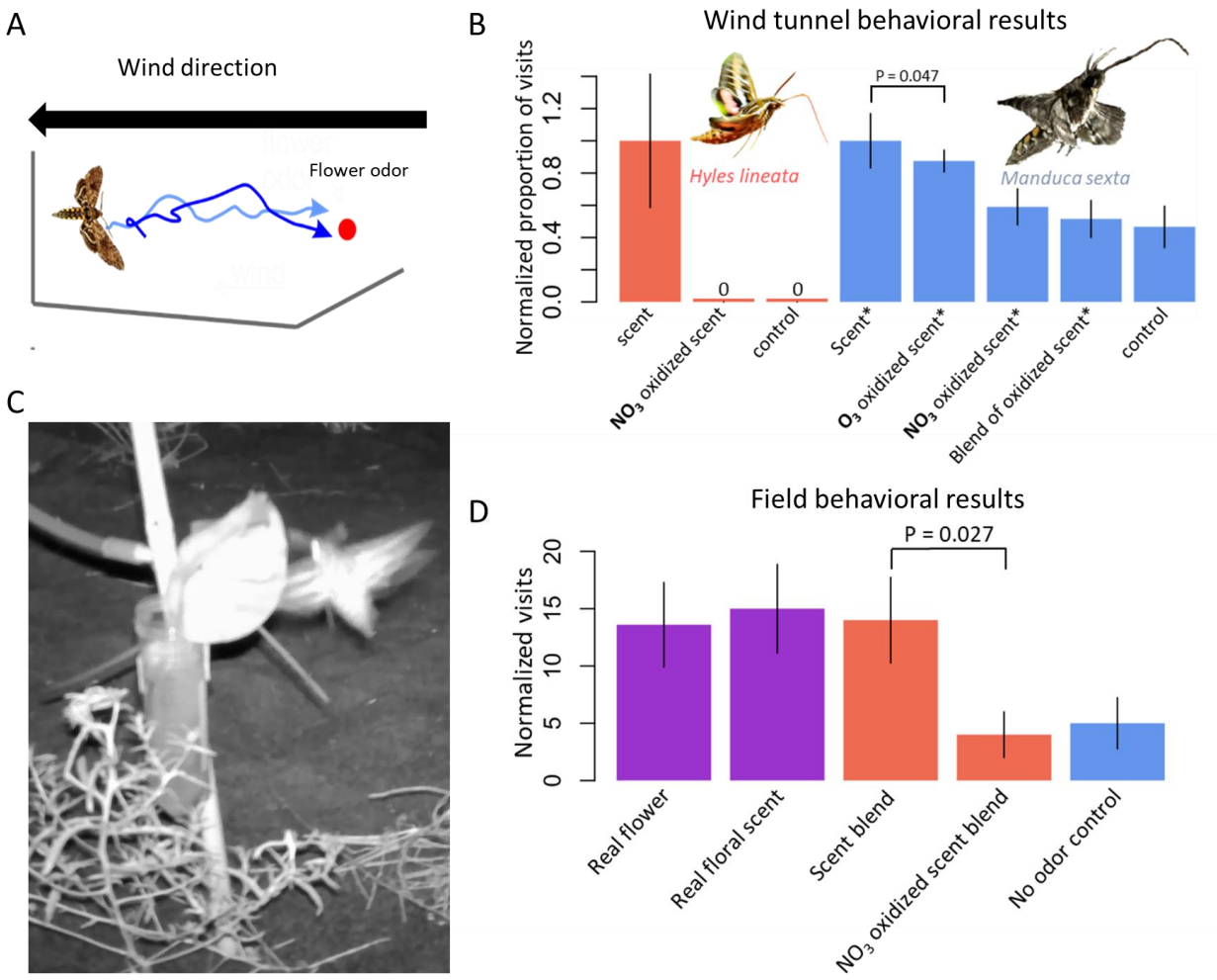

Figure 3 A: Diagram of hawkmoth flight path in the wind tunnel upwind towards the scent source. Photograph of a *Hyles lineata* visiting a scent treatment in the field. **B**: Wind tunnel behavioral results for *Hyles lineata* (coral) and *Manduca sexta* (blue) at 0.5 m/s laminar airflow. Individual naive male moths were released 1.5m directly downwind of the odor source, and the proportion of moths that attempted feeding from the source was recorded. The scent blend presented the same emission rate of the component chemicals as a single flower of *Oenothera pallida*. Blue bars and * indicate treatments done using 100x diluted scent blend. The visitation proportions for each set of treatments was normalized to the proportion of visits to the scent treatment. Error bars indicate standard error. NO_3 oxidation conditions are equilibrium N_2O_5 from 120 ppb O_3 and 60 ppb NO_2 at room temperature with 73s reaction time in a glass flowtube. O_3 and NO_2 oxidation conditions include just the O_3 or NO_2 component of the NO_3 treatment. Controls were done with dry, filtered air. Another scent treatment of 'blend of oxidized scent' was performed with a scent blend containing 84% less β-pinene and 67% less ocimene than the original scent blend to simulate oxidation by O_3 and NO_3. **C**: Photograph of a *Hyles lineata* visiting the humidified paper cone of a scent treatment embedded in a *O. pallida* plant in the field. Image taken by frame capture from video from a DVC video camera, illuminated by 850nm infrared light. **D**: Field behavioral results showing normalized number of visits to a single scent source of each treatment. Five treatments were performed simultaneously including a real flower treatment, real floral scent treatment, scent blend treatment, O_3 and NO_3

oxidized scent blend treatment, and clean air control. All treatments except the real flower treatment involved air from the scent treatment delivered through a humidified filter paper cone. A total of 49.5 hours of experiments was performed, but not all treatments had 49.5 hours of usable data due to camera malfunctions, so the total number of visits was normalized to a total observation time of 49.5 hours. Observations for the visits to the real flower treatment were multiplied by the number of flowers each hawk moth visited on the plant, and divided by the total number of flowers on the plant.

concentration (Fig. S2). To quantify the relative impacts of NO_3 and O_3 on the scent constituents, each compound was individually released into the flowtube and the change in concentration due to reaction with the oxidants were quantified. Similar to our results with the floral scent blend, certain compounds were more sensitive to degradation than others, especially the monoterpenes (e.g., β-pinene and β-ocimene). However, while β-pinene and β-ocimene were sensitive to oxidation by ozone (decreased by 33% and 30% respectively), the compounds were severely degraded in the presence of NO_3 (decreased by 84% and 67% respectively; $p < 0.001$, Welch t-test/Mann-Whitney U-test, Table S6)(Fig. 2 D-F), emphasizing the important role of NO_3 in the atmospheric oxidation of these scents. These scent compound responses are consistent with the set of known rate constants for their reactions with O_3 and NO_3 (IUPAC-AERIS) and the importance of atmospheric NO_3 for monoterpene fate even at much lower concentrations than O_3 (Edwards et al., 2017).

Atmospheric oxidation of floral scents suppresses hawkmoth attraction and plant-pollinator visitation.

To determine how atmospheric oxidation affects hawkmoths' ability to locate *O. pallida* scent sources and flower visitation, we first performed behavior experiments in a laboratory wind tunnel. The wind tunnel enabled reproducible simulation of the physicochemical conditions present in the field and determining the impacts of NO_3 and O_3 levels found in both polluted

urban and near-pristine environments (Fig. 3A). For both hawkmoth species, NO_3 oxidation of the floral odor reduced the ability of the hawkmoths to locate the flowers. For *Hyles*, NO_3 oxidation of the floral odor eliminated their behavioral attraction (Fig. 3B). For *Manduca*, which was more sensitive to the floral odor (Fig. S4A, B), NO_3 oxidation resulted in a 50% decrease in *Manduca* visitation rate ($p = 0.047$, comparison of population proportions), and to a level that was not significantly different from the clean air control. By contrast, O_3 oxidation of the floral odor at O_3 concentrations typical of the atmosphere had no significant impact on hawkmoth visitation (Fig. 3B).

Results from our flow reactor experiments showed that monoterpenes were selectively degraded to NO_3 exposure given the concentrations and limited timescales of exposure. To investigate if the decrease in concentration of monoterpenes in *O. pallida* scent was responsible for the loss in attraction, an artificial mixture was created to simulate selective depletion of monoterpenes to levels similar to that observed after NO_3 exposure in the flow reactor. The artificial mixture (with 84% less β-pinene and 67% less β-ocimene) was tested in the wind tunnel and resulted in significantly lower behavioral responses compared to the synthetic floral odor, and was not different from the clean air control nor the NO_3-degraded scent. Importantly, controls consisting of floral odor that was exposed to nitrogen dioxide (NO_2) or O_3 alone were not significantly different from responses to the untreated floral odor.

How might oxidation of floral scents impact plant-pollinator interactions and pollinator visitations in a field setting as opposed to the laboratory? To answer this question, we determined how atmospheric oxidation affects hawk moths' ability to locate *O. pallida* scent sources in the field. We conducted various scent treatments in the field (Fig. 3C, Table S7B, S7C) to determine the difference in visitation rates to different treatments. Visitation rates to the floral odor, both

real floral scent (1 flower) and our floral odor mimic, and to real flowers (per flower) were not significantly different. By contrast, the visitation rate to floral odor exposed to NO_3 was significantly lower than to the untreated odor ($p = 0.027$, GLM, Poisson, logistic link, Table S7B-S7D), and not significantly different from the clean air control (Fig. 3D). To establish the effects of scent oxidation on fruit set, we determined the number of visits per night with the fruit set per moth visit. From our experiments, an untreated *O. pallida* flower is visited by a hawkmoth approximately twice per night (1.9 +/- 0.9), whereas flower visitation in the oxidized scent treatment fell to 0.57 (+/- 0.28) visits per night, or a 70% (+/- 20%) drop in visitation. Since visitation by hawkmoths accounts for 40% (+/- 10%) of all successful fruits (Table S2A), a 70% drop in visitation may cause a 28% (+/- 11%) reduction in fruit set. Although these results do not take into account the effects of diurnal pollinators, such as bees, some of which are sensitive to pollutants (Ryalls et al., 2022, Vanderplanck et al., 2021, Demares et al., 2022, Dotteryl et al., 2016, Girling et al., 2013), nor other nocturnal pollinators (microlepidoptera), they do illustrate the potential impact of field relevant concentrations of NO_3 and O_3 on plant-pollinator interactions.

Global modeling of pollinator olfactory navigation impacts.

Results from the above laboratory and field experiments suggest that floral scent and associated pollinator attraction is especially sensitive to NO_3 oxidation. NO_3 dominates nighttime oxidation of biogenic VOCs, particularly near and downwind of urban areas where nitrogen dioxide and O_3 are elevated. To estimate potential impacts of anthropogenic enhancements to O_3 and NO_3 concentrations on pollinator olfactory navigation, we used global fields of O_3 and NO_3 concentrations simulated by the GEOS-Chem global chemical transport model, focusing on July

and January when these pollinators are typically most active in the northern or southern hemisphere, respectively (Haber and Frankie, 1989; Satterfield et al., 2020). Floral scents that are attractive to hawkmoths and other pollinators are dominated by monoterpenes, including β-pinene and β-ocimene (Knudsen et al., 2006). Using known rate constants for reactions of monoterpenes with O_3 and NO_3, we calculated the distance for floral scents to be oxidized to a level unrecognizable by hawkmoths , given the simulated concentrations of O_3 and NO_3 in a given location and assuming a mean surface wind speed of 1 m/s under stable conditions (Mylne, 1992). A scent recognition distance was computed for each location and month, and plotted as a series of global maps illustrating the differing impacts of NO_3 and O_3 on pollinator olfactory navigation. Results show that NO_3 degradation of floral scent has a more severe impact on recognition distance than O_3 alone (Fig. 4 A, B), and that scent recognition distances are often below 400 m in many populated areas. Regions with the most severe impacts from NO_3 include North America, Europe, Central Asia, the Middle East, and southern Africa. In addition, we performed a simulation of the pre-industrial atmosphere using GEOS-Chem to assess the percent change in scent recognition distance that has occurred since the pre-industrial era (Fig. 4C). The pre-industrial comparison map shows that in most populated regions of the world, current scent recognition distances are often below 25% of pre-industrial distances (Fig. 4C). In certain sparsely populated areas (e.g., Alaska USA, and Greenland), NO_3 concentrations have increased relative to pre-industrial levels, but these changes are relatively small and do not impact the scent recognition distances which remain above 1000 m. In other areas (Central Asia and Southern Africa), scent recognition distances remain unchanged relative to pre-industrial times because of natural NO_x emissions, illustrating the differential impacts of natural and anthropogenic NO_x

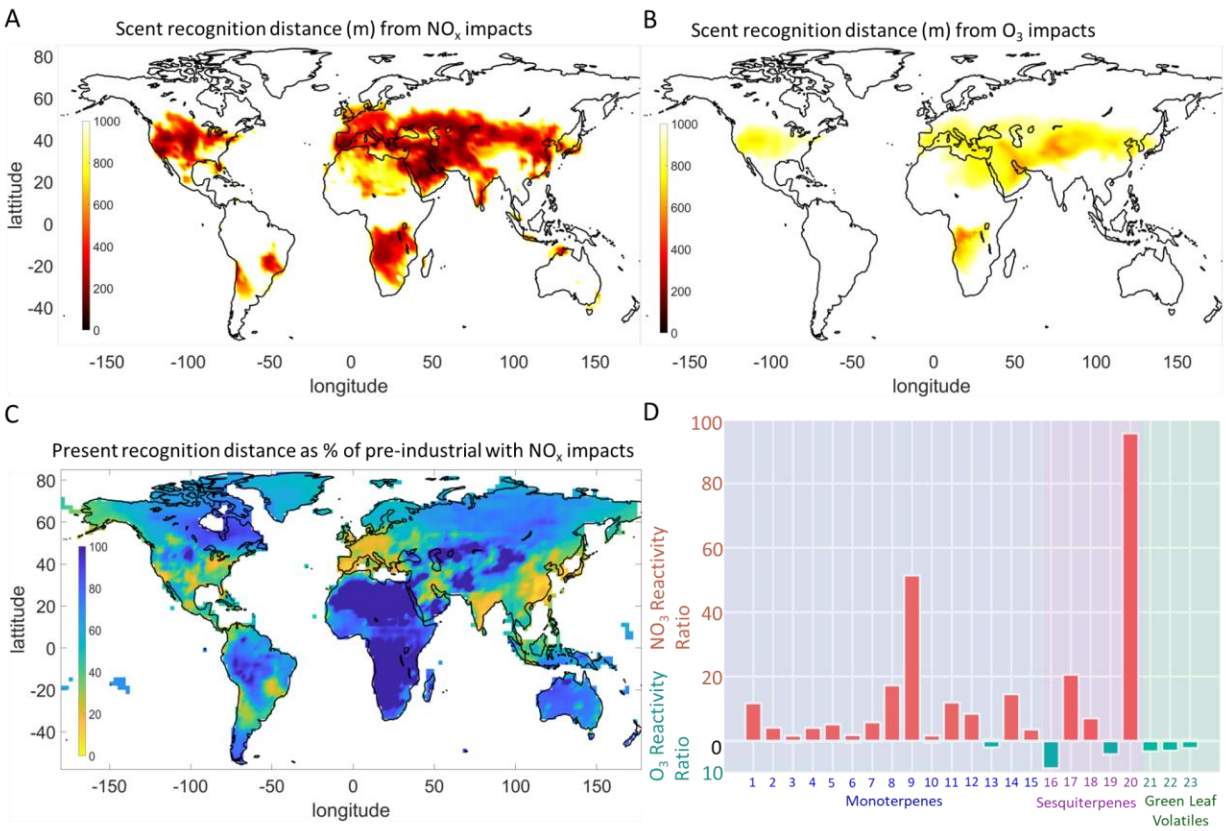

Figure 4 A: Map of floral scent recognition distance using O_3 and NO_3 degradation of the volatiles β-pinene and ocimene, with degradation thresholds of 84% and 67% respectively, and a wind speed of 1 m/s. The NO_3 and O_3 distributions were generated using GEOS-Chem standard 12.1.0 with the 2013 emissions inventory and 2013 meteorology with 2 x 2.5 degree grid and 72 vertical levels to 0.01 hPa for January 2013 to February 2014. The bottom vertical level and the average concentrations for July 2013 were used. **B**: Map of floral scent recognition distance using O_3 degradation of the volatiles β-pinene and ocimene with the same conditions as in **A**, and with data from the same GEOS-Chem model run. **C**: Map of 2013 floral scent recognition distance from **A** divided by pre-industrial floral scent recognition distance as a percentage. The pre-industrial NO_3 and O_3 distributions were generated using GEOS-Chem 13.2.1 classic with the 2013 non-anthropogenic emissions inventory and 2013 meteorology with 4 x 5 degree grid and 72 vertical levels to 0.01 hPa for January 2013 to December 2013. The bottom vertical level and the average concentrations for July 2013 were used. The output was masked using a land-ocean mask to remove the values over bodies of water. **D**: A plot of reaction rate ratios of various monoterpenes (blue), sesquiterpenes(purple) and green leaf volatiles (green) (Table S8, Figure S5 A, B) towards typical urban concentrations of NO_3 (2.6 ppt) and O_3 (37 ppb). The O_3 reactivity ratio was obtained by dividing the O_3 reaction rate by the NO_3 reaction rate. The NO_3 reactivity ratio was obtained by dividing the NO_3 reaction rate by the O_3 reaction rate. Reactivity ratios of the green leaf volatiles towards typical NO_3 and O_3 concentrations was ~1:1. Chemicals: 1 β-pinene, 2 (Z/E)- ocimene, 3 myrcene, 4 limonene, 5 α-pinene, 6 linalool, 7 2-carene, 8 3-carene, 9 camphene, 10 α-phellandrene, 11 β-phellandrene, 12 sabinene, 13 α-terpinene, 14 γ-terpinene, 15 terpinolene, 16 β-caryophyllene, 17 α-cedrene, 18 α-copaene, 19 α-humulene, 20 longifolene, 21 cis-3-hexen-1-ol, 22 cis-3-hexenylacetate, 23 trans-2-hexenal.

emissions, as well as the coupling of O_3 and NO_3 abundance to arboreal VOC emissions, on scent degradation.

To further evaluate the relative impacts of O_3 and NO_3 across different floral VOCs, the rate constants of monoterpenes, sesquiterpenes, and green leaf volatiles with NO_3 and O_3 were compiled from the literature and multiplied with the mean global terrestrial surface O_3 and NO_3 concentrations between 10 and 50 degrees north from the GEOS-Chem run of 37 ppb and 2.6 ppt respectively to give typical reactivities of each of the volatiles in s^{-1} (Table S8). These values are lower than measured values of 43 - 55 ppb O_3 (Huang et al., 2017) and 3 - 40 ppt rural NO_3, 5.8-149 ppt urban NO_3 (Khan et al., 2015). The NO_3 and O_3 rates were then plotted against each other to determine the relative reactivity of each of the chemicals towards NO_3 and O_3 under typical concentrations. The results show that most of the chemicals had significantly higher reactivity towards typical NO_3 concentrations compared to O_3, except for the sesquiterpenes α-humulene and β-caryophyllene, and the green leaf volatiles which had higher reactivity towards O_3 (Fig. 4D, Fig. S5A, S5B, Table S8).

To estimate the relative impacts of summertime O_3 and NO_3 pollution on floral scent recognition distances around different cities, the scent recognition distances and current day recognition distance as a percentage of pre-industrial distance was determined within a 2º lat x 2.5º lon area of 31 large cities around the world (Table S9). The distances were determined for January 2013 for cities in the southern hemisphere, and for July 2013 for cities in the northern hemisphere. Compared to the pre-industrial simulation, the area around almost all major cities have significant decreases in recognition distance. We found no correlation between population size, scent recognition, and present vs pre-industrial impacts (Fig. S6A-C). The data reveal several examples that shed light on other factors affecting recognition distance and present vs

pre-industrial changes. The areas around Riyadh, Los Angeles, Tehran and Madrid have the shortest recognition distances though they are neither the largest cities, nor have the highest NO_x emissions. There are also regions of Central Asia and Africa like Cairo where there are short recognition distances, but low present vs pre-industrial change. These patterns result from the fact that NO_3 and O_3 concentrations that affect floral scent reactivity do not necessarily scale linearly with emissions or population. Local atmospheric chemistry, such as the amount of O_3 relative to local NO_x emissions and vegetation emissions of reactive VOCs, geography, ecology, and meteorology affect the formation, accumulation, and transport of O_3 and NO_3.

Methods

Field site and plant-pollinator observations

The *Oenothera pallida* field site was in Grant county WA 46.913451, -119.921297. This is a relatively pristine field site based on O_3 and NO_2 measurements. At this field site, *O. pallida* plants had a patchy distribution of 1-4 plants/m^2. Pollinator activity was monitored from early June to late July in 2018 and 2019 when the flowers of *O. pallida* were in full bloom. Multiple video observations of varying lengths from 30 minutes to 14 h were made for a total of 200 hours (110 hours of nocturnal and 90 hours of daytime video recordings). The observations were conducted from 9 pm to noon when nocturnal and diurnal pollinators were active. To further prevent the potential for observer interference, video observations were made using a modified Sony Alpha NEX-5T (1080p 24 fps) mirrorless camera and two Panasonic LUMIX G DMC-GF3 (720p 30 fps) mirrorless camera that were all modified to be full spectrum by removal of their hot mirrors, and illuminated with 850nm infrared LED arrays. Cameras were deployed at a distance of 1 to 2 m away from the flowers, recording 1 to 5 plants per camera with 3 to ~70

flowers total per camera. Cameras were located between 5 m to 100 m apart. The cameras and LEDs were powered with 12V of lead-acid batteries with generic DC-DC 12V to 5V buck converter modules for pollinator observations, and by a generator (Westinghouse iGen2200) with a 100 foot extension cord and power adapters for the scent treatments. Specimens and photographs of pollinators were taken to identify the pollinators. Pollinators were captured using nets during the daytime, and captured by light trapping at night with 2x 250W self-ballasted Mercury Vapor HID Lamps (Eye Lighting, Mentor, OH, USA) on a 2 m x 2 m white nylon sheet. Insects were killed with an ethyl acetate kill jar, then pinned and dried for identification. Specimens were identified using the key: Johnson, N.F. & C. A. Triplehorn & 2005. Introduction to the Study of Insects. 7th ed. Some specimens were also identified by Evan A Sugden (University of Washington) and Terry Griswold (USDA). The pollinator videos were then manually reviewed to identify and log all recorded pollinator visits.

Simultaneously and throughout the experiments and field observations, the ozone, NO2, wind velocities, and turbulent intensities, and temperature and humidity measurements were measured at the field site (Table S1B). From midnight to 6 am, temperatures were 293.8 K +/- 1.5, with a relative humidity of 42.6% +/- 5.0 (iButtons; Maxim Integrated™, San Jose, CA, USA, #DS1923) (Fig. S1B). Measurements of wind velocities and turbulent intensities were conducted via a 3D sonic anemometer and horizontal wind speeds were typically 1.1 +/- 0.48 m/s (Table S1B). O_3 was 37.0 ppb +/- 4.1 (Fig. S 1C) NO_2 was 0.72 ppb +/- 0.28 (Fig. S 1D). These measurements match similar studies of this area (Laboratory for Atmospheric Research, 2017).

Therefore, these experiments captured the physicochemical conditions that were common in this area at this time of the year, allowing us to scale our laboratory behavioral experiments detailed below.

Pollinator limitation experiments

To determine the importance of pollination and out-crossing on *O. pallida* fruit set, a total of 258 individual flowers on plants were subject to four different experimental treatments during the June through July summer months of 2017 and 2018. For four weeks, flowers were either unbagged (n = 63 flowers) or bagged to prevent pollinator visitation (n = 44 flowers). Green organza bags (Model B07735-1; Housweety, Causeway Bay, Hong-Kong) were used to prevent pollinators from visiting the flowers. We also determined the importance of cross-pollination for *O. pallida*. For cross-pollination, pollen was removed from the anthers of several plants from 100-150m away using a brush and then transferred to the treatment flowers by gently brushing against the flowers' stigma (n = 40 plants). To examine the effects of self-pollination, anthers were removed from three flowers, and a brush was used to collect and transfer the pollen to flowers on the same plant (n = 9 plants). At the end of the field season, the number of flowers that produced fruits was recorded. Fruit sets between treatments were compared using a comparison of population proportions with Holm correction (Zar, 2010).

Plant VOCs collection and analysis, and characterization of free-radical oxidation of the floral scent

To characterize the *O. pallida* scents, headspace collections were performed during the summers of 2017, 2019, and 2020 in the Grant county WA field site (Washington, USA).

Specimens of *O. pallida* were also maintained in the greenhouse. Scents were collected during their peak flowering time and from those with unpollinated flowers. To collect the flower scent, the plant's inflorescence was enclosed in a nylon oven bag (Reynolds Kitchens, USA) that was tight around the stem. Two tygon tubes (Cole-Parmer, USA) were inserted at the base of the bag; one providing air into the bag through a charcoal filter cartridge (1 L/min.) to remove any contaminants from the pump or the surrounding air, and the other tube pulling the air out of the bag (1 L/min.) through a headspace trap composed of a borosilicate Pasteur pipette (VWR, Radnor, PA, USA) containing 100 mg of Porapak powder Q 80-100 mesh (Waters Corporation, Milford, MA, USA). This amount of Porapak was calibrated for collecting the floral headspace without bleed-through. The tubes were connected to a diaphragm pump (10D1125-101-1052, Gast, Benton Harbor, MI, USA), for the field VOCs collection connected to a battery (Power-Sonic PS-6200 Battery, M&B's Battery Company). Scent collections began at sunset and continued overnight for 12 h for initial scent analysis. The flowers were also sampled for 5 hours from midnight to 5 am to determine the nighttime scent profile, and for 5 hours from 6 am to 11 am to determine the daytime scent profile. For headspace controls, samples were taken concurrently from empty oven bags. Immediately after headspace collection, traps were eluted with 600 µL of 99% purity hexane (Sigma Aldrich, Saint-Louis, MO, USA). The samples were sealed and stored in 2 mL amber borosilicate vials (VWR, Radnor, PA) with Teflon-lined caps (VWR, Radnor, PA) on dry ice until reaching the laboratory, where they were stored at -80°C until analysis by GCMS. A total of 35 floral headspace samples were collected.

Gas Chromatography with Mass Spectrometric Detection of the O. pallida scent

To characterize the composition of the O. pallida scent, three microliters of each sample was injected into an Agilent 7890A GC and a 5975C Network Mass Selective Detector (Agilent Technologies, Palo Alto, CA, USA). A DB-5 GC column (J&W Scientific, Folsom, CA, USA; 30 m, 0.25 mm, 0.25 μm) was used, and helium was used as the carrier gas at a constant flow of 1 cc/min. For runs with the DB-5 column, the oven temperature was 45° for 4 min, followed by a heating gradient of 5°/min to 150°, followed by 15°/min to 300° which was then held isothermally for 2.5 min. The total run time was 37.5 min.

Chromatogram peaks were then manually integrated using the ChemStation software (Agilent Technologies, Santa Clara, CA, USA) and tentatively identified by the online NIST library. Using methods developed in our laboratory for identifying and quantifying volatiles in floral headspace emissions (Riffell et al., 2008b; Riffell et al., 2013; Riffell et al., 2014), the data from each sample was first run through a custom program. (https://github.com/cliffmar/GCMS_and_combine) to identify the volatiles based on their Kovats index and to remove potential contaminants and chemical synonyms for the subsequent analyses. Synthetic standards at different concentrations (0.2 ng/ml to 0.2 μg/ml) were then run to identify the peaks further and to quantify the areas for each compound; peaks are presented in terms of nanograms per hour per inflorescence (Table S3B).

Manduca sexta and Hyles lineata collection and colony conditions

Naïve *Manduca sexta* and *Hyles lineata* (Lepidoptera: Sphingidae) larvae were obtained from the moth-rearing facility of the Department of Biology of the University of Washington. The lab-reared *H. lineata* was established by collecting wild moths from the Grant county WA

field site (46.913451, -119.921297) and near Tucson AZ USA (31.720497, -110.874829) (Via Cristina Francois and Goggy Davidowitz). Larvae from both species were reared on an artificial diet (modified from Bell and Joachim, 1976) supplemented with cholesterol (5 g), wheatgerm (144 g; 14 mg carotenoids), cornmeal (140 g; 2 mg carotenoids), soy (76 g; 10 mg carotenoids), linseed oil (9 mL), and sugar (36 g) to enhance adult vision. Eclosed adults that had been reared on this diet as larvae had red eye shine when examined under white light (as did wild-caught moths), suggesting that all visible wavelengths of light except red were adsorbed by the moth photopigments. Larvae were reared under long-day light:dark (LD) regimen (LD 17:7) at 25–26 °C and 40–50% relative humidity (RH). Pupae were segregated by sex and held in a rearing room under reverse-photoperiod conditions (LD 14:10) and with a superimposed temperature cycle: LD 26:24° C. Male moths were used because the *O. pallida* odor may influence *H. lineata* and *M. sexta* female moth oviposition behavior, and thus a female preference for *O. pallida* may reflect a preference for an oviposition site rather than a nectar resource.

Electroantennogram Detection (EAD) and Gas chromatography linked with Electroantennogram Detection (GCEAD).

In separate experiments, we used gas-chromatography (GC) coupled with electro-antennographic detection (EAD) and electroantennogram detection (EAD) to identify compounds in the flower bouquet that can be detected by the hawkmoths, and examine differences between the two species in their sensitivity to the floral mixture. A total of 21 adult moths were used in the GC-EAD experiments (8 for *M. sexta*, and 13 for *H. lineata*) (Table S5), and 318 moths for EAD experiments (159 for *M. sexta*, and 159 for *H. lineata*). GC-EAD and EAD recordings provide information for how the moth periphery processes floral scent and

single components – GC-EAD is used to identify salient compounds in the floral bouquet while EAD responses to the floral mixture allowed us to determine the sensitivity of the antenna to the odor.

Adult male *M. sexta* and *H. lineata* were reared in the laboratory on an artificial diet under a long-day (17/7 hr light/dark cycle) photoperiod and prepared for experiments 2 days after emergence. For GCEAD experiments, the antenna from a single male moth was cut and connected to two glass electrodes filled with a 50% by volume mix of conductive gel (Parker Laboratories, Fairfield, NJ, USA) and *Manduca* physiological saline (4 mM NaCl, 40 mM KCl, 3 mM $CaCl_2$, 18 mM $MgCl_2$) (Kataoka et al., 1989). The mounted antennae were oriented at 90º from the main airline which was carrying medical air (Praxair, Danbury, CT, USA) and volatiles eluting from the Gas-Chromatograph to the preparation via a 200º C transfer line (EC-05; Syntech GmbH, Buchenbach, Germany).

For stimulation by the GC effluent, a 3 µL sample of collected *O. pallida* headspace volatiles was injected (splitless, 30 s) into an Agilent 7820A GC (Agilent Technologies) equipped with a flame ionization detector (FID) and aDB5 column (J&W Scientific, Folsom, CA, USA). The oven program was the same as the one used for the GC-MS analyses of the scent extracts. Effluent was split 1:1 between the FID of the GC and the moth antenna using a universal glass "Y" connector (J&W Scientific). Deactivated, fused-silica capillary tubing of the same internal diameter as the separation column carried the effluent to each detector. Effluent to the antenna passed through a heated transfer line (EC-05; Syntech GmbH, Buchenbach, Germany) set at 200° C into a 16-mm (i.d.) glass odor-delivery tube, via a small side hole, and mixed with a stream of medical air (Praxair, Danbury, CT, USA) flowing through the delivery tube to the side of the antenna at a rate of 80 ml/min.

The EAG signal was recorded by Ag-AgCl wires and electroantennogram signals were filtered and amplified (100×; 0.1-500 Hz) using an A-M 1800 amplifier (Sequim, WA, USA) connected to a personal computer via a Axon Digidata 1550B Low Noise Data Acquisition System digitizer (Molecular Devices, LLC. San Jose, CA, USA). A Hum Bug noise eliminator (Quest Scientific, Vancouver, Canada) was used to decrease electrical noise. The antennal responses to peaks eluting from the GC were measured for each antennal preparation and for each peak and moth species. Bioactive peaks were those that elicited deflections beyond the average noise floor of the baseline EAD signal, which were visually determined and tabulated.

Preparation of synthetic floral scent blend

All the synthetic chemicals used for the behavioral experiments were ordered from Sigma Aldrich (St. Louis, MO, USA)(≥98% purity) with the exception of the 2-methylbutanal oxime that was synthesized according to the methods of Damljanović et al. (2006) and ocimene (Sigma Aldrich, St. Louis, MO, USA)(≥90% purity). The ratio of syn- and anti-isomers approximated those quantified in the *O. pallida scent* (Table S3C, Table S4). For the synthesis of 2-methyl butyl aldoxime, neat 2-methyl butanal (10.0 mL) was added to solid anhydrous hydroxylamine hydrochloride (7.88 g) and solid sodium hydroxide (4.57 g) in a mortar and subsequently ground with a pestle for approximately 50 minutes. Afterward, the suspension was filtered through filter paper (Whatman 1, 90 mm diameter) yielding 2-methyl butyl aldoxime (mixture of syn [77.2%], and anti [22.8%] isomers). Purity was determined to be 86.8% by GC-MS with an Agilent 7890A GC with a 5975 MSD (Agilent Technologies, Palo Alto, CA, USA) (Table S3C). The artificial mixture was composed of a 12-component blend of odorants identified as antennal-active (via the GC-EAD experiments)(Fig. S3B, Table S3B, Table S5): The mixture was

prepared by adding each synthetic component and adjusting so that the headspace concentrations matched those found in the *O. pallida* floral headspace (as quantified through GC-MS) (Table S4). Briefly, emission rates of the artificial mixtures and single compounds were scaled to those of live flowers by their individual vapor pressures and associated partial pressures, and verified and adjusted by iterative headspace collection and quantification using the GC-MS (*sensu* Riffell et al., 2014).

EAG dose response in *Hyles lineata* and *Manduca sexta*

For EAD experiments, olfactory stimuli were delivered to the antenna by pulses of air from a constant air stream were diverted through a 1 mL syringe containing a piece of filter paper bearing the floral odor (10 µL). The floral odor was tested at different concentrations (1:100,000,000, 1:10,000,000, 1:1,000,000, 1:100,000, 1:10,000, 1:1000, 1:100, 1:33). The stimulus was pulsed by means of a solenoid-activated valve controlled by the WinEDR software (Strathclyde Electrophysiology Software, Glasgow, UK). The outlet of the stimulus syringe was positioned 2 cm from and orthogonal to the center of the antenna. Stimulus duration was 1 sec, delivered into a 16-mm (i.d.) glass odor-delivery tube, via a small side hole, and mixed with a stream of medical air (Praxair, Danbury, CT, USA) flowing through the delivery tube to the side of the antenna at a rate of 80 ml/min. Five pulses were separated by a 10 s interval per trial. The control solvent for the floral mixture was mineral oil. Antennal responses to each odor pulse were quantified in Python (Python Software Foundation. Python Language Reference, version 3.7.6) be removing noise spikes and averaging the two largest deflections in each five pulse trial.

Clean air source, N_2O_5 generator for generating NO_3, and flowtube

Filtered and dried air was supplied by a compressor (California Air Tools 1P1060SP) through three Drierite 27068 L68GP Gas Purifiers (W.A. Hammond Drierite Company LTD) filled with silica gel (WISESORB, orange-green indicating, 2-4 mm bead size), activated charcoal (Sigma-Aldrich, 4-8 mesh, Lot # SLBH5329V), Drierite (W.A. Hammond Drierite Company LTD, # 24005) and molecular sieves (WISESORB, 13x, 1.5-2.5 mm bead size). In the N_2O_5 generator, O_3 was generated by a 77 sccm flow of dry, filtered air through a fused silica ozone lamp [Jelight Inc., Irvine, CA, USA, model 81-3306-7, 30 mW/cm^2 at 254 nm and 1.3 mW/cm^2 at 185 nm] in a steel tube, which was mixed with a 10 sccm flow of 19 ppm nitrogen dioxide in N_2 (Scott-Marrin Inc., Riverside, CA, USA), allowing them to react in a Teflon tube (2.55 cm diameter x 45.7 cm long) for (162 seconds). This mixture leads to the formation of NO_3 in thermal equilibrium with dinitrogen pentoxide, N_2O_5 and NO_2 (Fig. S7A) by chemical modeling (Equation S1) using Matlab (MATLAB version 2020b, The MathWorks, Inc., Natick, MA, USA). The apparatus has been used as a reproducible source of N_2O_5 and NO_3 for instrument calibration in previous work (Lee et al., 2014, Lopez-Hilfiker et al., 2016a). The flowtube consisted of a 7.6 cm internal diameter borosilicate glass tube with a length of 86 cm and was wrapped in aluminum foil to prevent light from degrading the NO_3.

Characterization of free-radical oxidation of O. pallida scent and scent constituents

A series of experiments investigating the oxidative effects of NO_3 and O_3 were conducted on the floral odor blend under dry (RH < 1 %) and dark conditions with (NO_3 supplied from the N_2O_5 generator. Before the experiment, the flowtube was flushed overnight with 1 SLM 99.9999% UHP nitrogen (Praxair Inc.) to minimize any remaining contamination. There were

three stages of the experiment, and throughout each stage, floral scent or scent constituents were continuously injected into the reaction chamber. In the first stage, 23 sccm of headspace from a 500 mL culture bottle containing 200 mL of *O. pallida* floral odor blend (Table S4) was added to 3177 sccm flow of clean air, which simulates floral scent emissions from a single *O. pallida* flower. Thereafter, O_3 at 120 ppbv (stage II) measured with a Model 202 Ozone Monitor (2B Technologies, Boulder, CO, USA) was also injected into the reaction chamber to allow the degradation of the scent and scent constituents while allowing the reactions to reach steady-state conditions over several minutes. Stage III was initiated by the injection of NO_x from the N_2O_5 generator into the reaction chamber. The flow of clean, filtered air was adjusted to maintain a 3.2 SLM flow rate through the flowtube at all times. Chemical modeling (Equation S1) using Matlab (MATLAB version 2020b, The MathWorks, Inc., Natick, MA, USA) showed that the N_2O_5 from the N_2O_5 generator dissociates over the 73s flowtube residence time to allow NO_3 oxidation chemistry to occur (Figure S7B, Equation S1).

A high-resolution time-of-flight chemical ionization mass spectrometer (HR-ToF-CIMS, Aerodyne Research Inc., hereafter CIMS) (TOFWERK AG, Thun, Switzerland) was used to continuously measure the gas-phase products from floral odor oxidation in the flowtube. Two different ionization modes were used to measure the oxidation of the *O. pallida* odor blend by O_3 and NO_3. Benzene cations were used with a low-pressure ion-molecule reaction chamber (IMR) setup as described in Lee et al., 2014 using a deuterated benzene 99.95% (99.6% atom D)(Cambridge Isotope Labs, Teddington, Middlesex, UK) permeation tube instead of a methyl iodide permeation tube in the ion source. In that setup, ambient air was drawn through a critical orifice at 2.0 standard liters per minute (SLM) into the IMR, which is held at 90 mbar by means of a IDP3 scroll pump (Agilent Technologies, Santa Clara, CA, USA). A VOCUS PTR ion

source and ion-molecule reactor (Krechmer et al., 2018) was also used separately to measure the oxidation of individual odor blend chemicals by O_3 and NO_3. The mass spectra were analyzed using Tofware V3.0.3 mass spectral analysis software (TOFWERK AG, Thun, Switzerland).

Behavioral wind tunnel experiments

In the wind tunnel experiments testing the attractiveness and visitation to flowers emitting the natural and degraded odors, a total of 234 moths were tested – 138 *M. sexta* and 96 *H. lineata*. A synthetic mixture composed of 12 bioactive VOCs that mimics the *O. pallida* scent from one flower (2-methylbutanal oxime (54.4% syn ee), benzaldehyde, β-pinene, 5-Hepten-2-one, 6-methyl-, (Z)-3-Hexen-1-ol acetate, 1,8-cineole, (Z)-β-ocimene, nonanal, methyl nicotinate, methyl salicylate, decanal, indole) (Table S4) was used as the odor stimulus along with a clean air (no odor) control. 23 sccm of headspace from a 500 mL culture bottle containing 200 mL of *O. pallida* floral odor blend (Table S4) was added to 3177 sccm flow of dried, filtered air, which simulates floral scent emissions from a single *O. pallida* flower. This was then passed through the flowtube (7.6 cm diameter x 86 cm length) before being delivered through a 6.4 mm OD, 4.8 mm ID Teflon tube (Fluorostore, Parsippany, NJ, USA) through the center of a filter paper cone (Whatman 1, 80 mm diameter) which was formed into a cone by cutting a quadrant out from the filter paper disc and taping the cut edges together. The oxidized scent treatments had an added flow containing O_3 and/or NO_2 to generate nitrate radicals through the N_2O_5 generator. *H. lineata* was behaviorally tested with 1 floral equivalent of *O. pallida* floral odor blend, 1 floral equivalent of *O. pallida* floral odor blend oxidized with O_3 and NO_3 and a clean air control. *M. sexta* was behaviorally tested with 1 floral equivalent of *O. pallida* floral odor blend, 1 floral equivalent of floral odor blend oxidized with O_3 and NO_3, which

resulted in no behavioral difference, so further treatments with 100x diluted floral odor blend were tested. These treatments consisted of 1/100 floral equivalent of floral odor blend, 1/100 floral equivalent of floral odor blend oxidized with NO_2, 1/100 floral equivalent of floral odor blend oxidized with O_3, 1/100 floral equivalent of floral odor blend oxidized with O_3 and NO_3, 1/100 floral equivalent of simulated O_3 and NO_3 oxidized floral odor blend with 67% less ocimene and 84% less β-pinene, and a clean air control. For each olfactory stimulus, 11-42 moths were tested (Table S7A).

A Plexiglas wind tunnel (L x W x H = 2.5 x 1 x 1 m) was used to create a highly controlled wind flow environment for examining flight behavior in response to *O. pallida* floral odor and degraded plumes. The wind-tunnel conditions were physicochemically scaled to match the odor emission rate equivalent to that of the *O. pallida* flower emissions, and the field site conditions. Longitudinal (u) wind speeds in experiments were 50 cm/s, which is often encountered in the field under stable conditions at night (Matthews & Sponberg, 2018) (Table S1B) and which we have used in prior experiments (Riffell et al., 2014). At the beginning of scotophase, naïve, adult male moths (either *M. sexta*, or *H. lineata*) were placed individually 2 m downwind from the odor source. Each moth was allowed to fly freely inside the wind tunnel for 3 min, during which its behavior was recorded. Moth behaviors to the odor stimuli were scored based on wing fanning (typical behavior just prior to flight), upwind flight (moth comes within 0.75 m of odor source), close hover (moth hovered within 10 cm of odor source), source contact, and proboscis extension into the flower corolla (hereafter termed "feeding"). The proportion of feeding visits for the floral odor blend and O_3 and NO_3 oxidation treatment was then compared using a test of population proportions (Zar, 2010).

Field pollinator visitation experiments testing the impacts of oxidized floral scents

To examine the impact of degradation of floral scents on pollinator visitation, we conducted plant-pollinator visitation experiments in the field (Grant county WA 46.913451, -119.921297) using approaches similar to the ones described above in our wind tunnel and pollinator observation experiments. Observation of pollinator visitation to flowers started about 2 hours after sunset when the *O. pallida* flowers opened and stopped at about 6 am at twilight before daytime pollinators became active. A generator (Westinghouse iGen2200) was placed 30 m away from the setup and powered by an air compressor (California Air Tools 1P1060SP) which supplied the clean air to all treatments. Three Drierite 27068 L68GP Gas Purifiers (W.A. Hammond Drierite Company LTD) filled with silica gel (WISESORB, orange-green indicating, 2-4 mm bead size), activated charcoal (Sigma-Aldrich, 4-8 mesh, Lot # SLBH5329V), Drierite (W.A. Hammond Drierite Company LTD, # 24005) and molecular sieves (WISESORB, 13x, 1.5-2.5 mm bead size) were used to clean and dry the air from the compressor. 1/4" polyethylene tubing (Hudson Extrusions INC, NSF 51/61 PE1100 LLDPE) was used to relay the air to Alicat mass flow controllers (Alicat Scientific Inc, Tucson, AZ) which controlled air flow to the odor mixture treatments, and Gilmont flow controllers which controlled air flow to the control and real floral scent treatments.

Similar to the experiments in the laboratory wind tunnel, the floral odors were released at 23 sccm of airflow from 500 mL Fisher Scientific culture bottles containing 200 mL of 1% v/v floral odor in mineral oil (Table S4). The odor concentration and amount within the bottle were quantified by GCMS to equal the emissions of one *O. pallida* flower. The oxidized scent treatment had an added flow of NO_3 which were generated in the form of N_2O_5 from the N_2O_5 generator. The air flow was then diluted to a total flow of 3.2 SLM with clean air. The scent flow

then passed through a borosilicate glass flowtube (7.6 cm internal diameter x 86 cm long) for a total reaction time of 73 seconds before passing to the artificial flowers. N_2O_5 readily dissociates to form NO_3, which react with scent chemicals in the flowtube (Fig. S7B) (Equation S1). The different controls and floral odor treatments were released from artificial flowers (Whatman 1, 80 mm diameter; cut, and arranged to form a cone), the center of which emitted the odor through a 4.8 mm internal diameter Teflon tube.

Five different treatments – each situated approximately 2 m from one another – were simultaneously conducted each night: (1) A real flower treatment with a camera recording pollinator visits to a plant with 1 or 2 flowers; (2) A clean air control with 3.2 SLM of clean air flowing to a paper flower; (3) A real floral scent treatment with 3.2 SLM of air from a 500 mL three-necked round-bottomed flask containing a single *O. pallida* flower (still attached to the plant), delivered to a paper flower; (4) The synthetic *O. pallida* floral odor mixture delivered in 3.2 SLM of clean air flow through a glass flowtube to a paper flower; (5) An oxidized floral odor treatment consisting of the output of the N_2O_5 generator and one floral equivalent of synthetic *O. pallida* floral odor blend delivered in 3.2 SLM clean air through a glass flowtube to a paper flower. Six cameras (5 SEREE camcorders, Panasonic LUMIX G DMC-GF3) were deployed for scent treatments. Four cameras recording from four scent treatments (scent blend, O_3 and NO_3 oxidized scent blend, real floral scent, and clean air control), one camera recording a single *O. pallida* plant with 5 to 22 flowers, and one camera recording the entire setup from a distance of 5 m. The cameras were positioned approximately 1 m from the flowers or scent sources.

A total of 285 h of pollinator visitation data was recorded and analyzed manually (approximately 47.5 h observation per treatment) (Table S7B). As in our pollinator observation and plant fitness experiments, hawkmoths (*H. lineata*, *Manduca* spp.) were readily identifiable

based on their markings and flight patterns. For the real flower treatment, hawkmoth visits to individual flowers on the plants were considered and used to compute the mean number of visits to each flower per hour for all observations. This was then multiplied by the number of hours of observation to give the mean visits to a single flower over the hours of observation (Table S7C). Data across all nights were pooled for analysis. The number of hawkmoth visits to the different treatments was analyzed in R (R version 4.0.3, The R Foundation for Statistical Computing) using a generalized linear model for Poisson data with a log link function. P-values of the coefficients were considered in comparisons between treatments (Table S7D).

Global models of ozone and nitrate radicals and effects on pollinator detection of flowers

The GEOS-Chem chemical transport model (Bey et al., 2001) was used for simulations driven by assimilated MERRA-2 (Modern-Era Retrospective analysis for Research and Applications, Version 2) meteorological fields (Gelaro et al., 2017). The spatial resolution of grids were 2◦ × 2.5◦ (lat × long) with 47 vertical levels, and the simulation period was from March 2012 to June 2014, with the first year as a spin-up period to allow for the accumulation of intermediate chemical reservoir species. A reference simulation was conducted based on the public version 12.1.0 of GEOS-Chem (http://wiki.geos-chem. org/GEOS-Chem_12#12.1.0, last access: July 2019). The HOx –NOx –VOC–O3–BrOx tropospheric chemistry chemical mechanism in the reference simulation is described in Mao et al. (2010, 2013) with recent updates for biogenic volatile organic compound (VOC) chemistry (Fisher et al., 2016; Travis et al., 2016). The Model of Emissions of Gasses and Aerosols from Nature v2.1 (MEGAN) (Guenther et al., 2012) was used to derive biogenic emissions, and the Global Fire Emissions Database (GFED4) was used for open fire emissions. For anthropogenic emissions of various

gaseous and aerosol species, the CEDS (Community Emission Data System) inventory was the basis but combined with local inventories in Asia, the USA, Canada, Mexico, Europe, and Africa. More details about the simulations are described in Xu et al., 2022.

For the preindustrial GEOS-Chem model run, we used the GEOS-Chem chemical transport model version 13.2.1 (Bey et al., 2001) driven by assimilated meteorology from MERRA-2 (Modern-Era Retrospective analysis for Research and Applications, Version 2) from the year 2013 at a horizontal resolution of 4°x 5° and 72 vertical levels up to 0.01 hPa. GEOS-Chem contains detailed HO_x-NO_x-VOC-ozone-halogen-aerosol chemistry (Wang et al., 2021) including isoprene chemistry from Bates and Jacob (2019) and reactive uptake of NO_2, NO_3, and N_2O_5 by aerosols from Holmes et al. (2019 and McDuffie et al. (2018). Global anthropogenic emissions of pollutants including VOCs, NO_x, and various aerosol species are from the Community Emissions Data System (CEDS) v2 inventory from McDuffie et al. (2020). Biogenic VOC emissions are from the Model of Emissions of Gasses and Aerosols from Nature v2.1 (MEGAN) (Guenther et al., 2012; Hu et al., 2015) and biogenic soil NO_x emissions are from Hudman et al. (2012). Open fire emissions are from Global Fire Emissions Database (GFED4.1). Dry deposition for aerosols and gasses is based on a resistance-in-series scheme described in Wesely (1989). The wet deposition scheme is described in Luo et al. (2020) for water-soluble aerosols and in Amos et al. (2012) for gasses. To simulate a preindustrial atmosphere, all anthropogenic emissions are turned off (Zhai et al., 2021). The preindustrial simulation had 12 months of spin-up to equilibrate the model to preindustrial conditions.

GEOS-Chem code availability:

GEOS-Chem version 12.1.0 code is publicly available at http://wiki.geos-chem.org/GEOS-Chem_12#12.1.0 (https://doi.org/10.5281/zenodo.1553349, International GEOS-Chem User Community, 2018).

GEOS-Chem version 13.2.1 code is publicly available at https://doi.org/10.5281/zenodo.5500717.

The bottom vertical layers of the model output were used in computing the pollinator impacts maps. The data was processed and the maps plotted using MATLAB R2020b. Data from January 2013 was used to investigate the pollinator impacts in the summer in the southern hemisphere, and data from July 2013 was used to investigate the pollinator impacts in the summer in the northern hemisphere.

For the pre-industrial comparisons map, values over the oceans were masked by creating a mask using a modified version of the global-land-mask 1.0.0 package by toddkarin in Python, using the 'Natural Earth' map database. The land/water values in each grid cell were summed, and if there were any land values in the grid cell, the grid cell was classified as a land grid cell. Antarctica was also excluded from consideration by masking all grid cells below -56 degrees in latitude.

Mean O_3 and NO_3 values over the northern latitudes were calculated by averaging all values over land between 10 and 50 degrees latitude in the current day July 2013 GEOS-Chem model simulation.

A plot of reaction rate ratios of various monoterpenes, sesquiterpenes and green leaf volatiles (IUPAC-AERIS)(Table S8, Figure S5 A, B) towards mean northern latitude concentrations of NO_3 (2.6 ppt) and O_3 (37 ppb). The O_3 reactivity ratio was obtained by dividing the O_3 reaction rate by the NO_3 reaction rate. The NO_3 reactivity ratio was obtained by dividing the NO_3 reaction rate by the O_3 reaction rate.

Discussion

Our results demonstrate that atmospheric O_3 and NO_3 oxidation impacts nocturnal pollinator visitations in the field by changing the floral scent chemical composition, thereby reducing scent recognition distances. Different components of the floral scent are differentially degraded depending on the rates of reaction of the individual components with O_3 and NO_3, and the local concentrations of those oxidants. Local atmospheric chemistry, geography, ecology, and meteorology affect the formation, accumulation, and transport of O_3 and NO_3, and the complex interaction of these factors control the local impacts of atmospheric oxidation on floral scent recognition distance. Of the floral scent compounds analyzed, the monoterpenes were the most susceptible to O_3 and NO_3 degradation and their degradation was shown to be responsible for the reduction in hawkmoth visits in our plant-pollinator system. Given that other studies (Girling et al., 2013; Farre Armengol et al., 2015; Farre-Armengol et al., 2020; Knudsen et al., 2006) have established that monoterpenes are ubiquitous floral volatiles that are important for scent recognition in other plant-pollinator systems, our results are likely to be generalizable to other systems which use monoterpenes as key volatiles for scent recognition. While other classes of volatiles like sesquiterpenes, green leaf volatiles, and aromatics have different reactivity profiles, our analytical framework can be used to estimate the impacts of O_3 and NO_3 on scent

recognition distances in other systems if the relevant volatiles and rate constants in those systems can be determined.

We used the models to estimate scent recognition distances around major cities at present, and compared to the pre-industrial. Although the relatively coarse grid size of 2^o lat x 2.5^o lon does not resolve variation in O_3 and NO_3 concentrations around the cities, the mean values for the grid approximate what might be experienced in the regions surrounding the cities where the impacts of reduced scent recognition will have a greater impact on agriculture and ecosystems than within the cities. Comparison of present-day to pre-industrial scent recognition distances reveal that scent recognition distances around major cities have been greatly reduced. Even relatively uninhabited areas such as Alaska and Greenland have had significant reductions in scent recognition distance due to long-range transport of air pollutants. Other areas in Central Asia and Africa with short recognition distances show little change from pre-industrial times, suggesting that natural processes in some areas result in O_3 and NO_3 levels that can significantly affect floral scent recognition, though there are significant uncertainties in the emissions budgets in these remote areas. Another factor that can impact scent recognition distances is climate change and the associated changes in temperature and winds. Unfortunately, these factors are not accounted for in our pre-industrial simulations since we used present-day meteorology in our pre-industrial runs. While it may not be possible to determine pre-industrial global temperature and wind distributions with much certainty, even local temperature changes of 10 K will only result in changes in scent recognition distance by ~3% of the listed values, which will not change the trends or conclusions that we present. Local surface winds are likely to be heavily influenced by land use changes which affect the surface roughness, thus impacting turbulent dispersion of scent.

The importance of monoterpenes in floral scent recognition begs the question of why pollinators in many systems continue to rely on monoterpenes for scent recognition despite their historical susceptibility to atmospheric degradation, and the presence of many other floral volatiles which are more resistant to degradation. Perhaps monoterpenes represent a relatively ephemeral and thus salient cue about the proximity of floral resources, which will hopefully be investigated by chemical ecologists in the future. Finally, other studies have shown that atmospheric ozone can impact scent perception by pollinators (Dotteryl et al., 2016; Vanderplanck et al., 2021; Demares et al., 2022), and that the products of volatile oxidation can also impact scent recognition (Dubuisson et al.; 2022, Mofikoya et al., 2020). These factors will exacerbate the impacts from reduced scent transmission that we have investigated.

Supplemental

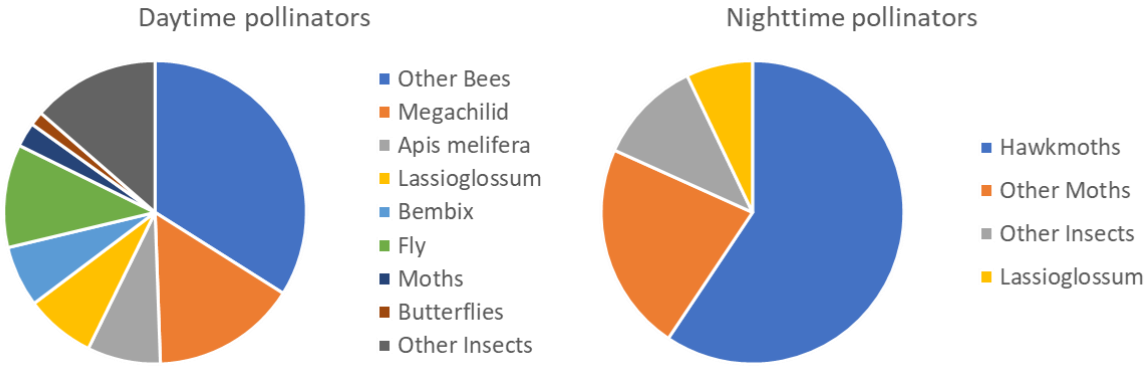

Figure S1A: Proportions of visits from different pollinator groups to *Oenothera pallida* flowers during the day and night.

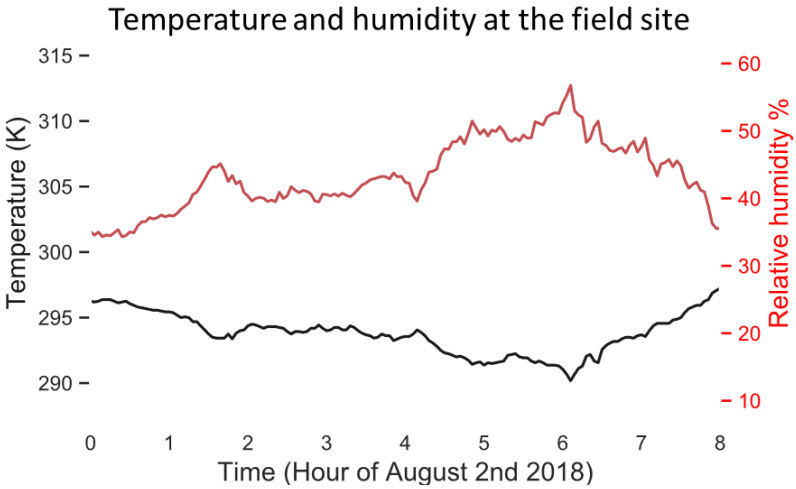

Figure S1B: Temperature and humidity at the field site recorded using Hygrochron iButtons (Maxim technologies).

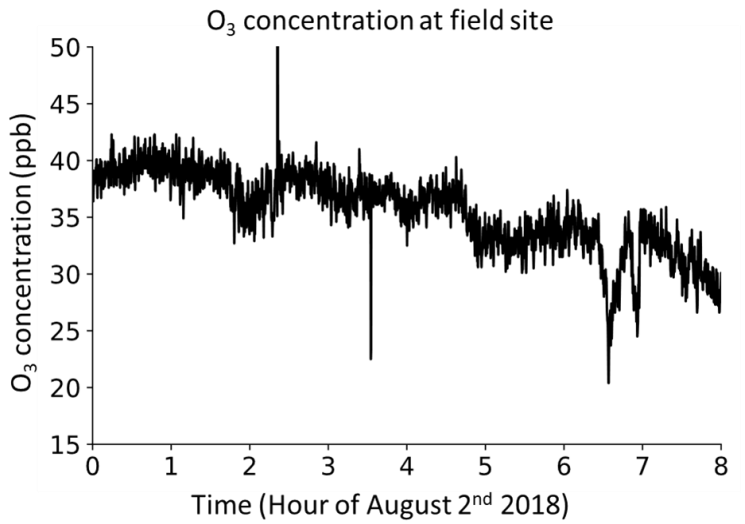

Figure S1C: Ozone concentration at the field site measured using a 2b Tech Model 202 ozone monitor.

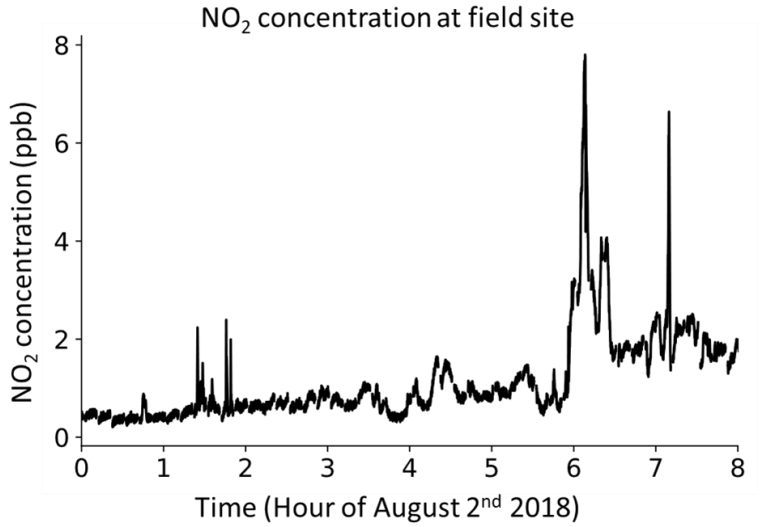

Figure S1D: Nitrogen dioxide concentration at the field site measured using a CAPs NO_2 monitor from Aerodyne.

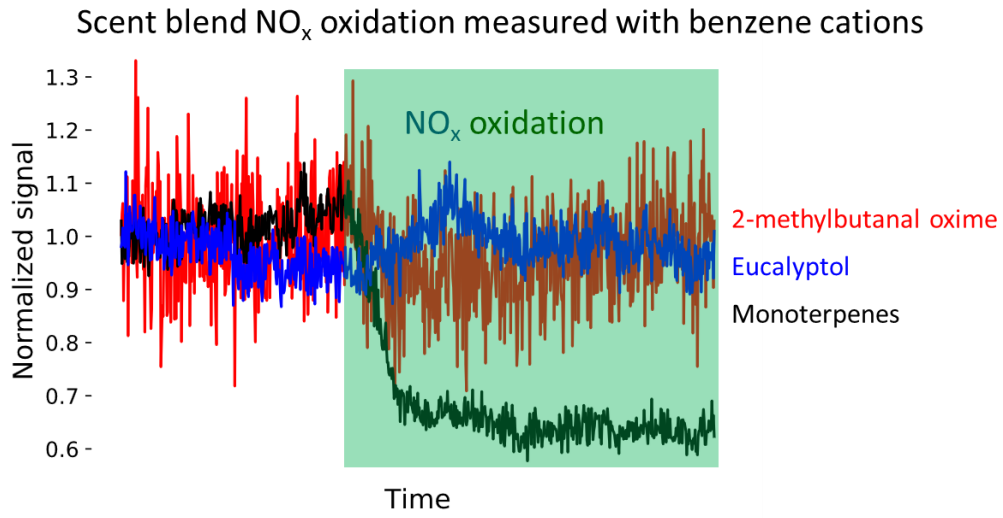

Figure S2: *Oenothera pallida* floral odor blend was oxidized in a flowtube with O_3 and NO_3 from the N_2O_5 generator and measured using the ToF CIMS (TOFWERK AG, Thun, Switzerland) with benzene cation chemical ionization mode. A drop in monoterpene concentrations was observed, while other compounds like 2-methylbutanal oxime and eucalyptol showed no change in concentrations. The oxidation of each compound in the scent blend was then analyzed individually to enable differentiation of the monoterpenes.

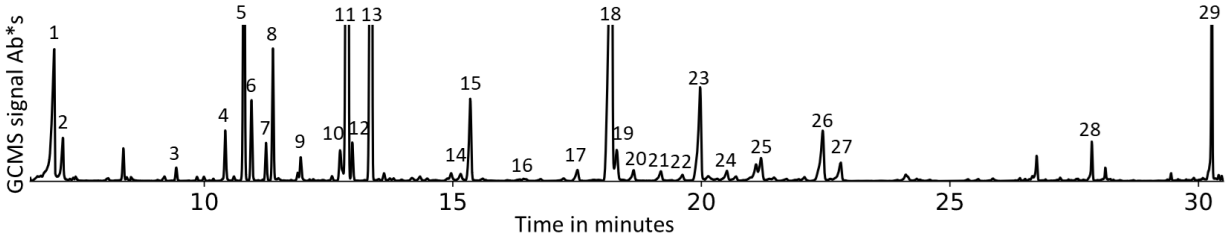

Figure S3A: Annotated GCMS spectrum of field Oenothera pallida scent sample. Peaklist in

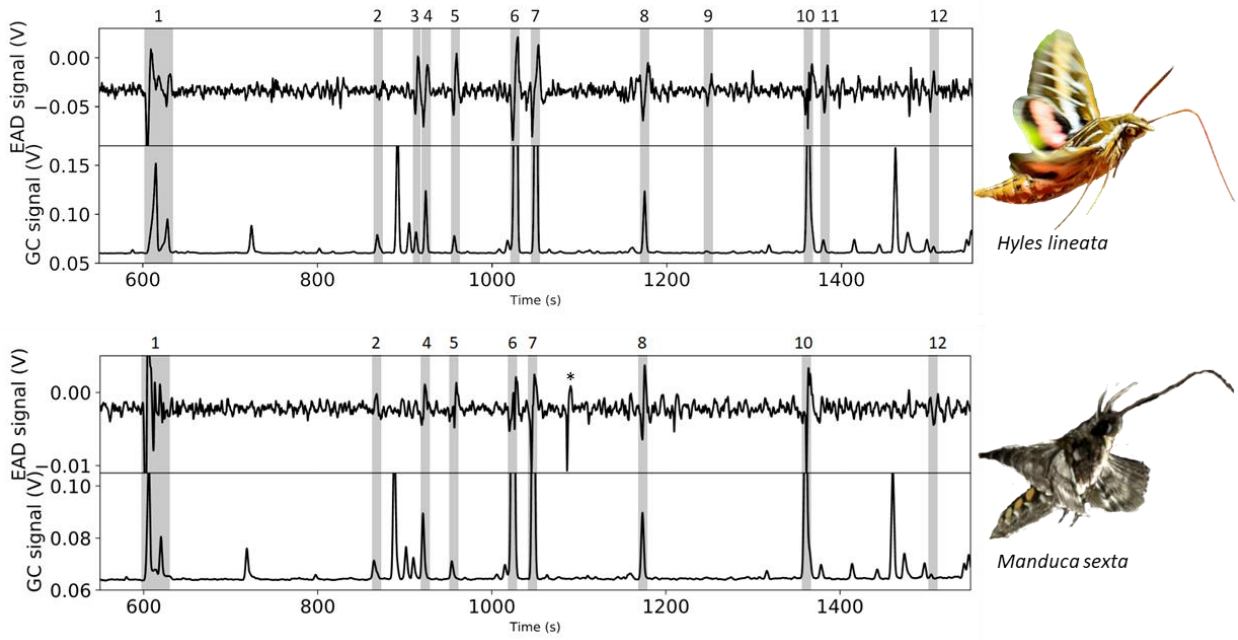

Figure S3B: Annotated GC-EAD spectra of *Hyles lineata* and *Manduca sexta* to *Oenothera pallida* scent sample. * indicates a response that was not reproducible.
Peaklist: 1. 2-methylbutanal oxime syn- and anti- isomers, 2. Benzaldehyde, 3. B-pinene, 4. Sulcatone (6-methyl-5-hepten-2-one), 5. 3-Hexen-1-ol acetate, 6. Eucalyptol (1,8-cineole), 7. (Z)- ocimene, 8. Nonanal, 9. Methyl nicotinate, 10. Methyl salicylate, 11. Decanal, 12. Indole

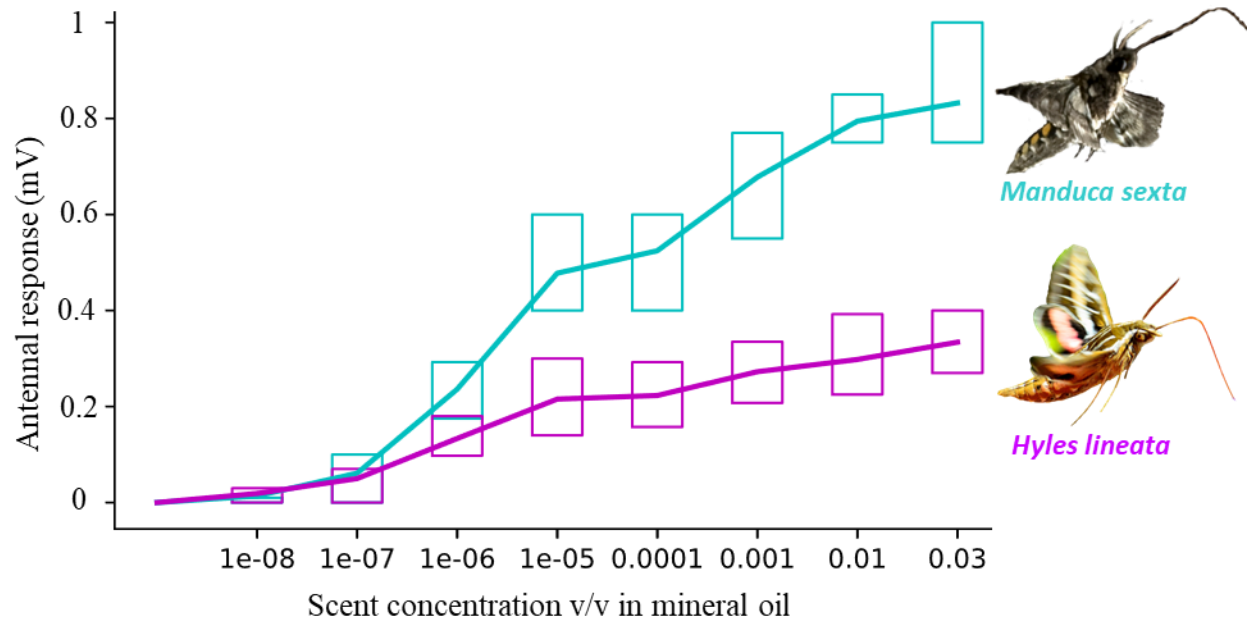

Figure S4A: Dose response curves of male *Hyles lineata* (in magenta) and *Manduca sexta* (in teal) antennae to night scent blend.

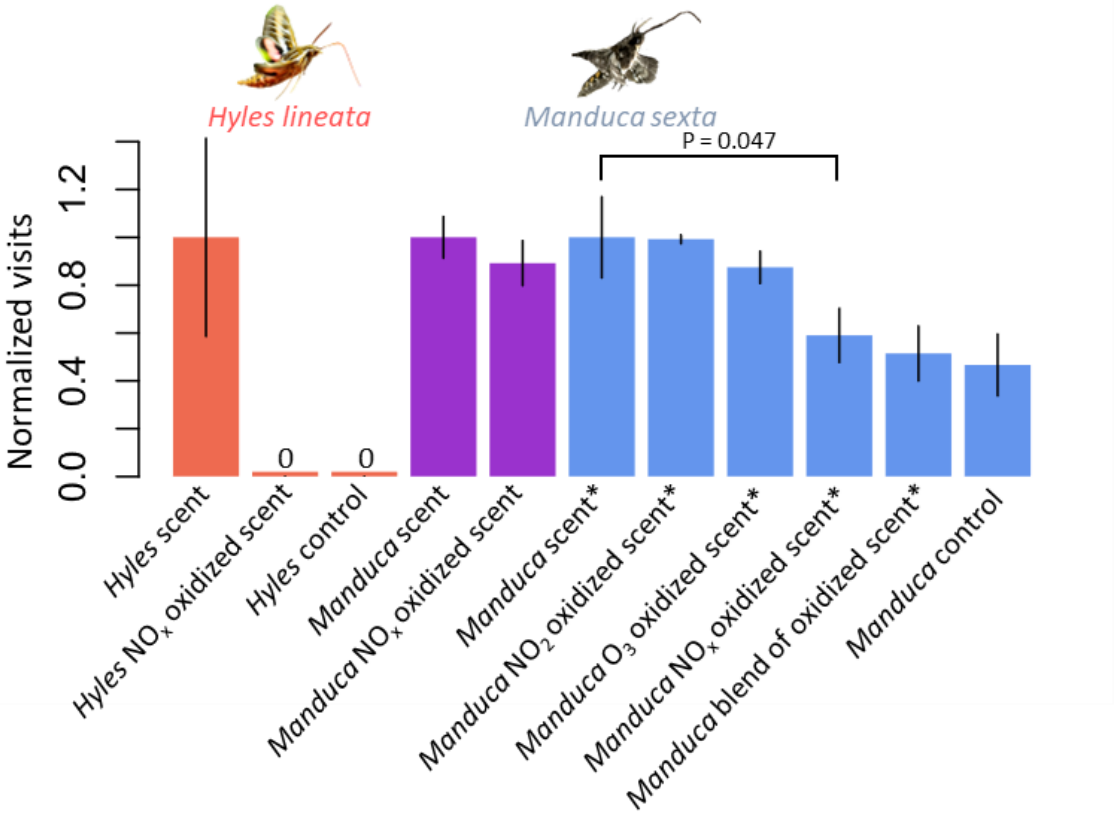

Figure S4B: Wind tunnel behavioral results for *Hyles lineata* (coral) and *Manduca sexta* (purple and blue) at 0.5 m/s laminar airflow. Individual naive male moths were released 1.5m directly downwind of the odor source, and the proportion of moths that attempted feeding from the source was recorded. The scent blend presented the same emission rate of the component chemicals as a single flower of *Oenothera pallida*. Blue bars and * indicate treatments done using 100x diluted scent blend. The visitation proportions for each set of treatments was normalized to the proportion of visits to the scent treatment. Error bars indicate standard error. O_3 and NO_3 oxidation conditions are equilibrium N_2O_5 from 120 ppb O_3 and 60 ppb NO_2 at room temperature with 73s reaction time in a glass flowtube. O_3 and NO_2 oxidation conditions include just the O_3 or NO_2 component of the NO_3 treatment. Controls were done with dry, filtered air. Another scent treatment of 'blend of oxidized scent' was performed with a scent blend containing 84% less β-pinene and 67% less ocimene than the original scent blend to simulate oxidation by O_3 and NO_3.

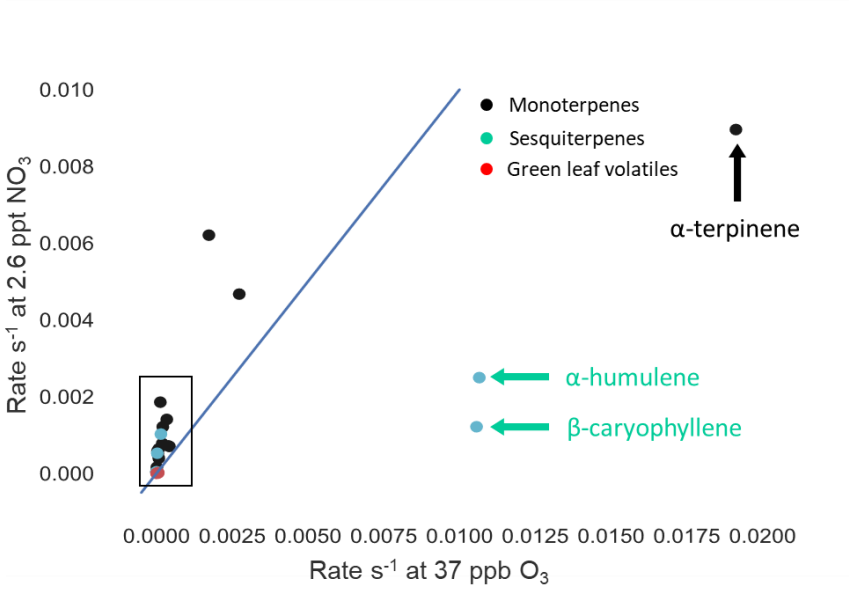

Figure S5A: Rate constants of reactions (Table S8) of various floral volatiles with ozone and nitrate radicals and reaction rates with typical northern hemisphere terrestrial O_3 (37 ppb) and NO_3 (2.6 ppt) concentrations. Monoterpenes are depicted by black points, sesquiterpenes by green points, and green leaf volatiles by red points.

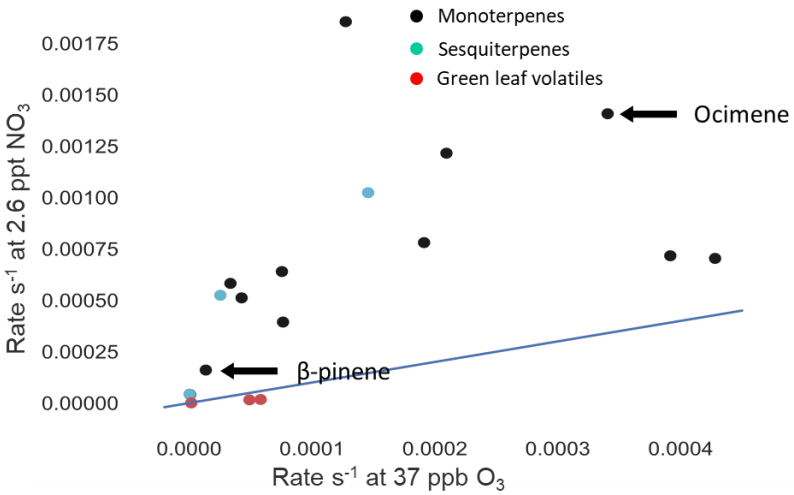

Figure S5B: Rate constants of reactions (Table S8) of various floral volatiles with ozone and nitrate radicals and reaction rates with typical northern hemisphere terrestrial O_3 (37 ppb) and NO_3 (2.6 ppt) concentrations. Monoterpenes are depicted by black points, sesquiterpenes by green points, and green leaf volatiles by red points. The outliers α-phellandrene, terpinolene, α-terpinene, α-humulene, and β-caryophyllene were excluded from this plot to visualize the points from other chemicals.

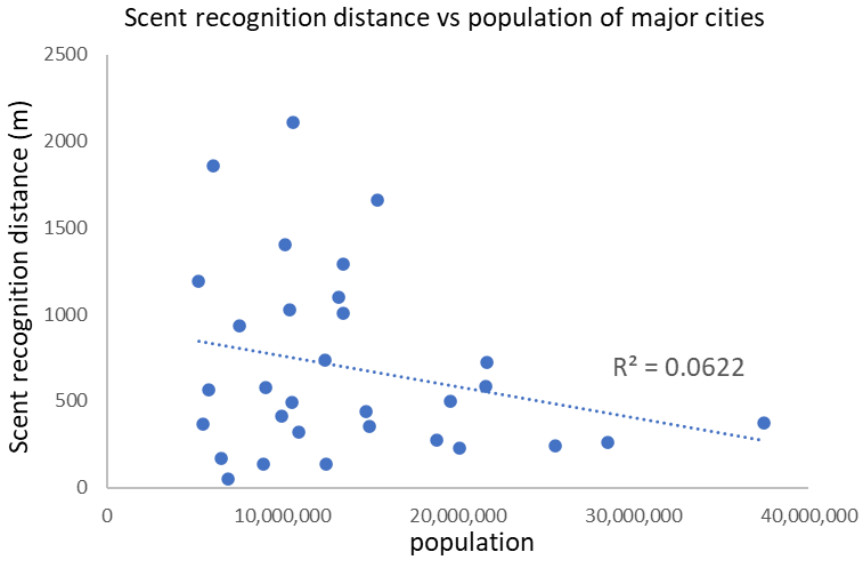

Figure S6A: Plot of summertime scent recognition distance of *Oenothera pallida* floral scent under local O_3 and NO_3 oxidation conditions in major cities by population.

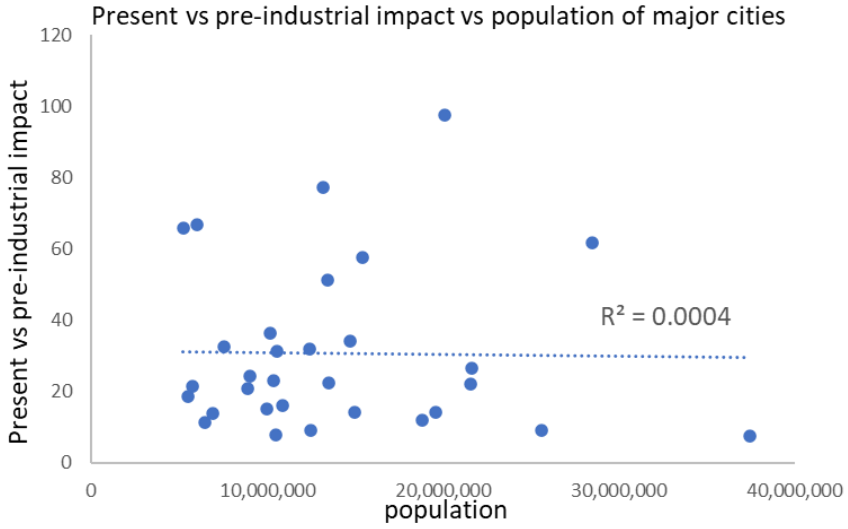

Figure S6B: Plot of summertime present vs pre-industrial impact of *Oenothera pallida* floral scent transmission under local O_3 and NO_3 oxidation conditions in major cities by population.

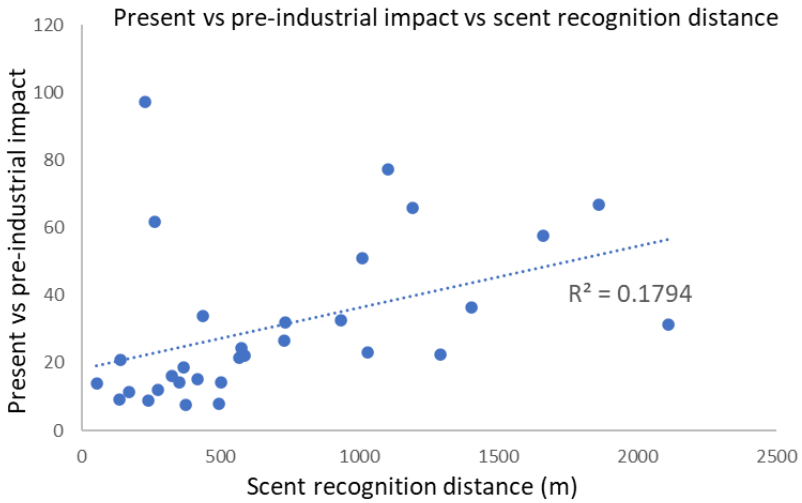

Figure S6C: Plot of summertime present vs pre-industrial impact of *Oenothera pallida* floral scent transmission vs scent recognition distance under local O_3 and NO_3 oxidation conditions in major cities.

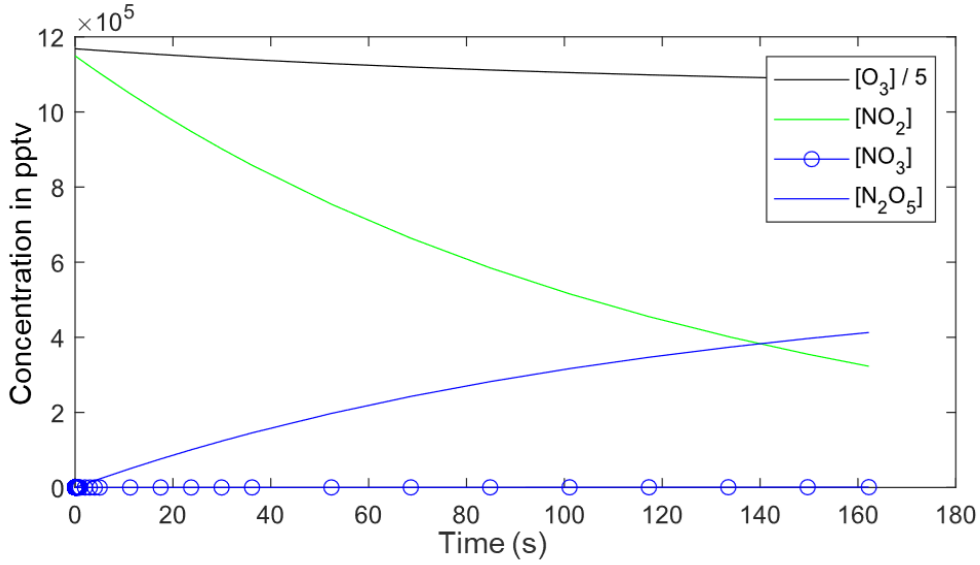

Figure S7A: Plot of modeled NO_x concentrations within the reaction chamber of the N_2O_5 generator. Residence time in the reaction chamber was 162s. O_3 concentration divided by 5 to make it visible in the plot area. Concentrations were simulated using Matlab (MATLAB version 2020b, The MathWorks, Inc., Natick, MA, USA) and Equation S1.

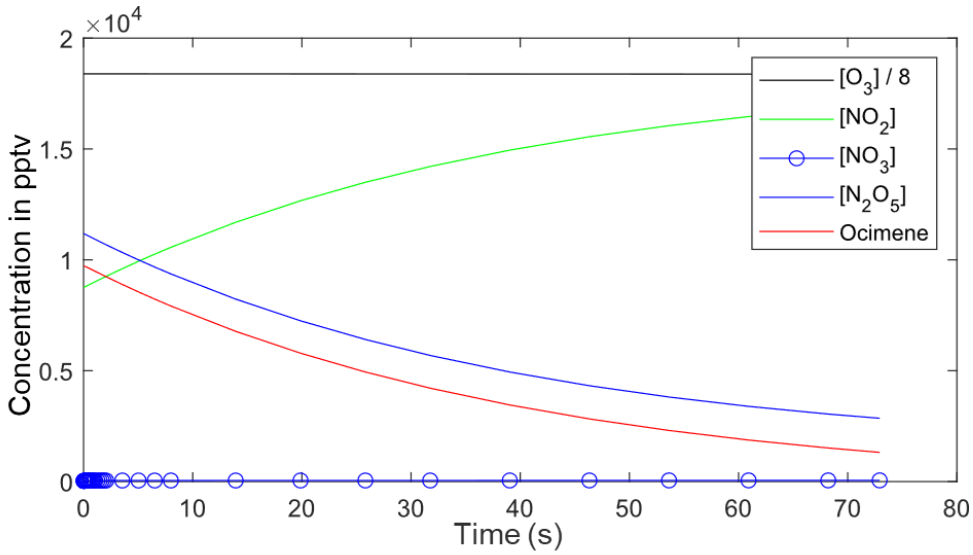

Figure S7B: Plot of modeled NO_x and ocimene concentrations within the flowtube. Residence time on the flowtube was 73s. O_3 concentration divided by 8 to make it visible in the plot area. Concentrations were simulated using Matlab (MATLAB version 2020b, The MathWorks, Inc., Natick, MA, USA) and Equation S1.

Table S1A: Table of pollinator visits from 110 nocturnal and 90 diurnal hours of video recording of 1-5 *Oenothera pallida* plants in the field with 5-70 flowers total.

Identities of floral visitors	Day	night	Total
Lepidoptera			
Sphingidae			
Hyles lineata	6	114	120
Manduca sp.		3	3
Papilionoidea			
Pieridae	8		8
Microlepidoptera		54	54
Other Moths	8	44	52
Hymenoptera			
Megachilidae (Megachile montivaga, Megachile umatillensis, Megachile rotundata, Coelioxys mesae, others)	83		83
Apoidea			
Halictidae			
Halictinae			
Lassioglossum			
Evylaeus sp.	40	14	54
Andrenidae			
Andrena			
Onagrandrena raveni	12		12
Apidae			
Apis mellifera	42		42
Anthophorini			
Habropoda sp.	21		21
Other Bees	149	2	151
Crabronidae			
Bembix sp.	35		35
Diptera (*Syrphidae, Bombyliidae*, others)	79		79
Other Insects (*Myrmeleontidae, Chrysopidae, Caelifera*, others)	59	20	79
Grand Total	560	276	836

Table S1B: Tabulated environmental measurements from the field site. 3D wind velocity was measured using a Young sonic anemometer. Temperature and humidity were recorded using Hygrochron iButtons (Maxim technologies). Ozone was measured using a 2b Tech Model 202 ozone monitor. Nitrogen Dioxide was measured using a CAPs NO_2 monitor from Aerodyne.

Measurement	mean	Standard deviation
Horizontal wind speed under stable conditions between midnight and 6 am	1.14 m/s	0.48
Air temperature between midnight and 6 am	293.8 K	1.5
Relative humidity between midnight and 6 am	42.6 %	5.0
Atmospheric ozone concentration between midnight and 6 am	37.0 ppb	4.1
Atmospheric nitrogen dioxide concentration between midnight and 6 am	0.72 ppb	0.28

Table S2A:
Table of data for pollinator exclusion treatments

Treatment	Sample size	Fruit set	Proportion of fruit set	Standard Deviation
+ control	63	50	0.794	0.051
pollen supplementation	40	27	0.675	0.0741
total exclusion	44	5	0.114	0.0479
night exclusion	44	21	0.477	0.0753
day exclusion	67	44	0.657	0.058

Table S2B: p-values for pairwise comparisons of population proportions. p value adjustment method: holm

Treatments	total exclusion	pollen supplementation	night exclusion	+ control
pollen supplementation	3.20E-06	-	-	-
night exclusion	0.0032	0.4645	-	-
control	1.70E-10	0.5269	0.0082	-
day exclusion	4.80E-07	1	0.4645	0.4645

Table S3A: Floral volatiles detected by GCMS on an Agilent 7890A GC with a 5975C MSD and Agilent ChemStation software with a NIST mass spectral database.

Peak number	Chemical	RT (min)	Area (Ab*s)	CAS Number	Entry Number Library
1	Butyl aldoxime, 2-methyl-, syn-	7.06	33498739	049805-56-3	4084
2	Butyl aldoxime, 2-methyl-, anti-	7.243	7104293	049805-55-2	4094
3	1R-.alpha.-Pinene	9.565	1351790	007785-70-8	15517
4	Benzaldehyde	10.574	5566457	000100-52-7	5021
5	.beta.-Phellandrene	10.946	42449298	000555-10-2	15529
6	.beta.-Pinene	11.104	7909153	000127-91-3	15500
7	5-Hepten-2-one, 6-methyl-	11.369	3879846	000110-93-0	11254
8	.beta.-Myrcene	11.527	13090398	000123-35-3	15508
9	3-Hexen-1-ol, acetate, (Z)-	12.075	3712957	003681-71-8	19431
10	D-Limonene	12.902	4136525	005989-27-5	15491
11	Eucalyptol	13.034	1.96E+08	000470-82-6	26146
12	1,3,6-Octatriene, 3,7-dimethyl-, (E)-	13.135	4697449	003779-61-1	15616
13	1,3,6-Octatriene, 3,7-dimethyl-, (Z)-	13.526	1.27E+08	003338-55-4	15615
14	Benzoic acid, methyl ester	15.135	1158362	000093-58-3	16113
15	Nonanal	15.501	11963010	000124-19-6	19661
16	Methyl nicotinate	16.561	366348	000093-60-7	16430
17	2-methyl-6-methylene-7-octen-2-ol	17.659	2505832	014314-21-7	26294
18	Methyl salicylate	18.371	85703048	000119-36-8	25364
19	3-Cyclohexene-1-methanol, .alpha.,.alpha.4-trimethyl-	18.46	5243348	000098-55-5	26442
20	Decanal	18.775	2214847	000112-31-2	27694
21	2,6-Octadien-1-ol, 3,7-dimethyl-, (Z)-	19.33	1486435	000106-25-2	26335
22	2,6-Octadienal, 3,7-dimethyl-, (Z)-	19.759	1495466	000106-26-3	24762
23	2,6-Octadien-1-ol, 3,7-dimethyl-, (E)-	20.119	18572226	000106-24-1	26334
24	2,6-Octadienal, 3,7-dimethyl-	20.649	2138733	005392-40-5	24722
25	Indole	21.437	4161258	000120-72-9	8486
26	Benzoic acid, 2-methoxy-, methyl ester	22.598	10271712	000606-45-1	34978
27	Butanoic acid, phenylmethyl ester	22.952	3818777	000103-37-7	42785
28	2-Propenoic acid, 2-methyl-, 2-propynyl ester	27.942	2908096	013861-22-8	10341
29	Benzyl Benzoate	30.364	13972112	000120-51-4	68759

Table S3B: Emission rate in ng/h of chemicals from *Oenothera pallida* floral scent used in the floral scent blend.

Chemical	GCMS peak area (Ab*s)	Emission rate in ng/h
Eucalyptol	196366755	10400
Ocimene	126977354	1900
Methyl salicylate	85765523	7900
2-Methylbutanal oxime	41534408	2900
Nonanal	11963010	850
B-pinene	7914399	99
Benzaldehyde	5605024	230
Indole	4432361	105
Sulcatone	3879846	260
Hexenol acetate	3731065	250
Decanal	2246710	160
Methyl nicotinate	366348	28

Table S3C: syn-enantiomeric excess of 2-methylbutanal oxime in the floral scent sample compared to the synthetic aldoxime. Purity of the synthetic aldoxime was 86.8% as determined by GCMS.

	Real scent aldoxime	Synthetic aldoxime
syn-isomer	33677660	92839367
anti-isomer	7856748	27385080
Total area	41534408	1.2E+08
syn enantiomeric excess	62.2	54.4

Table S4: Comparison of scent blend GCMS peak areas with field *Oenothera pallida* scent sample peak areas and their ratios. Scent blend composition in ng/L of mineral oil is listed in the right column. The enantiomeric excess of syn-2-methylbutanal oxime was 62% in the *O. pallida* sample and 56% in the oxime synthesized for use in the scent blend. β-ocimene was added as a racemic mixture (90% purity, Sigma-Aldrich) such that the required amount of Z-β-ocimene was added.

Blend chemical	Blend area	Sample area	Blend area/ sample area	Blend composition in ng/L
syn-2-methylbutanal oxime	29837496	33677660	0.89	
anti-2-methylbutanal oxime	8484984	7856748	1.08	
Total 2-methylbutanal oxime	40003549	41534408	0.96	123.0
Benzaldehyde	5793203	5605024	1.03	11.4
B-pinene	9073013	7914399	1.15	30.3
Sulcatone	4331040	3879846	1.12	14.6
3-Hexen-1-ol, acetate	3961892	3731065	1.06	20.8
Eucalyptol	189303680	196366755	0.96	2537.4
1,3,6-Octatriene, 3,7-dimethyl-, (Z)-	127280483	126977354	1.00	2708.7
Nonanal	13857700	11963010	1.16	219.1
Methyl nicotinate	273453	366348	0.75	9.1
Methyl salicylate	90422294	85765523	1.05	2594.1
Decanal	2340918	2246710	1.04	789.6
Indole	4719890	4432361	1.06	272.9
Total	491361114	490782803	1.00	

Table S5: Number of *Hyles lineata* and *Manduca sexta* antennae that responded to each of the 12 antennographically active chemicals used in the odor blend. Only male right antennae were used,13 *Hyles* and 8 *Manduca* antennae were measured.

Species	Total runs	2-Methylbutanal oxime	Benzaldehyde	β-pinene	6-methyl-5-hepten-2-one	3-Hexen-1-ol acetate	1,8-cineole
Hyles	13	12	6	12	13	13	13
Manduca	8	8	3	1	4	5	5

Species	Total runs	(Z)-β-ocimene	Nonanal	Methyl nicotinate	Methyl salicylate	Decanal	Indole
Hyles	13	13	13	9	11	10	4
Manduca	8	7	4	0	5	3	1

Table S6: Percentage change in concentration of each of the chemicals in the odor blend upon oxidation be either O_3 alone or O_3 and NO_3. These were measured using a VOCUS PTR ToFMS (TOFWERK AG, Thun, Switzerland), and the oxidation was carried out in a glass flowtube with 3.2 SLM flow, 120 ppb O_3 and 60 ppb NO_2 through a N_2O_5 generator. p values of the changes were computed using the t-test if possible, using the Welch t-test if variances were not equal (determined with Levene's test of homogeneity of variances), and using the Mann-Whitney U-test if the data were not normally distributed (determined with Shapiro Wilk test) (Zar, 2010).

Chemical	Change in concentration with O_3 oxidation	p value	test	Change in concentration with NO_3 & O_3 oxidation	p value	test
2-methylbutanal oxime	0	0.070	t-test	-0.01	0.49	t-test
benzaldehyde	0	9.50E-01	Mann-Whitney U-test	0.02	2.00E-01	Mann-Whitney U-test
β-pinene	-0.33	2.20E-120	Welch t-test	-0.84	4.80E-67	Mann-Whitney U-test
β- ocimene	-0.3	5.00E-54	Mann-Whitney U-test	-0.67	2.10E-171	Welch t-test
Nonanal	0	0.78	t-test	-0.01	0.48	t-test

Table S7A: Sample and visit numbers to the wind tunnel behavior treatments for *Hyles lineata* and *Manduca sexta*.

Species	Treatment	Moths tested	Visits
H. lineata	odor blend	35	5
H. lineata	NO_x oxidized odor blend	19	0
H. lineata	clean air control	42	0
M. sexta	odor blend	12	11
M. sexta	NO_x oxidized odor blend	11	9
M. sexta	1/100 odor blend	14	10
M. sexta	1/100 NO_2 oxidized odor blend	24	17
M. sexta	1/100 O_3 oxidized odor blend	24	15
M. sexta	1/100 NO_x oxidized odor blend	19	8
M. sexta	1/100 blend of oxidized scent	19	7
M. sexta	clean air control	15	5

Table S7B: Table of field hawkmoth visits to the scent treatments and the calculated standard errors of the Poisson means.

Treatment	Scent blend visits	Oxidized blend visits	Control visits	Real scent visits	Visits to real plant
Total visits	14	4	5	13	13
Hours analyzed	49.5	49.5	49.5	43	18
Visits/hour	0.283	0.081	0.101	0.302	0.722
Standard error	0.076	0.040	0.045	0.084	0.200
Visits/7 hour night	1.980	0.566	0.707	2.116	5.056
Standard error	0.529	0.283	0.316	0.587	1.402

Table S7C: Table of field hawkmoth visits to real *Oenothera pallida* plants and individual flowers, and the calculated standard errors of the Poisson means.

Day	Plant visits	Number of flowers	Individual flower visits	Hours analyzed	Flower hours	Visits/flower /hour	Visits/flower /7 hour night
20210804 morning	1	11	2	4.5	49.5	0.040	0.283
20210804 night	8	11	30	7	77	0.390	2.727
20210805 night	4	4	10	6.5	26	0.385	2.692
Total hours/visits	13	26	42	18	152.5	0.275	1.928
					Standard error	0.124	0.866

Table S7D: Generalized linear model results of the field behavioral experiments with a Poisson distribution and logistic link function and the floral odor blend as the comparison group. The model was run using R (R version 4.0.3, The R Foundation for Statistical Computing).

Coefficients	Estimate	Standard Error	Z value	p value
Intercept	2.639	0.267	9.874	<2e-16
Control	-1.03	0.521	-1.976	0.048
NO_x oxidized blend	-1.253	0.567	-2.21	0.027
Real flower	-0.027	0.38	-0.07	0.944
Real scent	0.069	0.372	0.186	0.853

Table S8: Rate constants of reactions (O_3 and NO_3 rates from IUPAC-AERIS) of various floral volatiles with ozone and nitrate radicals and reaction rates with typical northern hemisphere terrestrial O_3 (37 ppb) and NO_3 (2.6 ppt) concentrations.

Chemical	O_3 rate constant in $cm^3molec^{-1}s^{-1}$	NO_3 rate constant in $cm^3molec^{-1}s^{-1}$	Rate in s^{-1} at 37 ppb O_3	Rate in s^{-1} at 2.6 ppt NO_3
β-pinene	1.50E-17	2.51E-12	1.37E-05	0.000161
(Z/E)- ocimene	3.74E-16	2.20E-11	0.000341	0.001408
myrcene	4.70E-16	1.10E-11	0.000428	0.000704
limonene	2.10E-16	1.22E-11	0.000191	0.000781
α-pinene	8.40E-17	6.16E-12	7.65E-05	0.000394
linalool	4.30E-16	1.12E-11	0.000392	0.000717
2-carene	2.30E-16	1.90E-11	0.000209	0.001216
3-carene	3.70E-17	9.10E-12	3.37E-05	0.000582
camphene	9.00E-19	6.60E-13	8.20E-07	4.22E-05
α-phellandrene	3.00E-15	7.30E-11	0.002732	0.004671
β-phellandrene	4.70E-17	8.00E-12	4.28E-05	0.000512
sabinene	8.30E-17	1.00E-11	7.56E-05	0.00064
α-terpinene	2.10E-14	1.40E-10	0.019122	0.008958
γ-terpinene	1.40E-16	2.90E-11	0.000127	0.001856
terpinolene	1.90E-15	9.70E-11	0.00173	0.006207
β-caryophyllene	1.16E-14	1.90E-11	0.010563	0.001216
α-cedrene	2.80E-17	8.20E-12	2.55E-05	0.000525
α-copaene	1.60E-16	1.60E-11	0.000146	0.001024
α-humulene	1.17E-14	3.90E-11	0.010654	0.002495
longifolene	5.00E-19	6.80E-13	4.55E-07	4.35E-05
cis-3-hexen-1-ol	6.40E-17	2.72E-13	5.83E-05	1.74E-05
cis-3-hexenylacetate	5.40E-17	2.46E-13	4.92E-05	1.57E-05
trans-2-hexenal	2.00E-18	1.21E-14	1.82E-06	7.74E-07

Table S9: Table of impacts determined by calculating the floral scent recognition distance using O_3 and NO_3 degradation of the volatiles β-pinene and ocimene, with degradation thresholds of 84% and 67% respectively, and a wind speed of 1 m/s. The impacts were calculated for the respective summertime conditions, with January 2013 O_3 and NO_3 concentrations used for southern hemisphere cities, and July 2013 O_3 and NO_3 concentrations used for northern hemisphere cities. Current recognition distance was also calculated as a percentage of the preindustrial recognition distance. Cities were then ranked according to their current percentage of pre-industrial recognition distance. NO_3 and O_3 distributions were generated using GEOS-Chem standard 12.1.0 with the 2013 emissions inventory and 2013 meteorology with 2 x 2.5 degree grid and 72 vertical levels to 0.01 hPa for January 2013 to February 2014. The pre-industrial NO_3 and O_3 distributions were generated using GEOS-Chem 13.2.1 classic with the 2013 non-anthropogenic emissions inventory and 2013 meteorology with 4 x 5 degree grid and 72 vertical levels to 0.01 hPa for January 2013 to December 2013. City coordinates were obtained from https://www.latlong.net/ and population numbers were obtained from the United Nations World Urbanization Prospects 2018.

City	Population	Regional recognition distance (m)	Current percentage of preindustrial	Impact rank
Tokyo	37,468,000	375	7.6	1
Jakarta	10,517,000	490	7.8	2
Shanghai	25,582,000	238	9.0	3
Los Angeles	12,458,000	137	9.2	4
Madrid	6,497,000	169	11.3	5
New York	18,819,000	274	12.1	6
Riyadh	6,907,000	51	13.9	7
Buenos Aires	14,967,000	370	14.1	8
Dhaka	19,578,000	496	14.1	9
Seoul	9,963,000	417	15.1	10
Paris	10,901,000	328	16.1	11
Johannesburg	5,486,000	382	18.7	12
Tehran	8,896,000	139	20.9	13
Singapore	5,792,000	563	21.5	14
Mexico City	21,581,000	604	22.2	15
Manila	13,482,000	1282	22.4	16
Lima	10,391,000	1066	23.0	17
London	9,046,000	590	24.4	18
Sao Paulo	21,650,000	748	26.5	19
Bogota	10,574,000	2161	31.4	20
Moscow	12,410,000	751	32.0	21
Kuala Lumpur	7,564,000	931	32.5	22
Istanbul	14,751,000	440	34.0	23
Bangkok	10,156,000	1396	36.5	24
Lagos	13,463,000	1012	51.1	25
Karachi	15,400,000	1639	57.7	26
Dehli	28,514,000	259	61.8	27
Sydney	5,231,147	1261	65.8	28
Dar Es Salaam	6,048,000	1866	66.8	29
Kinshasa	13,171,000	1109	77.3	30
Cairo	20,076,000	228	97.4	31

$[O_3] = -k_1[O_3][NO_2] – k_{2x}[VOC_x][O_3]$
$[NO_2] = -k_1[O_3][NO_2] – k_2[NO_3][NO_2] + k_3[N_2O_5]$
$[NO_3] = k_1[O_3][NO_2] – k_2[NO_3][NO_2] + k_3[N_2O_5] – k_{1x}[VOC_x][NO_3]$
$[N_2O_5] = k_2[NO_3][NO_2] - k_3[N_2O_5]$
$[VOC_x] = - k_{1x}[VOC_x][NO_3] – k_{2x}[VOC_x][O_3]$

Equation S1: Equations governing the simulation of NO_3 chemistry in the N_2O_5 generator and flowtube with various volatile organic compounds denoted by VOC_x.

Conclusion

We developed an orthogonal-flow electrospray ionization chemical ionization source for a high-resolution time-of-flight mass spectrometer that can generate a wide variety of reagent ion species from their respective salt solutions. These reagent ion species have a range of charge densities and binding energies, resulting in a range of sensitivities and specificities to different analytes. This will provide versatility in the detection of a wide range of analyte species in the atmosphere to allow for monitoring of ambient atmospheric concentrations of different chemicals and allow the detection of reaction products to investigate the mechanisms of atmospheric chemical reactions.

We have established that nocturnal pollinators are important for fruit set in *Oenothera pallida*, and that the hawkmoths *Hyles lineata* and *Manduca sp.* are the dominant nighttime visitors of *O. pallida*. We have shown that oxidation by atmospherically relevant nitrate radical concentrations results in a more severe degradation of many floral scent compounds compared to ozone oxidation, and that this scent degradation results in reduced hawkmoth visitation via the degradation of the monoterpene component of the odor blend. These effects are likely to be generalizable to other plant-pollinator systems as monoterpenes are the most common floral scent component in the families of seed plants, and monoterpenes have been shown to be important for pollinator recognition of floral scent in other systems. Our analytical framework is also applicable towards estimating the impacts in other scent recognition systems if the relevant volatiles and rate constants in those systems can be determined.

Global chemical modeling with GEOS-Chem shows that scent recognition distances in the regions around many major cities around the world have likely fallen to below 30% of pre-industrial recognition distances, and that the largest changes in scent recognition distance have

occurred in the more urban regions of the world like Europe, Southern and Eastern Asia, North America, and parts of South America. However, the factors determining local impacts are a complex interaction of human and natural NO_x emissions combined with local geography and meteorology that determines the local NO_x and ozone levels.

These findings raise the question of why monoterpenes continue to be important in floral scent recognition despite their historical susceptibility to atmospheric degradation. I propose that this is because it makes monoterpenes a more salient signal for floral resources. This topic should be investigated further, possibly by studying a number of other systems to see if other systems also include key scent chemicals for recognition that are highly sensitive to atmospheric oxidation, and studying any exceptions to this rule.

The effects of the hydroxy radical (OH) should also be studied, since OH is the most powerful oxidant in the atmosphere, and because OH chemistry occurs during the day, when most pollinators are active, as opposed to nitrate radical chemistry which principally occurs at night.

Finally, atmospheric degradation of scent signals is only one of the ways by which olfactory navigation is impacted by air pollution. For example, atmospheric oxidants have also been shown to impact the emitters and receivers of scent signals, and other components of air pollution such as aerosols and volatile organic compounds have also been shown to impact scent recognition. A more wholistic study should be undertaken to understand what the total impacts are in different localities, and which factors have the largest influence, as this could influence policy decisions on particularly vulnerable systems.

Bibliography

Aernecke, M. J., Mendum, T., Geurtsen, G., Ostrinskaya, A., & Kunz, R. R. (2015). Vapor Pressure of Hexamethylene Triperoxide Diamine (HMTD) Estimated Using Secondary Electrospray Ionization Mass Spectrometry. *The Journal of Physical Chemistry. A, Molecules, Spectroscopy, Kinetics, Environment, & General Theory*, 119(47), 11514–11522. https://doi.org/10.1021/acs.jpca.5b08929

Aljawhary, D., Lee, A. K. Y., & Abbatt, J. P. D. (2013). High-resolution chemical ionization mass spectrometry (ToF-CIMS): application to study SOA composition and processing. *Atmospheric Measurement Techniques*, 6(11), 3211–3224. https://doi.org/10.5194/amt-6-3211-2013

Amorim, F. W., Wyatt, G. E., & Sazima, M. (2014). Low abundance of long-tongued pollinators leads to pollen limitation in four specialized hawkmoth-pollinated plants in the Atlantic Rain forest, Brazil. *Die Naturwissenschaften*, *101*(11), 893–905. https://doi.org/10.1007/s00114-014-1230-y

Amos, H. M., Jacob, D. J., Holmes, C. D., Fisher, J. A., Wang, Q., Yantosca, R. M., et al. (2012). Gas-particle partitioning of atmospheric Hg(II) and its effect on global mercury deposition. *Atmospheric Chemistry and Physics*, *12*(1), 591–603. https://doi.org/10.5194/acp-12-591-2012

Barrios-Collado, C., García-Gómez, D., Zenobi, R., Vidal-de-Miguel, G., Ibáñez, A. J., & Martinez-Lozano Sinues, P. (2016). Capturing in Vivo Plant Metabolism by Real-Time Analysis of Low to High Molecular Weight Volatiles. *Analytical Chemistry (Washington)*, 88(4), 2406–2412. https://doi.org/10.1021/acs.analchem.5b04452

Bates, K. H., & Jacob, D. J. (2019). A new model mechanism for atmospheric oxidation of isoprene: global effects on oxidants, nitrogen oxides, organic products, and secondary organic aerosol. *Atmospheric Chemistry and Physics*, *19*(14), 9613–9640. https://doi.org/10.5194/acp-19-9613-2019

Bean, H. D., Mellors, T. R., Zhu, J., & Hill, J. E. (1900). Profiling Aged Artisanal Cheddar Cheese Using Secondary Electrospray Ionization Mass Spectrometry. *Journal of Agricultural and Food Chemistry*, 63(17), 4386–4392. https://doi.org/10.1021/jf5063759

Bell, R. A., & Joachim, F. G. (1976). Techniques for Rearing Laboratory Colonies of Tobacco Hornworms and Pink Bollworms. *Annals of the Entomological Society of America*, *69*(2), 365–373.

Berndt, T., Richters, S., Jokinen, T., Hyttinen, N., Kurten, T., Otkjaer, R. V., Kjaergaard, H. G., Stratmann, F., Herrmann, H., Sipila, M., Kulmala, M., & Ehn, M. (2016). Hydroxyl radical-induced formation of highly oxidized organic compounds. *Nature Communications*, 7(1), 13677–13677. https://doi.org/10.1038/ncomms13677

Bertram, T. H., Kimmel, J. R., Crisp, T. A., Ryder, O. S., Yatavelli, R. L. N., Thornton, J. A., Cubison, M. J., Gonin, M., & Worsnop, D. R. (2011). A field-deployable, chemical ionization time-of-flight mass spectrometer. *Atmospheric Measurement Techniques*, 4(7), 1471–1479. https://doi.org/10.5194/amt-4-1471-2011

Bey, I., Jacob, D. J., Yantosca, R. M., Logan, J. A., Field, B. D., Fiore, A. M., Li, Q.-B., Liu, H.-Y., Mickley, L. J., & Schultz, M. G. (2001). Global modeling of tropospheric chemistry with assimilated meteorology: Model description and evaluation. *Journal of Geophysical Research*, *106*(D19), 23073–23095. https://doi.org/10.1029/2001JD000807

Böhringer, H., Fahey, D. ., Lindinger, W., Howorka, F., Fehsenfeld, F. ., & Albritton, D. . (1987). Mobilities of several mass-identified positive and negative ions in air. *International Journal of Mass Spectrometry and Ion Processes*, 81, 45–65. https://doi.org/10.1016/0168-1176(87)80005-8

Breitenlechner, M., Fischer, L., Hainer, M., Heinritzi, M., Curtius, J., & Hansel, A. (2017). PTR3: An Instrument for Studying the Lifecycle of Reactive Organic Carbon in the Atmosphere. *Analytical Chemistry (Washington)*, 89(11), 5824–5831. https://doi.org/10.1021/acs.analchem.6b05110

Broadhead, G. T., Basu, T., von Arx, M., & Raguso, R. A. (2017). Diel rhythms and sex differences in the locomotor activity of hawkmoths. *Journal of Experimental Biology*, *220*(Pt 8), 1472–1480. https://doi.org/10.1242/jeb.143966

Brophy, P. & Farmer, D. K. (2015). A switchable reagent ion high resolution time-of-flight chemical ionization mass spectrometer for real-time measurement of gas phase oxidized species: characterization from the 2013 southern oxidant and aerosol study. *Atmospheric Measurement Techniques*, 8(7), 2945–2959. https://doi.org/10.5194/amt-8-2945-2015

Brophy, P., & Farmer, D. K. (2016). Clustering, methodology, and mechanistic insights into acetate chemical ionization using high-resolution time-of-flight mass spectrometry. *Atmospheric Measurement Techniques*, 9(8), 3969–3986. https://doi.org/10.5194/amt-9-3969-2016

Brownell Jr R. L., Ralls, K., Baumann-Pickering, S., & Poole, M. M. (2009). Behavior of melon-headed whales, Peponocephala electra, near oceanic islands. Marine Mammal Science, 25(3), 639–658. https://doi.org/10.1111/j.1748-7692.2009.00281.x

Chen, Y. H., Hill Jr, H. H., & Wittmer, D. P. (1994). Analytical merit of electrospray ion mobility spectrometry as a chromatographic detector. *The Journal of Microcolumn Separations*, 6(5), 515–524. https://doi.org/10.1002/mcs.1220060511

Cook, B., Haverkamp, A., Hansson, B. S., Roulston, T., Lerdau, M., & Knaden, M. (2020). Pollination in the Anthropocene: a Moth Can Learn Ozone-Altered Floral Blends. *Journal of Chemical Ecology*, *46*(10), 987–996. https://doi.org/10.1007/s10886-020-01211-4

Crounse, J. D., McKinney, K. A., Kwan, A. J., & Wennberg, P. O. (2006). Measurement of Gas-Phase Hydroperoxides by Chemical Ionization Mass Spectrometry. *Analytical Chemistry (Washington)*, 78(19), 6726–6732. https://doi.org/10.1021/ac0604235

Damljanovic, Vukicevic, M., & Vukicevic, R. D. (2006). A Simple Synthesis of Oximes. *Monatshefte Für Chemie*, *137*(3), 301–305. https://doi.org/10.1007/s00706-005-0427-3

Démares,F., Gibert, L., Creusot, P., Lapeyre, B., & Proffit, M. (2022). Acute ozone exposure impairs detection of floral odor, learning, and memory of honey bees, through olfactory generalization. *The Science of the Total Environment*, 827, 154342–154342. https://doi.org/10.1016/j.scitotenv.2022.154342

Dötterl, S., Vater, M., Rupp, T., & Held, A. (2016). Ozone Differentially Affects Perception of Plant Volatiles in Western Honey Bees. *Journal of Chemical Ecology*, *42*(6), 486–489. https://doi.org/10.1007/s10886-016-0717-8

Dominoni, D. M., Halfwerk, W., Baird, E., Buxton, R. T., Fernández-Juricic, E., Fristrup, K. M., … Barber, J. R. (2020). Why conservation biology can benefit from sensory ecology. *Nature Ecology & Evolution*, *4*(4), 502–511. https://doi.org/10.1038/s41559-020-1135-4

Dubuisson, C., Nicolè, F., Buatois, B., Hossaert-McKey, M., & Proffit, M. (2022). Tropospheric Ozone Alters the Chemical Signal Emitted by an Emblematic Plant of the Mediterranean Region: The True Lavender (Lavandula angustifolia Mill.). *Frontiers in Ecology and Evolution*, *10*. https://doi.org/10.3389/fevo.2022.795588

Edwards, P. M., Aikin, K. C., Dube, W. P., Fry, J. L., Gilman, J. B., de Gouw, J. A., Graus, M. G., Hanisco, T. F., Holloway, J., Hübler, G., Kaiser, J., Keutsch, F. N., Lerner, B. M., Neuman, J. A., Parrish, D. D., Peischl, J., Pollack, I. B., Ravishankara, A. R., Roberts, J. M., … Brown, S. S. (2017). Transition from high- to low-NOx control of night-time oxidation in the southeastern US. *Nature Geoscience*, *10*(7), 490–495. https://doi.org/10.1038/ngeo2976

Ehn, M., Kleist, E., Junninen, H., Petaja, T., Lonn, G., Schobesberger, S., Dal Maso, M., Trimborn, A., Kulmala, M., Worsnop, D. R., Wahner, A., Wildt, J., & Mentel, T. F. (2012). Gas phase formation of extremely oxidized pinene reaction products in chamber and ambient air. *Atmospheric Chemistry and Physics*, 12(11), 5113–5127. https://doi.org/10.5194/acp-12-5113-2012

Ehn, M., Thornton, J. A., Kleist, E., Sipila, M., Junninen, H., Pullinen, I., Springer, M., Rubach, F., Tillmann, R., Lee, B., Lopez-Hilfiker, F., Andres, S., Acir, I.-H., Rissanen, M., Jokinen, T., Schobesberger, S., Kangasluoma, J., Kontkanen, J., Nieminen, T., … Mentel, T. F. (2014). A large source of low-volatility secondary organic aerosol. *Nature (London)*, 506(7489), 476–479. https://doi.org/10.1038/nature13032

Ellis, H. W., McDaniel, E. W., Albritton, D. L., Viehland, L. A., Lin, S. L., & Mason, E. A. (1978). Transport properties of gaseous ions over a wide energy range. Part II. *Atomic Data and Nuclear Data Tables*, 22(3), 179–217. https://doi.org/10.1016/0092-640X(78)90014-1

Farré-Armengol, G., Peñuelas, J., Li, T., Yli-Pirilä, P., Filella, I., Llusia, J., & Blande, J. D. (2016). Ozone degrades floral scent and reduces pollinator attraction to flowers. *The New Phytologist*, *209*(1), 152–160. https://doi.org/10.1111/nph.13620

Farré-Armengol, G., Fernández-Martínez, M., Filella, I., Junker, R. R., & Peñuelas, J. (2020). Deciphering the Biotic and Climatic Factors That Influence Floral Scents: A Systematic Review of Floral Volatile Emissions. Frontiers in Plant Science, 11, 1154–1154. https://doi.org/10.3389/fpls.2020.01154

Farrell, R. R., Fahrentrapp, J., García-Gómez, D., Martinez-Lozano Sinues, P., & Zenobi, R. (2017). Rapid fingerprinting of grape volatile composition using secondary electrospray ionization orbitrap mass spectrometry: A preliminary study of grape ripening. *Food Control*, 81, 107–112. https://doi.org/10.1016/j.foodcont.2017.04.041

Finlayson-Pitts, B. J., & Pitts, J. N. (2000). Chemistry of the upper and lower atmosphere : theory, experiments, and applications. *Academic Press*.

Firebaugh, A., & Haynes, K. J. (2016). Experimental tests of light-pollution impacts on nocturnal insect courtship and dispersal. *Oecologia*, *182*(4), 1203–1211. https://doi.org/10.1007/s00442-016-3723-1Fuentes, J. D., Chamecki, M., Roulston, T., Chen, B., & Pratt, K. R. (2016). Air pollutants degrade floral scents and increase insect foraging times. *Atmospheric Environment (1994)*, *141*, 361–374. https://doi.org/10.1016/j.atmosenv.2016.07.002

Fisher, J., Jacob, D. J., Travis, K. R., Kim, P. S., Marais, E. A., Miller, C. C., Yu, K., Zhu, L., Yantosca, R. M., Sulprizio, M. P., Hanisco, T. F., & Wolfe, G. M. (2016). Organic Nitrate Chemistry and Its Implications for Nitrogen Budgets in an Isoprene- and Monoterpene-Rich Atmosphere: Constraints From Aircraft (SEAC4RS) and Ground-Based (SOAS) Observations in the Southeast US. *Atmospheric Chemistry and Physics*, *16*(9), 5969–5991. https://doi.org/10.5194/acp-16-5969-2016

Fortner, E. C., Zhao, J., & Zhang, R. (2004). Development of Ion Drift-Chemical Ionization Mass Spectrometry. *Analytical Chemistry (Washington)*, 76(18), 5436–5440. https://doi.org/10.1021/ac0493222

Fujii, T., Selvin, P. C., Sablier, M., & Iwase, K. (2001). Lithium ion attachment mass spectrometry for on-line analysis of trace components in air: direct introduction. *International Journal of Mass Spectrometry*, 209(1), 39–45. https://doi.org/10.1016/S1387-3806(01)00469-9

Gao, Y. Q., Hall, W. A., & Johnston, M. V. (2010). Molecular Composition of Monoterpene Secondary Organic Aerosol at Low Mass Loading. *Environmental Science & Technology*, 44(20), 7897–7902. https://doi.org/10.1021/es101861k

García-Gómez, D., Bregy, L., Barrios-Collado, C., Vidal-de-Miguel, G., & Zenobi, R. (2015). Real-Time High-Resolution Tandem Mass Spectrometry Identifies Furan Derivatives in Exhaled Breath. *Analytical Chemistry (Washington)*, 87(13), 6919–6924. https://doi.org/10.1021/acs.analchem.5b01509

García-Gómez, D., Gaisl, T., Barrios-Collado, C., Vidal-de-Miguel, G., Kohler, M., & Zenobi, R. (2016). Real-Time Chemical Analysis of E-Cigarette Aerosols By Means Of Secondary Electrospray Ionization Mass Spectrometry. *Chemistry : a European Journal*, 22(7), 2452–2457. https://doi.org/10.1002/chem.201504450

Garvey, J. F., Herron, W. J., & Vaidyanathan, G. (1995). ChemInform Abstract: Probing the Structure and Reactivity of Hydrogen-Bonded Clusters of the Type (M)n(H2O)H+, via the Observation of Magic Numbers. *ChemInform*, 26(7), no–no. https://doi.org/10.1002/chin.199507349

Gelaro, R., McCarty, W., Suarez, M. J., Todling, R., Molod, A., Takacs, L., Randles, C., Darmenov, A., Bosilovich, M. G., Reichle, R., Wargan, K., Coy, L., Cullather, R., Draper, C., Akella, S., Buchard, V., Conaty, A., da Silva, A., Gu, W., … Zhao, B. (2017). The Modern-Era Retrospective Analysis for Research and Applications, Version 2 (MERRA-2). *Journal of Climate*, *30*(14), 5419–5454. https://doi.org/10.1175/JCLI-D-16-0758.1

Girling, R. D., Lusebrink, I., Farthing, E., Newman, T. A., & Poppy, G. M. (2013). Diesel exhaust rapidly degrades floral odours used by honeybees. *Scientific Reports*, *3*(1), 2779–. https://doi.org/10.1038/srep02779

Goldstein, A. H., & Galbally, I. E. (2007). Known and Unexplored Organic Constituents in the Earth's Atmosphere. *Environmental Science & Technology*, 41(5), 1514–1521. https://doi.org/10.1021/es072476p

Graham, R. A., & Johnston, H. S. (1978). The photochemistry of the nitrate radical and the kinetics of the nitrogen pentoxide-ozone system. *Journal of Physical Chemistry (1952)*, *82*(3), 254–268. https://doi.org/10.1021/j100492a002

Gregory, D. (1964). Hawkmoth Pollination in the Genus Oenothera. *Aliso*, *5*(4), 385–419. https://doi.org/10.5642/aliso.19640504.02

Guenther, A. B., Jiang, X., Heald, C. L., Sakulyanontvittaya, T., Duhl, T., Emmons, L. K., & Wang, X. (2012). The model of emissions of gases and aerosols from nature version 2.1 (MEGAN2.1): An extended and updated framework for modeling biogenic emissions. *Geoscientific Model Development*, *5*(6), 1471–1492. https://doi.org/10.5194/gmd-5-1471-2012

Haber, W. A. & Frankie, G. W. (1989). A tropical hawkmoth community: Costa Rican dry forest Sphingidae. *Biotropica*, *21*(2), 155–172. https://doi.org/10.2307/2388706

Hirokawa, J., Kato, T., & Mafuné, F. (2009). In Situ Measurements of Atmospheric Nitrous Acid by Chemical Ionization Mass Spectrometry Using Chloride Ion Transfer Reactions. *Analytical Chemistry (Washington)*, 81(20), 8380–8386. https://doi.org/10.1021/ac901117b

Holmes, C. D., Bertram, T. H., Confer, K. L., Graham, K. A., Ronan, A. C., Wirks, C. K., & Shah, V. (2019). The Role of Clouds in the Tropospheric NO x Cycle: A New Modeling Approach for Cloud Chemistry and Its Global Implications. *Geophysical Research Letters*, *46*(9), 4980–4990. https://doi.org/10.1029/2019GL081990

Horning, E. C., Carroll, D. I., Dzidic, I., Haegele, K. D., Horning, M. G., & Stillwell, R. N. (1974). Liquid chromatograph—mass spectrometer—computer analytical systems. *Journal of Chromatography A*, 99, 13–21. https://doi.org/10.1016/S0021-9673(00)90841-0

Hu, L., Millet, D. B., Baasandorj, M., Griffis, T. J., Turner, P., Helmig, D., et al. (2015). Isoprene emissions and impacts over an ecological transition region in the U.S. Upper Midwest inferred from tall tower measurements. *Journal of Geophysical Research: Atmospheres*, *120*(8), 3553–3571. https://doi.org/10.1002/2014JD022732

Huang, M., Carmichael, G. R., Pierce, R. B., Jo, D. S., Park, R. J., Flemming, J., Emmons, L. K., Bowman, K. W., Henze, D. K., Davila, Y., Sudo, K., Jonson, J. E., Lund, M. T., Janssens-Maenhout, G., Dentener, F. J., Keating, T. J., Oetjen, H., & Payne, V. H. (2017). Impact of intercontinental pollution transport on North American ozone air pollution: an HTAP phase 2 multi-model study. *Atmospheric Chemistry and Physics*, *17*(9), 5721–5750. https://doi.org/10.5194/acp-17-5721-2017

Hudman, R. C., Moore, N. E., Mebust, A. K., Martin, R. v., Russell, A. R., Valin, L. C., & Cohen, R. C. (2012). Steps towards a mechanistic model of global soil nitric oxide emissions: implementation and space based-constraints. *Atmospheric Chemistry and Physics*, *12*(16), 7779–7795. https://doi.org/10.5194/acp-12-7779-2012

Huey, L. G., Hanson, D. R., & Howard, C. J. (1995). Reactions of SF6- and I- with Atmospheric Trace Gases. *Journal of Physical Chemistry* (1952), 99(14), 5001–5008. https://doi.org/10.1021/j100014a021

Huey. L. G. (2007). Measurement of trace atmospheric species by chemical ionization mass spectrometry: Speciation of reactive nitrogen and future directions. *Mass Spectrometry Reviews*, 26(2), 166–184. https://doi.org/10.1002/mas.20118

Hyttinen, N., Kupiainen-Määttä, O., Rissanen, M. P., Muuronen, M., Ehn, M., & Kurtén, T. (1900). Modeling the Charging of Highly Oxidized Cyclohexene Ozonolysis Products Using Nitrate-Based Chemical Ionization. *The Journal of Physical Chemistry. A, Molecules, Spectroscopy, Kinetics, Environment, & General Theory*, 119(24), 6339–6345. https://doi.org/10.1021/acs.jpca.5b01818

II, R. E. S. (1976). A New Method for Studying Pollen Dispersal Using Micronized Fluorescent Dusts. *The American Midland Naturalist*, *96*(1), 241–245. https://doi.org/10.2307/2424586

Inomata, S. & Hirokawa, J. (2017). Non-radioactive Chemical Ionization Mass Spectrometry Using Acetic Acid–Acetate Cluster as a Reagent Ion for the Real-time Measurement of Acids and Hydroperoxides. *Chemistry Letters*, 46(1), 38–41. https://doi.org/10.1246/cl.160828

IUPAC-AERIS Evaluated Kinetic Data (2022) Database maintained by the Task Group on Atmospheric Chemical Kinetic Data Evaluation. https://iupac.aeris-data.fr/en/home/

Iyer, S., Lopez-Hilfiker, F., Lee, B. H., Thornton, J. A., & Kurtén, T. (2016). Modeling the Detection of Organic and Inorganic Compounds Using Iodide-Based Chemical Ionization. The *Journal of Physical Chemistry. A, Molecules, Spectroscopy, Kinetics, Environment, & General Theory*, 120(4), 576–587. https://doi.org/10.1021/acs.jpca.5b09837

Jokinen, T., Berndt, T., Makkonen, R., Kerminen, V.-M., Junninen, H., Paasonen, P., Stratmann, F., Herrmann, H., Guenther, A. B., Worsnop, D. R., Kulmala, M., Ehn, M., & Sipila, M. (2015). Production of extremely low volatile organic compounds from biogenic emissions: Measured yields and atmospheric implications. *Proceedings of the National Academy of Sciences - PNAS*, 112(23), 7123–7128. https://doi.org/10.1073/pnas.1423977112

Junninen, H., Ehn, M., Petaja, T., Luosujarvi, L., Kotiaho, T., Kostiainen, R., Rohner, U., Gonin, M., Fuhrer, K., Kulmala, M., & Worsnop, D. R. (2010). A high-resolution mass spectrometer to measure atmospheric ion composition. *Atmospheric Measurement Techniques*, 3(4), 1039–1053. https://doi.org/10.5194/amt-3-1039-2010

Kataoka, H., Troetschler, R. G., Li, J. P., Kramer, S. J., Carney, R. L., & Schooley, D. A. (1989). Isolation and identification of a diuretic hormone from the tobacco hornworm, Manduca sexta. *Proceedings of the National Academy of Sciences - PNAS*, *86*(8), 2976–2980. https://doi.org/10.1073/pnas.86.8.2976

Kercher, J. P., Riedel, T. P., & Thornton, J. A. (2009). Chlorine activation by N2O5: simultaneous, in situ detection of ClNO2 and N2O5 by chemical ionization mass spectrometry. *Atmospheric Measurement Techniques*, 2(1), 193–204. https://doi.org/10.5194/amt-2-193-2009

Khan, M. A. H., Cooke, M. C., Utembe, S. R., Archibald, A. T., Derwent, R. G., Xiao, P., Percival, C. J., Jenkin, M. E., Morris, W. C., & Shallcross, D. E. (2015). Global modeling of the nitrate radical (NO3) for present and pre-industrial scenarios. *Atmospheric Research*, *164-165*, 347–357. https://doi.org/10.1016/j.atmosres.2015.06.006

Kim, M. J., Zoerb, M. C., Campbell, N. R., Zimmermann, K. J., Blomquist, B. W., Huebert, B. J., & Bertram, T. H. (2016). Revisiting benzene cluster cations for the chemical ionization of dimethyl sulfide and select volatile organic compounds. *Atmospheric Measurement Techniques*, 9(4), 1473–1484. https://doi.org/10.5194/amt-9-1473-2016

Knudsen, J. T., Eriksson, R., Gershenzon, J., & Ståhl, B. (2006). Diversity and Distribution of Floral Scent. *The Botanical Review*, *72*(1), 1–120. https://doi.org/10.1663/0006-8101(2006)72[1:DADOFS]2.0.CO;2

Krakos, K. N., & Fabricant, S. A. (2014). Generalist versus specialist pollination systems in 26 Oenothera (Onagraceae). Journal of Pollination Ecology, 14, 235–243. https://doi.org/10.26786/1920-7603(2014)23

Krechmer, J., Lopez-Hilfiker, F., Koss, A., Hutterli, M., Stoermer, C., Deming, B., Kimmel, J., Warneke, C., Holzinger, R., Jayne, J., Worsnop, D., Fuhrer, K., Gonin, M., & de Gouw, J. (2018). Evaluation of a New Reagent-Ion Source and Focusing Ion–Molecule Reactor for Use in Proton-Transfer-Reaction Mass Spectrometry. *Analytical Chemistry (Washington)*, *90*(20), 12011–12018. https://doi.org/10.1021/acs.analchem.8b02641

Kristensen, K., Watne, Å. K., Hammes, J., Lutz, A., Petäjä, T., Hallquist, M., Bilde, M., & Glasius, M. (2016). High-Molecular Weight Dimer Esters Are Major Products in Aerosols from α-Pinene Ozonolysis and the Boreal Forest. *Environmental Science & Technology*, 3(8), 280–285. https://doi.org/10.1021/acs.estlett.6b00152

Laboratory for Atmospheric Research The Tri-Cities Ozone Precursor Study (2017) Final Report by Laboratory for Atmospheric Research, Department of Civil & Environmental Engineering, Washington State University. https://ecology.wa.gov/DOE/files/93/934a2f46-b000-4f9a-837c-a286ccfa615e.pdf

Laskin, A., Laskin, J., & Nizkorodov, S. A. (2012). Mass spectrometric approaches for chemical characterisation of atmospheric aerosols: critical review of the most recent advances. *Environmental Chemistry*, 9(3), 163–189. https://doi.org/10.1071/EN12052

Lavi, A., Vermeuel, M. P., Novak, G. A., & Bertram, T. H. (2018). The sensitivity of benzene cluster cation chemical ionization mass spectrometry to select biogenic terpenes. *Atmospheric Measurement Techniques*, *11*(6), 3251–3262. https://doi.org/10.5194/amt-11-3251-2018

Lee, B. H., Lopez-Hilfiker, F. D., Mohr, C., Kurtén, T., Worsnop, D. R., & Thornton, J. A. (2014). An Iodide-Adduct High-Resolution Time-of-Flight Chemical-Ionization Mass Spectrometer: Application to Atmospheric Inorganic and Organic Compounds. *Environmental Science & Technology*, 48(11), 6309–6317. https://doi.org/10.1021/es500362a

Lee, B. H., Mohr, C., Lopez-Hilfiker, F. D., Lutz, A., Hallquist, M., Lee, L., Romer, P., Cohen, R. C., Iyer, S., Kurten, T., Hu, W., Day, D. A., Campuzano-Jost, P., Jimenez, J. L., Xu, L., Ng, N. L., Guo, H., Weber, R. J., Wild, R. J., … Thornton, J. A. (2016). Highly functionalized organic nitrates in the southeast United States: Contribution to secondary organic aerosol and reactive nitrogen budgets. *Proceedings of the National Academy of Sciences - PNAS*, 113(6), 1516–1521. https://doi.org/10.1073/pnas.1508108113

Lopez-Hilfiker, F. D., Mohr, C., Ehn, M., Rubach, F., Kleist, E., Wildt, J., Mentel, T. F., Lutz, A., Hallquist, M., Worsnop, D., & Thornton, J. A. (2014). A novel method for online analysis of gas and particle composition: description and evaluation of a Filter Inlet for Gases and AEROsols (FIGAERO). *Atmospheric Measurement Techniques*, 7(4), 983–1001. https://doi.org/10.5194/amt-7-983-2014

Lopez-Hilfiker, F. D., Mohr, C., Ehn, M., Rubach, F., Kleist, E., Wildt, J., Mentel, T. F., Carrasquillo, A. J., Daumit, K. E., Hunter, J. F., Kroll, J. H., Worsnop, D. R., & Thornton, J. A. (2015). Phase partitioning and volatility of secondary organic aerosol components formed from alpha-pinene ozonolysis and OH oxidation: the importance of accretion products and other low volatility compounds. *Atmospheric Chemistry and Physics*, 15(14), 7765–7776. https://doi.org/10.5194/acp-15-7765-2015

Lopez-Hilfiker, F. D., Iyer, S., Mohr, C., Lee, B. H., D'Ambro, E. L., Kurten, T., & Thornton, J. A. (2016a). Constraining the sensitivity of iodide adduct chemical ionization mass spectrometry to multifunctional organic molecules using the collision limit and thermodynamic stability of iodide ion adducts. *Atmospheric Measurement Techniques*, 9(4), 1505–1512. https://doi.org/10.5194/amt-9-1505-2016

Lopez-Hilfiker, F. D., Mohr, C., D'Ambro, E. L., Lutz, A., Riedel, T. P., Gaston, C. J., Iyer, S., Zhang, Z., Gold, A., Surratt, J. D., Lee, B. H., Kurten, T., Hu, W. W., Jimenez, J., Hallquist, M., & Thornton, J. A. (2016b). Molecular Composition and Volatility of Organic Aerosol in the Southeastern US: Implications for IEPDX Derived SOA. *Environmental Science & Technology*, 50(5), 2200–2209. https://doi.org/10.1021/acs.est.5b04769

Luo, G., Yu, F., & Moch, J. M. (2020). Further improvement of wet process treatments in GEOS-Chem v12.6.0: Impact on global distributions of aerosols and aerosol precursors. *Geoscientific Model Development*, *13*(6), 2879–2903. https://doi.org/10.5194/gmd-13-2879-2020

Mao, J., Jacob, D. J., Evans, M. J., Olson, J. R., Ren, X., Brune, W. H., St Clair, J. M., Crounse, J. D., Spencer, K. M., Beaver, M. R., Wennberg, P. O., Cubison, M. J., Jimenez, J. L., Fried, A., Weibring, P., Walega, J. G., Hall, S. R., Weinheimer, A. J., Cohen, R. C., … Carouge, C. (2010). Chemistry of hydrogen oxide radicals (HOx) in the Arctic troposphere in spring. *Atmospheric Chemistry and Physics*, *10*(13), 5823–5838. https://doi.org/10.5194/acp-10-5823-2010

Mao, J., Paulot, F., Jacob, D. J., Cohen, R. C., Crounse, J. D., Wennberg, P. O., Keller, C. A., Hudman, R. C., Barkley, M. P., & Horowitz, L. W. (2013). Ozone and organic nitrates over the eastern United States: Sensitivity to isoprene chemistry: OZONE AND ORGANIC NITRATES OVER EAST U.S. *Journal of Geophysical Research. Atmospheres*, *118*(19), 11–11,268. https://doi.org/10.1002/jgrd.50817

Martínez-Lozano, P., Zingaro, L., Finiguerra, A., & Cristoni, S. (2011). Secondary electrospray ionization-mass spectrometry: breath study on a control group. *Journal of Breath Research*, 5(1), 016002–016002. https://doi.org/10.1088/1752-7155/5/1/016002

Matthews, M., & Sponberg, S. (2018). Hawkmoth flight in the unsteady wakes of flowers. Journal of Experimental Biology, 221(22). https://doi.org/10.1242/jeb.179259

McDuffie, E. E., Fibiger, D. L., Dubé, W. P., Lopez-Hilfiker, F., Lee, B. H., Thornton, J. A., et al. (2018). Heterogeneous N 2 O 5 Uptake During Winter: Aircraft Measurements During the 2015 WINTER Campaign and Critical Evaluation of Current Parameterizations. *Journal of Geophysical Research: Atmospheres*, *123*(8), 4345–4372. https://doi.org/10.1002/2018JD028336

Meier, L., Berchtold, C., Schmid, S., & Zenobi, R. (2012). Sensitive detection of drug vapors using an ion funnel interface for secondary electrospray ionization mass spectrometry. *Journal of Mass Spectrometry*., 47(5), 555–559. https://doi.org/10.1002/jms.2982

Mofikoya, A. O., Yli-Pirilä, P., Kivimäenpää, M., Blande, J. D., Virtanen, A., & Holopainen, J. K. (2020). Deposition of α-pinene oxidation products on plant surfaces affects plant VOC emission and herbivore feeding and oviposition. *Environmental Pollution (1987)*, *263*(Pt B), 114437–114437. https://doi.org/10.1016/j.envpol.2020.114437

Mohr, C., Lopez-Hilfiker, F. D., Yli-Juuti, T., Heitto, A., Lutz, A., Hallquist, M., D'Ambro, E. L., Rissanen, M. P., Hao, L., Schobesberger, S., Kulmala, M., Mauldin, R. L., Makkonen, U., Mylne K. R. (1992). Concentration fluctuation measurements in a plume dispersing in a stable surface layer. *Boundary - Layer Meteorology*, *60*(1-2), 15–48. https://doi.org/10.1007/BF00122060

Ng, N. L., Brown, S. S., Archibald, A. T., Atlas, E., Cohen, R. C., Crowley, J. N., Day, D. A., Donahue, N. M., Fry, J. L., Fuchs, H., Griffin, R. J., Guzman, M. I., Herrmann, H., Hodzic, A., Iinuma, Y., Jimenez, J. L., Kiendler-Scharr, A., Lee, B. H., Luecken, D. J., … Zaveri, R. A. (2017). Nitrate radicals and biogenic volatile organic compounds: oxidation, mechanisms, and organic aerosol. *Atmospheric Chemistry and Physics*, *17*(3), 2103–2162. https://doi.org/10.5194/acp-17-2103-2017

Nguyen, T. B., Bateman, A. P., Bones, D. L., Nizkorodov, S. A., Laskin, J., & Laskin, A. (2010). High-resolution mass spectrometry analysis of secondary organic aerosol generated by ozonolysis of isoprene. *Atmospheric Environment* (1994), 44(8), 1032–1042. https://doi.org/10.1016/j.atmosenv.2009.12.019

Nizkorodov, S. A., Laskin, J., & Laskin, A. (2011). Molecular chemistry of organic aerosols through the application of high resolution mass spectrometry. *Physical Chemistry Chemical Physics : PCCP*, 13(9), 3612–3629. https://doi.org/10.1039/c0cp02032j

Nowak, J. B., Huey, L. G., Eisele, F. L., Tanner, D. J., Mauldin III, R. L., Cantrell, C., Kosciuch, E., & Davis, D. D. (2002). Chemical ionization mass spectrometry technique for detection of dimethylsulfoxide and ammonia. *Journal of Geophysical Research*, 107(D18), ACH 10–1–ACH 10–8. https://doi.org/10.1029/2001JD001058

Nozière, B., Kalberer, M., Claeys, M., Allan, J., D'Anna, B., Decesari, S., Finessi, E., Glasius, M., Grgić, I., Hamilton, J. F., Hoffmann, T., Iinuma, Y., Jaoui, M., Kahnt, A., Kampf, C. J., Kourtchev, I., Maenhaut, W., Marsden, N., Saarikoski, S., … Wisthaler, A. (1900). The Molecular Identification of Organic Compounds in the Atmosphere: State of the Art and Challenges. *Chemical Reviews*, 115(10), 3919–3983. https://doi.org/10.1021/cr5003485

Praplan, A. P., Schobesberger, S., Bianchi, F., Rissanen, M. P., Ehn, M., Jokinen, T., Junninen, H., Adamov, A., Amorim, A., Dommen, J., Duplissy, J., Hakala, J., Hansel, A., Heinritzi, M., Kangasluoma, J., Kirkby, J., Krapf, M., Kuerten, A., Lehtipalo, K., … Worsnop, D. R. (2015). Elemental composition and clustering behaviour of alpha-pinene oxidation products for different oxidation conditions. *Atmospheric Chemistry and Physics*, 15(8), 4145–4159. https://doi.org/10.5194/acp-15-4145-2015

Raguso, R. A., Henzel, C., Buchmann, S. L., & Nabhan, G. P. (2003). Trumpet Flowers of the Sonoran Desert: Floral Biology of Peniocereus Cacti and Sacred Datura. *International Journal of Plant Sciences*, *164*(6), 877–892. https://doi.org/10.1086/378539

Rhodes, M. K., Fant, J. B., & Skogen, K. A. (2017). Pollinator identity and spatial isolation influence multiple paternity in an annual plant. *Molecular Ecology*, *26*(16), 4296–4308. https://doi.org/10.1111/mec.14115

Riffell, J. A., Abrell, L., & Hildebrand, J. G. (2008a). Physical Processes and Real-Time Chemical Measurement of the Insect Olfactory Environment. Journal of Chemical Ecology, 34(7), 837–853. https://doi.org/10.1007/s10886-008-9490-7

Riffell, J. A., Alarcon, R., Abrell, L., Davidowitz, G., Bronstein, J. L., & Hildebrand, J. G. (2008b). Behavioral Consequences of Innate Preferences and Olfactory Learning in Hawkmoth: Flower Interactions. *Proceedings of the National Academy of Sciences - PNAS*, *105*(9), 3404–3409. https://doi.org/10.1073/pnas.0709811105

Riffell, J. A., Lei, H., Abrell, L., & Hildebrand, J. G. (2013). Neural Basis of a Pollinator's Buffet: Olfactory Specialization and Learning in Manduca sexta. Science (American Association for the Advancement of Science), 339(6116), 200–204. https://doi.org/10.1126/science.1225483

Riffell, J. A., Shlizerman, E., Sanders, E., Abrell, L., Medina, B., Hinterwirth, A. J., & Kutz, J. N. (2014). Flower discrimination by pollinators in a dynamic chemical environment. Science (American Association for the Advancement of Science), 344(6191), 1515–1518. https://doi.org/10.1126/science.1251041

Ryalls, J. M. W., Langford, B., Mullinger, N. J., Bromfield, L. M., Nemitz, E., Pfrang, C., & Girling, R. D. (2022). Anthropogenic air pollutants reduce insect-mediated pollination services. *Environmental Pollution (1987)*, *297*, 118847–118847. https://doi.org/10.1016/j.envpol.2022.118847

Satterfield, T. A., Sillett, T. S., Chapman, J. W., Altizer, S., & Marra, P. P. (2020). Seasonal insect migrations: massive, influential, and overlooked. *Frontiers in Ecology and the Environment*, *18*(6), 335–344. https://doi.org/10.1002/fee.2217

Saunier, A., & Blande, J. D. (2019). The effect of elevated ozone on floral chemistry of Brassicaceae species. *Environmental Pollution* (1987), 255(Pt 2), 113257. https://doi.org/10.1016/j.envpol.2019.113257

Schiestl. F. P. (2015). Ecology and evolution of floral volatile-mediated information transfer in plants. *The New Phytologist*, *206*(2), 571–577. https://doi.org/10.1111/nph.13243

Seinfeld, J. H., & Pandis, S. N. (2006). Atmospheric chemistry and physics : from air pollution to climate change (Second edition.). *John Wiley & Sons, Inc*.

Siemers, B. M., & Schaub, A. (2011). Hunting at the highway: traffic noise reduces foraging efficiency in acoustic predators. *Proceedings of the Royal Society. B, Biological Sciences*, *278*(1712), 1646–1652. https://doi.org/10.1098/rspb.2010.2262

Sipilä, M., Petäjä, T., & Thornton, J. A. (2017). Ambient observations of dimers from terpene oxidation in the gas phase: Implications for new particle formation and growth: Ambient Observations of Gas-Phase Dimers. *Geophysical Research Letters*, 44(6), 2958–2966. https://doi.org/10.1002/2017GL072718

Smith, J. N., Moore, K. F., McMurry, P. H., & Eisele, F. L. (2004). Atmospheric Measurements of Sub-20 nm Diameter Particle Chemical Composition by Thermal Desorption Chemical Ionization Mass Spectrometry. *Aerosol Science and Technology*, 38(2), 100–110. https://doi.org/10.1080/02786820490249036

Tam, M., & Hill, H. H. (2004). Secondary Electrospray Ionization-Ion Mobility Spectrometry for Explosive Vapor Detection. *Analytical Chemistry (Washington)*, 76(10), 2741–2747. https://doi.org/10.1021/ac0354591

Travis, K. R., Jacob, D. J., Fisher, J. A., Kim, P. S., Marais, E. A., Zhu, L., Yu, K., Miller, C. C., Yantosca, R. M., Sulprizio, M. P., Thompson, A. M., Wennberg, P. O., Crounse, J. D., Clair, J. M. S., Cohen, R. C., Laughner, J. L., Dibb, J. E., Hall, S. R., Ullmann, K., … Zhou, and X. (2016). Why Do Models Overestimate Surface Ozone in the Southeast United States? *Atmospheric Chemistry and Physics*, *16*(21), 13561–13577. https://doi.org/10.5194/acp-16-13561-2016

Troestl, J., Chuang, W. K., Gordon, H., Heinritzi, M., Yan, C., Molteni, U., Ahlm, L., Frege, C., Bianchi, F., Wagner, R., Simon, M., Lehtipalo, K., Williamson, C., Craven, J. S., Duplissy, J., Adamov, A., Almeida, J., Bernhammer, A.-K., Breitenlechner, M., … Flagan, R. C. (2016). The role of low-volatility organic compounds in initial particle growth in the atmosphere. *Nature (London)*, 533(7604), 527–531. https://doi.org/10.1038/nature18271

Tu, P. J., Hall, W. A., & Johnston, M. V. (2016). Characterization of Highly Oxidized Molecules in Fresh and Aged Biogenic Secondary Organic Aerosol. *Analytical Chemistry (Washington)*, 88(8), 4495–4501. https://doi.org/10.1021/acs.analchem.6b00378

United Nations, Department of Economic and Social Affairs, Population Division (2019). World Urbanization Prospects 2018: Highlights (ST/ESA/SER.A/421). https://population.un.org/wup/Publications/Files/WUP2018-Highlights.pdf

Vanderplanck, M., Lapeyre, B., Brondani, M., Opsommer, M., Dufay, M., Hossaert-McKey, M., & Proffit, M. (2021). Ozone Pollution Alters Olfaction and Behavior of Pollinators. *Antioxidants*, *10*(5), 636. https://doi.org/10.3390/antiox10050636

Veres, P., Roberts, J. M., Warneke, C., Welsh-Bon, D., Zahniser, M., Herndon, S., Fall, R., & de Gouw, J. (2008). Development of negative-ion proton-transfer chemical-ionization mass spectrometry (NI-PT-CIMS) for the measurement of gas-phase organic acids in the atmosphere. *International Journal of Mass Spectrometry*, 274(1), 48–55. https://doi.org/10.1016/j.ijms.2008.04.032

Walton, R. E., Sayer, C. D., Bennion, H., & Axmacher, J. C. (2020). Nocturnal pollinators strongly contribute to pollen transport of wild flowers in an agricultural landscape. *Biology Letters (2005)*, *16*(5), 20190877–20190877. https://doi.org/10.1098/rsbl.2019.0877

Wang, X., Jacob, D. J., Downs, W., Zhai, S., Zhu, L., Shah, V., et al. (2021). Global tropospheric halogen (Cl, Br, I) chemistry and its impact on oxidants. *Atmospheric Chemistry and Physics*, *21*(18), 13973–13996. https://doi.org/10.5194/acp-21-13973-2021

Wesely, M. M. (1989). Parameterization of surface resistances to gaseous dry deposition in regional-scale numerical models. *Atmospheric Environment, 23*, 1293–1304. https://doi.org/10.1016/j.atmosenv.2007.10.058

Whitehouse, C.M., Levin, F., Meng, C.K., Fenn, J.B.: Proceedings of the 34th ASMS Conference on Mass Spectrometry and Allied Topics, Denver, 507, 1986.

Witkowski, B., & Gierczak, T. (2013). Analysis of α-acyloxyhydroperoxy aldehydes with electrospray ionization-tandem mass spectrometry (ESI-MSn). *Journal of Mass Spectrometry*., 48(1), 79–88. https://doi.org/10.1002/jms.3130

Wu, C., Siems, W. F., & Hill, H. H. (2000). Secondary Electrospray Ionization Ion Mobility Spectrometry/Mass Spectrometry of Illicit Drugs. *Analytical Chemistry (Washington)*, 72(2), 396–403. https://doi.org/10.1021/ac9907235

Xu, R., Thornton, J. A., Lee, B. H., Zhang, Y., Jaeglé, L., Lopez-Hilfiker, F. D., Rantala, P., & Petäjä, T. (2022). Global simulations of monoterpene-derived peroxy radical fates and the distributions of highly oxygenated organic molecules (HOMs) and accretion products. *Atmospheric Chemistry and Physics*, *22*(8), 5477–5494. https://doi.org/10.5194/acp-22-5477-2022

Yatavelli, R. L. N., Lopez-Hilfiker, F., Wargo, J. D., Kimmel, J. R., Cubison, M. J., Bertram, T. H., Jimenez, J. L., Gonin, M., Worsnop, D. R., & Thornton, J. A. (2012). A Chemical Ionization High-Resolution Time-of-Flight Mass Spectrometer Coupled to a Micro Orifice Volatilization Impactor (MOVI-HRToF-CIMS) for Analysis of Gas and Particle-Phase Organic Species. *Aerosol Science and Technology*, 46(12), 1313–1327. https://doi.org/10.1080/02786826.2012.712236

Yuan, B., Koss, A., Warneke, C., Gilman, J. B., Lerner, B. M., Stark, H., & de Gouw, J. A. (2016). A high-resolution time-of-flight chemical ionization mass spectrometer utilizing hydronium ions (H3O+ ToF-CIMS) for measurements of volatile organic compounds in the atmosphere. *Atmospheric Measurement Techniques*, 9(6), 2735–2752. https://doi.org/10.5194/amt-9-2735-2016

Zar. (2010). *Biostatistical analysis* (Fifth edition.). Prentice Hall.

Zhai, S., Wang, X., McConnell, J. R., Geng, L., Cole-Dai, J., Sigl, M., et al. (2021). Anthropogenic Impacts on Tropospheric Reactive Chlorine Since the Preindustrial. *Geophysical Research Letters, 48*(14). https://doi.org/10.1029/2021GL093808

Zhang, X., Lambe, A. T., Upshur, M. A., Brooks, W. A., Gray Bé, A., Thomson, R. J., Geiger, F. M., Surratt, J. D., Zhang, Z., Gold, A., Graf, S., Cubison, M. J., Groessl, M., Jayne, J. T., Worsnop, D. R., & Canagaratna, M. R. (2017). Highly Oxygenated Multifunctional Compounds in α-Pinene Secondary Organic Aerosol. *Environmental Science & Technology*, 51(11), 5932–5940. https://doi.org/10.1021/acs.est.6b06588

Zhao, J., Eisele, F. L., Titcombe, M., Kuang, C., & McMurry, P. H. (2010). Chemical ionization mass spectrometric measurements of atmospheric neutral clusters using the cluster-CIMS. *Journal of Geophysical Research*, 115(D8). https://doi.org/10.1029/2009JD012606

Zhao, J., Ortega, J., Chen, M., McMurry, P. H., & Smith, J. N. (2013). Dependence of particle nucleation and growth on high-molecular-weight gas-phase products during ozonolysis of alpha-pinene. *Atmospheric Chemistry and Physics*, 13(15), 7631–7644. https://doi.org/10.5194/acp-13-7631-2013

Zhao, Y., Wingen, L. M., Perraud, V., Greaves, J., & Finlayson-Pitts, B. J. (2015). Role of the reaction of stabilized Criegee intermediates with peroxy radicals in particle formation and growth in air. *Physical Chemistry Chemical Physics : PCCP*, 17(19), 12500–12514. https://doi.org/10.1039/c5cp01171j

Zhao, Y., Wingen, L. M., Perraud, V., & Finlayson-Pitts, B. J. (2016). Phase, composition, and growth mechanism for secondary organic aerosol from the ozonolysis of alpha-cedrene. Atmospheric Chemistry and Physics, 16(5), 3245–3264. https://doi.org/10.5194/acp-16-3245-2016

Zhao, Y., Chan, J. K., Lopez-Hilfiker, F. D., McKeown, M. A., D'Ambro, E. L., Slowik, J. G., Riffell, J. A., & Thornton, J. A. (2017). An electrospray chemical ionization source for real-time measurement of atmospheric organic and inorganic vapors. Atmospheric Measurement Techniques, 10(10), 3609–3625. https://doi.org/10.5194/amt-10-3609-2017

Zhu, J. J., Bean, H. D., Kuo, Y.-M., & Hill, J. E. (2011). Fast Detection of Volatile Organic Compounds from Bacterial Cultures by Secondary Electrospray Ionization-Mass Spectrometry (vol 48, pg 4426, 2010). *Journal of Clinical Microbiology*, 49(2), 769–769. https://doi.org/10.1128/JCM.02580-10